

**Diffusion and surface trapping of ^8Li in
rutile TiO_2 and the comparison on ^8Li and
 ^9Li spin relaxation using β -NMR**

by

Christos Aris Chatzichristos

Diploma, National Technical University of Athens, 2013

A THESIS SUBMITTED IN PARTIAL FULFILLMENT OF
THE REQUIREMENTS FOR THE DEGREE OF

DOCTOR OF PHILOSOPHY

in

The Faculty of Graduate and Postdoctoral Studies

(Physics)

THE UNIVERSITY OF BRITISH COLUMBIA

(Vancouver)

February 2020

© Christos Aris Chatzichristos 2020

The following individuals certify that they have read, and recommend to the Faculty of Graduate and Postdoctoral Studies for acceptance, the dissertation entitled:

Diffusion and surface trapping of ^8Li in rutile TiO_2 and the comparison on ^8Li and ^9Li spin relaxation using β -NMR

submitted by Christos Aris Chatzichristos in partial fulfillment of the requirements for the degree of Doctor Of Philosophy in Physics

Examining Committee:

Robert F. Kiefl, Physics and Astronomy
Co-supervisor

W. Andrew MacFarlane, Chemistry
Co-supervisor

Brian Wetton, Mathematics
University Examiner

John D. Madden, Electrical and Computer Engineering
University Examiner

Additional Supervisory Committee Members:

Douglas Bonn, Physics and Astronomy
Supervisory Committee Member

Joerg Rottler, Physics and Astronomy
Supervisory Committee Member

Mark Halpern, Physics and Astronomy
Supervisory Committee Member

Abstract

It is well established that the properties of many materials change as their thickness is shrunk to the nanoscale, often yielding novel features at the near-surface region that are absent in the bulk. Even though there are several techniques that can study either the bulk or the surface of these materials, there are very few that can scan the near-surface region of crystals and thin films versus depth. Beta-detected NMR (β -NMR) is capable of this and therefore has been established as a powerful tool for material science. This thesis aims to further develop the capabilities of β -NMR.

The first part of this thesis demonstrates that by comparing the spin-lattice relaxation rates (SLR) of two radioactive Li isotopes ($^8,^9\text{Li}$) it is possible to distinguish whether the source of SLR in a given situation is driven by magnetic or electric interactions. This is an important development for β -NMR, since there are instances where it is problematic to distinguish whether the measured relaxation is due to magnetic or electric fluctuations. Using this method, it was found that the SLR in Pt is (almost) purely magnetic in origin, whereas the spin relaxation in SrTiO_3 is driven (almost) entirely by electric quadrupolar interactions.

The second part of this thesis traces the development of α -radiotracer, that uses the progeny α -particles from the decay of ^8Li , in order to directly measure the nanoscale diffusivity of Li^+ in Li-ion battery materials. To develop this technique, Monte Carlo simulations of the experimental configuration were carried out, a new apparatus and a new α -detector were designed and used for experiments on rutile TiO_2 . In rutile, the measurements revealed that Li^+ gets trapped at the (001) surface, a result that helps explain the suppressed intercalation of Li^+ in bulk rutile. Moreover, the diffusion rate of Li^+ in rutile was found to follow a bi-Arrhenius relationship, with a high- T activation energy in agreement with other reported measurements and a low- T component of similar magnitude with the theoretically calculated diffusion barrier as well as the activation energy of the Li-polaron complex found with β -NMR below 100 K.

Lay Summary

Beta-detected NMR (β -NMR) is capable of studying both the magnetic and electric properties of materials at the nanoscale (billionth of a meter) and therefore has been established as a powerful tool for material science. The first part of this thesis demonstrates that by comparing the β -NMR signal of two radioactive lithium isotopes it is possible to distinguish whether the dominant interaction in a given situation is magnetic or electric in origin. This development can aid the identification and fabrication of materials with useful properties for a wide range of applications.

In addition, in this thesis the α -radiotracer technique for studying nanoscale lithium diffusion was developed. Studying diffusion is crucial for identifying better materials for next-generation lithium-ion batteries. This technique uses nuclear physics to study how fast lithium ions move inside materials and also what happens when these ions reach a surface.

Preface

I was the lead investigator for the projects located in Chapters 3.3, 5 and 6, where I was responsible for all major areas of concept formation, data analysis, as well as the majority of manuscript composition. For the project located in Sections 3.1- 3.2.3, I was responsible for the data analysis and manuscript composition and I took part in the data collection, while Rob Kiefl and Andrew MacFarlane were responsible for the concept creation.

Most of the results presented in Chapters 3 and 6, as well as some work presented in Chapter 5 have been published in peer-reviewed articles, either in journals or conference proceedings. In these articles I am listed as the first author and the co-authors took part in the data collection and manuscript revision processes. More details on the division of work between myself and the co-authors are given below for each publication. The relevant papers are the following:

- A. Chatzichristos, R. M. L. McFadden, V. L. Karner, D. L. Cortie, C. D. P. Levy, W.A. MacFarlane, G. D. Morris, M. R. Pearson, Z. Salman, and R. F. Kiefl, “Determination of the nature of fluctuations using ^8Li and ^9Li β -NMR and spin-lattice relaxation”, *Phys. Rev. B* **96**, 014307 (2017) [1]; which contains a version of Sections 3.1 to 3.2.3. I carried out the data analysis in collaboration with R. M. L. McFadden and prepared the manuscript. I presented the findings of this paper in an oral presentation (invited talk) at the “Applications of Nuclear Physics” Mini-Symposium of the American Physical Society, Division of Nuclear Physics meeting, Vancouver, BC, Canada (October 2016).
- A. Chatzichristos, R. M. L. McFadden, V. L. Karner, D. L. Cortie, C. D. P. Levy, W. A. MacFarlane, G. D. Morris, M. R. Pearson, Z. Salman, and R. F. Kiefl, “Comparison of ^8Li and ^9Li spin relaxation in SrTiO_3 and Pt: A means to distinguish magnetic and electric quadrupolar sources of relaxation” in Proceedings of the 14th International Conference on Muon Spin Rotation, Relaxation and Resonance ($\mu\text{SR}2017$) [2]; which contains a version of Sections 3.3 and 3.4. I carried out the data analysis and prepared the manuscript. I presented the findings of this paper on a poster at the 14th International

Conference on Muon Spin Rotation, Relaxation and Resonance (μ -SR 2017), Hokkaido University, Sapporo, Hokkaido, Japan (July 2017).

- A. Chatzichristos, R.M.L. McFadden, M.H. Dehn, S.R. Dunsiger, D. Fujimoto, V.L. Karner, C.D.P. Levy, I. McKenzie, G.D. Morris, M.R. Pearson, M. Stachura, J. Sugiyama, J.O. Ticknor, W.A. MacFarlane, and R.F. Kiefl, “Bi-Arrhenius Diffusion and Surface Trapping of $^8\text{Li}^+$ in Rutile TiO_2 ”, *Phys. Rev. Lett.* *123*, 095901 (2019) [3]; which contains a version of Sections 6.1 to 6.4. I carried out the simulation study, developed the data analysis tools, conducted the data analysis and prepared the manuscript. I presented the findings of this letter in an oral presentation at the 28th annual symposium of the Hellenic Nuclear Physics Society, Thessaloniki, Greece (June 2019).

The publishers of the aforementioned papers have granted permission for this material to be incorporated into this thesis.

Table of Contents

Abstract	iii
Lay Summary	iv
Preface	v
Table of Contents	vii
List of Tables	x
List of Figures	xi
Acknowledgments	xiv
Dedication	xv
1 Introduction	1
1.1 Importance of nanomaterials	1
1.1.1 Experimental techniques to study nanoscale phenomena	2
1.2 Li-ion Diffusion - Solid State Li-ion Batteries	6
1.2.1 Importance of Li-ion Batteries	6
1.2.2 Experimental Methods for Studying Solid State Diffusion	9
1.2.3 Studying nanoscale Li diffusion	11
1.3 Organization of this Thesis	12
2 Beta-detected Nuclear Magnetic Resonance	14
2.1 Physics of β -NMR	14
2.2 Experimental Details of β -NMR at TRIUMF	16
2.2.1 Polarized Beam Production and Delivery	17
2.2.2 β -NMR and β -NQR Spectrometers	22
2.2.3 Beam Implantation Profiles	26
2.3 Spin Interactions of β -NMR probes in a lattice	28
2.3.1 Magnetic Interactions	29

2.3.2	Electric Quadrupolar Interactions	30
2.4	Types of Measurements	32
2.4.1	Resonance Spectra	32
2.4.2	Spin Lattice Relaxation Spectra	36
2.5	Enhancing the capabilities of β -NMR using α detection	38
3	Using α-tagged ^9Li β-NMR to Distinguish the Source of Spin Lattice Relaxation in ^8Li β-NMR	41
3.1	Isotopic Comparison Method	42
3.2	Experimental Demonstration of the Isotopic Comparison Method	43
3.2.1	Platinum	44
3.2.2	Strontium Titanate	46
3.2.3	Ratio of Relaxation Rates	50
3.3	Enhancing the Effective Asymmetry of ^9Li Using α -tagging	52
3.3.1	α LithEIA Method	53
3.3.2	Experimental Testing of the α LithEIA Method on ZnS(Ag)	56
3.4	Conclusions	61
4	Principles of Interstitial Diffusion in Solids	62
4.1	Macroscopic Theory of Solid State Diffusion	62
4.1.1	Fick's Laws	63
4.1.2	Temperature Dependence of Diffusion: Arrhenius Law	64
4.2	Microscopic Theory of Diffusion	65
4.2.1	One Dimensional Random Walk	66
4.2.2	Boundary Conditions	68
4.2.3	Einstein-Smoluchowski Law	70
4.2.4	Isotopic mass effect on diffusion	74
5	Principles of Studying Nanoscale Lithium Diffusion Using the α-Decay of ^8Li	76
5.1	Basic Principles of the ^8Li α -radiotracer Technique	76
5.2	Simulations of α -Detected Lithium Diffusion	81
5.2.1	Temporal Evolution of the Diffusion Profiles	82
5.2.2	Geant4 Simulations	85
5.3	Calculating the α -radiotracer signal	96
5.4	Conclusions	99
6	Measurements of ^8Li Diffusion in Rutile using α Detection	101
6.1	Rutile - General Characteristics	101
6.2	Experimental Details	103

6.3	Experimental Results on Rutile TiO ₂ Using the α -radiotracer Technique	103
6.4	Arrhenius Fits and Discussion	108
6.5	Conclusions	113
7	Conclusions and Future Work	114
7.1	Summary	114
7.1.1	Isotopic comparison for distinguishing magnetic and electric relaxation in β -NMR	115
7.1.2	Establishing the α -radiotracer technique for studying nanoscale Li diffusion	116
7.1.3	Study of the Li ⁺ motion in rutile TiO ₂ , using the α -radiotracer technique	116
7.2	Future Work	117
	Bibliography	119

Appendices

A	The cryo-oven	140
B	Geant4	145
B.1	Getting started	145
B.2	The project code tree	145
B.3	Running the simulation	147
B.4	Structure of the Geant4 project	148
B.4.1	LiDiffusion.cc	148
B.4.2	LiDetectorConstruction/LiDetectorMessenger	148
B.4.3	PhysicsList	149
B.4.4	LiActionInitialization	149
B.4.5	LiPrimaryGeneratorAction/LiPrimaryGeneratorMessenger 150	
B.4.6	LiRunAction/LiEventAction/LiSteppingAction	151
B.4.7	Output files	151
B.4.8	Macro (input) file	152

List of Tables

1.1	Comparison of classical NMR with β -NMR	4
2.1	Intrinsic nuclear properties of radioisotopes used in β -NMR . . .	16
3.1	The asymmetry of each decay mode of ${}^9\text{Li}$	54
3.2	Fits of the untagged, α -tagged and no- α -tagged spectra of ${}^9\text{Li}$ β -NMR at 308 K in ZnS(Ag)	60

List of Figures

1.1	Li-ion battery market expansion (2000-2015)	7
1.2	Schematic of a (C/LiCoO ₂) Li-ion battery	8
1.3	Direct and indirect methods for studying solid state diffusion . . .	9
1.4	The steps for measuring diffusion with the (radio)tracer method .	11
2.1	Anisotropy of the direction of the emitted β -particles	15
2.2	Energy distribution of the β - and α -particles coming from the decay of ⁸ Li	17
2.3	Internal view of the 520 MeV main cyclotron vault at TRIUMF . .	18
2.4	Schematic of the polarizer and the section of the beamline leading to the β -NMR and β -NQR spectrometers	19
2.5	Schematic of the spin polarization method for ⁸ Li	20
2.6	Schematic of the high-field β -NMR spectrometer	23
2.7	Image of the β -NMR sample holder	24
2.8	Over-view of the β -NQR spectrometer	25
2.9	Image of the β -NQR sample holder	26
2.10	Tracks of ⁸ Li implanted in TiO ₂ , as simulated by SRIM-2013 . . .	27
2.11	⁸ Li beam implantation profile in TiO ₂ as simulated by SRIM-2013	28
2.12	The energy splitting of the magnetic sub-levels of ⁸ Li, due to the axial part of the Hamiltonian	32
2.13	Resonance spectrum for ⁸ Li in a Bismuth single crystal at 294 K .	33
2.14	Resonance spectrum for ⁸ Li implanted in a epitaxial Ag film grown on MgO at 155 K	35
2.15	SLR spectrum of ⁸ Li implanted in a single crystal of bismuth at at 295 K	38
3.1	Resonance spectra in Pt foil at 300 K and 1.90 T with ⁸ Li and ⁹ Li	45
3.2	SLR spectra for ⁸ Li ⁺ and ⁹ Li ⁺ in Pt foil at 300 K and 6.55 T	46
3.3	Measured SLR rates for ⁸ Li implanted in Pt	47
3.4	Crystal structure of SrTiO ₃	48
3.5	SLR spectra of ⁸ Li and ⁹ Li in single crystal SrTiO ₃ at 300 K . . .	49

3.6	Field dependence of $1/T_1$ for ^8Li and ^9Li in SrTiO_3 (sample S1) at 300 K	50
3.7	SLR spectra of ^8Li and ^9Li in SrTiO_3 at 10 mT and 300 K	51
3.8	Ratios of ^9Li to ^8Li $1/T_1$ relaxation rates in Pt and in the two SrTiO_3 samples	52
3.9	Properties of the principle β -decay modes of ^8Li and ^9Li	53
3.10	Theoretical initial β -asymmetry detected in coincidence/absence of an α , for varying α -detection efficiency	55
3.11	Resonance spectrum for ^8Li in $\text{ZnS}(\text{Ag})$ at 10 K	57
3.12	Crystal structure of $\text{ZnS}(\text{Ag})$	58
3.13	Temperature dependence of the fraction of the relaxing component and the relaxation rate in $\text{ZnS}(\text{Ag})$	59
3.14	Untagged, α -tagged and no- α -tagged spectra of ^9Li β -NMR at 310 K in $\text{ZnS}(\text{Ag})$	59
3.15	The normalized decay curves of the light emitted from a $\text{ZnS}(\text{Ag})/{}^6\text{LiF}$ scintillator illuminated with 5.5 MeV α -particles	60
4.1	Density profiles with an accumulative wall	69
4.2	Density profiles with a reflective wall	71
4.3	Image of n individual random steps on a lattice	72
4.4	Interstitial atom's jumping process	73
5.1	Schematic of the ultra-high vacuum sample region with the cross-section of the ring detector	77
5.2	Schematic of the α -detection geometry	78
5.3	Simulated counts at the α -detector versus time	80
5.4	Calculated depth profiles of Li ions versus time	84
5.5	Simulated fraction of Li ions trapped at the front surface of a TiO_2 sample versus time	85
5.6	Geometry simulated by Geant4	88
5.7	Simulation of the distribution of the energy deposited at the α -detector at different times	90
5.8	The normalized α -spectrum, as simulated with Geant4 in TiO_2 , for different α -detector energy thresholds	91
5.9	The normalized α -signal, as simulated with Geant4 in TiO_2 , for different diffusion rates	92
5.10	The normalized α -signal, as simulated with Geant4 in TiO_2 , for a reflective surface	93
5.11	The normalized α -signal, for various trapping probabilities at the surface of the sample	94

5.12	Simulated α -signals for beam energies of 10 keV and 25 keV . . .	95
5.13	The energy deposition profile of α - and β -particles inside the α - detector for various detector thicknesses	96
5.14	Probability of α -detection versus decay depth	98
5.15	Comparison of calculated and simulated normalized $Y_{\alpha}^n(t)$ signals	99
6.1	A 3-D view of the rutile TiO_2 unit cell	102
6.2	Comparison of the measured normalized α -yield for the (110)- and (001)-oriented rutile	105
6.3	Comparison of the measured normalized α -yield between unrotated and rotated (001)-oriented rutile	106
6.4	Fits of the measured normalized α -yield for the (001)-oriented rutile at various temperatures	107
6.5	Arrhenius plot, comparing reported Li diffusivity in rutile TiO_2 . .	109
6.6	Arrhenius fit to the diffusion rates of ^8Li found in this study	110
A.1	Figure showing the sample holder used in the cryo-oven assembly	140
A.2	Images of two SolidWorks cuts of the lower region of the cryo-oven assembly	143
A.3	Images of two SolidWorks overviews of the cryo-oven assembly .	144

Acknowledgments

True to the spirit of sir Isaac Newton's famous quote about standing on the shoulders of giants, this work would be completely impossible without the help and guidance of my supervisors, Prof. Rob Kiefl and Prof. Andrew MacFarlane. Their expertise and knowledge in both experimental and theoretical issues, but also their enthusiasm and vision were crucial for the completion of most aspects of this work. I want also to thank the other members of my PhD committee: Douglas Bonn, Mark Halpern and Joerg Rottler for taking the time to read the thesis and for their insightful comments.

A major part of this thesis revolves around the incarnation of the α -radiotracer technique, which, among other things, required the design, fabrication and assembly of a novel, completely custom-made cryostat: the chimeric cryo-oven. This project was benefited greatly by the expertise and knowledge of Gerald Morris, who aided us in all phases of the cryo-oven's development. I want to thank Mike McLay for his great work in translating the doodles of the various parts of the cryo-oven Rob and I made to meaningful 3D blueprints. Last but not least, I want to acknowledge Rahim Abasalti and Deepak Vyas for their really herculean labor and their immense contribution to the assembly, mounting and preparation of the cryo-oven.

I want also to say a great thank you to all my colleagues in the β -NMR group: Victoria Karner, Ryan McFadden, Martin Dehn, Derek Fujimoto, John Ticknor, Iain McKenzie, Monika Stachura, Sarah Dunsiger and others. This whole endeavor was a highly collaborative process with everybody taking shifts for data acquisition and helping with most aspects of analysis, interpretation, etc. Special thanks to Victoria and Ryan, who gave me the introductory crash course on the ins and outs of β -NMR. I would also like to express my gratitude to TRIUMF staff members Matt Pearson, Phil Levy, Bassam Hitti, Donald Arseneau and Suzannah Davie for their aid and all their meaningful contributions during the β -NMR and α -radiotracer experiments.

Dedication

To all the people that guided and helped me, my spouse and my parents most of all.

Κτῆμα τε ἐς αἰεὶ μᾶλλον ἢ ἀγώνισμα ἐς τὸ παραχρῆμα

Chapter 1

Introduction

1.1 Importance of nanomaterials

New experimental tools and techniques capable of studying nanoscale phenomena, are constantly revealing new and potentially useful properties. The difference between nanomaterials (e.g., particles or thin-films) and their bulk forms stems from finite size effects and interfaces which can give rise to new and unusual properties. When one (or several) of a material's dimensions approaches the nanoscale, certain underlying quantum effects cannot be neglected any more, as the classical limit gets progressively less valid. This gives rise to novel material properties (optical, electromagnetic, chemical, etc), that are much less important on a macroscopic length scale. For instance, the 2D electron gas (2DEG) [4], realized at the interface of certain heterostructures, exhibits extremely high electron (hole) mobility and can also give rise to the quantum Hall effect, where the conductance can only take quantized values [5]. In addition, the material properties are in many cases size-dependent in this scale. This permits the fine-tuning of certain properties (e.g., electrical conductivity and magnetic permeability) by changing the size of the particle or the thin-film. An important example of this tunability relates to quantum dots, which are small semiconductor particles having a nanoscale diameter. When certain quantum dots are illuminated they will emit light, the frequency of which depends on the particle's size [6].

Apart from the rise of quantum mechanics at this scale, a second reason behind the importance of the nanoscale is the large surface-to-mass ratios of nanomaterials. Indeed, a spherical nanoparticle with a radius of 100 nm would have a surface-to-mass ratio 10,000 times larger than a 1 mm radius single-crystal of the same substance. A greater surface area increases the chemical reactivity of the substance, which can greatly improve, for instance, the properties of catalysts used in chemistry and chemical engineering.

Moreover, the developments in nanoscale fabrication and experimental techniques revealed a plethora of interesting surface phenomena. A few examples include the novel material class of topological insulators [7], which have topologically-protected conduction states at their surface while being bulk insulators, as well as the fabrication of magnetic surfaces, interfaces and thin films [8].

The above-mentioned phenomena are not just of pure scientific interest, but they rather have very important applications. For instance, quantum tunneling is responsible for the development of flash memory for computers [9] and topological insulators might be used in the future for better magnetic (memory) devices [10].

1.1.1 Experimental techniques to study nanoscale phenomena

Many interesting and important nanoscale phenomena have been discovered by the parallel development of a large number of experimental methods capable of studying them. For instance, nuclear magnetic resonance (NMR) [11] is sensitive to local electromagnetic fields and resonant X-ray diffraction (XRD) [12] can effectively provide site-specific chemical information, but both lack the sensitivity to explore surface or near-surface phenomena, however useful they may be in studying the bulk of materials.

Another very important class of experimental techniques includes many that can probe the surface properties of thin films and single crystal samples. Grazing incidence X-ray diffraction and neutron reflectivity, are two complementary techniques [13] that illuminate the sample with different probes and use their diffraction to extract properties of the surface and near-surface region. Atomic force microscopy (AFM) [14] uses piezoelectric elements to image the surface of solids with sub-nanometer resolution, as well as to perform force spectroscopy. Scanning tunneling microscopy (STM) [15] is capable of imaging surfaces with single-atom resolution. It makes use of the quantum tunneling effect, by bringing a conducting tip close to the sample surface and then observing the tunneling current versus applied voltage and tip position. Angle-resolved photoemission spectroscopy (ARPES) [16] can be used to explore the electronic structure of solids (i.e., their k-space/momentum-resolved band structure), using the electron photoemission upon illumination with soft X-rays.

Despite the large number of available techniques for studying nanoscale materials, very few are able to study the near-surface region (1 nm to 100 nm) of a sample. This is a very interesting region, where one can study how the material properties change versus the distance from the surface [17–19] (or an interface between two heterostructures [20]). Among the techniques mentioned above, only grazing incidence X-ray diffraction and neutron reflectivity are able to probe this near-surface region and both of them are reciprocal-space probes as opposed to real-space probes. Indeed, there are only two general purpose real-space techniques capable of studying the near-surface region of thin-films and single crystals, β -detected NMR (β -NMR) and low energy muon spin rotation/relaxation (LE- μ SR), accompanied by some special-case techniques, such as conversion-electron Mössbauer spectroscopy [21].

In recent years, β -NMR has been established as a powerful tool of material

science due to its inherent sensitivity to magnetic and electronic properties of the probe's local environment [22]. It has been used extensively to study, amongst other topics, metals [23, 24], insulators – both classical [25] and topological [26] –, superconductors [27], semiconductors [28], lithium diffusion [29, 30], soft condensed matter [31], antiferromagnetism [17], as well as recently ionic liquids [32].

Despite its wide range of applications and its demonstrated success in studying the nanoscale, β -NMR is still not very well known or widely used. The primary reason is that it requires an extensive infrastructure, including a particle accelerator capable of delivering an intense beam of spin-polarized radionuclides. There are very few centers in the world with such capabilities and all of them focus primarily on nuclear or particle physics research. These include TRIUMF in Canada [33], ISOLDE in Switzerland [34, 35], Osaka [36] and Moscow [37]. From these, the center with the most developed β -NMR program is the ISAC facility at TRIUMF, Canada's national laboratory for nuclear and particle physics.

A major limitation on the proliferation of the β -NMR technique is that ISAC is a single-user facility, meaning that only one experiment may be using the radioactive beam at any given time. Typically, the beamtime dedicated to β -NMR experiments at TRIUMF is limited to 5 weeks/year, but at the time of writing it is significantly lower, due to extended shutdown periods each year for helping with the ARIEL upgrade [38]. As a consequence, the β -NMR beamtime at TRIUMF has to be used *very* effectively, which sometimes makes it difficult to obtain beamtime for control measurements. This underlines the need for more β -NMR user facilities.

The principle success of TRIUMF's low-energy incarnation of β -NMR [33, 39] is the ability to study thin films, surfaces, and interfaces — situations where conventional NMR is ill-suited. This stems from β -NMR's high sensitivity (per nuclei) relative to conventional NMR; typically only $\sim 10^8$ nuclei (instead of $\sim 10^{17}$) are required for a discernible spectrum (see Tab.1.1).

Table 1.1: Comparison of classical NMR with β -NMR. *Nuclear Polarization* refers to the percentage of the spin-probes in the sample that are spin-polarized, whereas *Sensitivity* refers to the number of spin-probes needed for a spectrum. The much greater sensitivity of β -NMR, permits the study of thin-films.

	NMR	β -NMR
Nuclear Polarization	$\ll 1\%$	$\sim 70\text{-}80\%$
Nuclear Probes	stable nuclei with spin, e.g., ^1H , ^{13}C , ^{57}Fe , ^{17}O , etc	unstable nuclei with spin, e.g., $^8\text{Li}^+$, $^9\text{Li}^+$, $^{31}\text{Mg}^+$, etc
Sensitivity	$> 10^{16}$ probes	$\sim 10^8$ probes
Detection Method	Induced EMF in a coil from precession of nuclear magnetization	Anisotropic β -decay

In classical NMR, the nuclear spin polarization is achieved by applying a strong magnetic field on the sample. This field splits the degeneracy of the nuclear spin states, making the state with the nuclear spin parallel to the field energetically favorable by an energy difference –for spin 1/2 nuclei – of $\Delta E = 2\mu B$, where μ is the nuclear magnetic moment. At a temperature T , the ratio of the occupation of the two spin states of a spin-1/2 nucleus is given by a Boltzman distribution:

$$N_+/N_- = \exp(-\Delta E/k_B T) \quad (1.1)$$

where N_+ and N_- are the populations of the \pm nuclear spin states at the axis defined by the applied magnetic field and k_B is the thermodynamic Boltzmann constant. Almost always $\Delta E \ll k_B T$, which leads to the approximation:

$$N_+/N_- \sim 1 - \frac{\Delta E}{k_B T} \quad (1.2)$$

It is important to note that unlike conventional NMR, where the thermodynamic Boltzmann factor ($\Delta E/k_B T$) determines the polarization, the initial non-equilibrium nuclear polarization in β -NMR is close to unity and independent of the sample temperature and/or magnetic field. Consequently, measurements can be made under conditions where conventional NMR is difficult or impossible e.g., at high temperatures, low magnetic fields or in thin films. The intensity of the implanted beam (typically $\sim 10^7 \text{ s}^{-1}$), is such that the concentration of the nuclear probes is so small that there is no interaction between probes and thus no homo-nuclear spin-coupling.

The only other real-space technique with equivalent sensitivity over a comparable material length scale (viz. 10 nm to 200 nm) [40] is low-energy μSR [41–43].

μ SR is a sister technique to β -NMR, in the sense that both rely on the same underlying physical principle (i.e. parity violation in weak nuclear interactions, see Sect. 2.1). However, they operate in complementary time-windows due to the different probe lifetimes (1.21 s for ${}^8\text{Li}^+$ vs. 2.2 μs for μ^+). As a result, the two techniques are sensitive to spin relaxation rates of completely different frequencies. Broadly speaking, the time range of each technique is defined as $[\tau_\beta/100 - 100\tau_\beta]$, where τ_β is the lifetime of the radioactive probe, which means that μ SR is most suitable to study electromagnetic spin relaxation rates at the MHz scale, whereas ${}^8\text{Li}$ β -NMR can be used to probe spin relaxation rates at the sub-Hz to kHz range. Thus, both techniques have leveraged the nuclear physics of β -decay to investigate topical problems in condensed matter physics, including magnetic surfaces, thin film heterostructures and near surface phenomena.

This thesis aims to further enhance the capabilities of ${}^8\text{Li}$ β -NMR, by developing new tools and methods that use the α -emissions of ${}^9,8\text{Li}$ in conjunction with the β -NMR signal coming from the β -decay.

The first part of the thesis (Ch. 2-3) describes the isotopic comparison method, which compares the spin-lattice relaxation (SLR) rates of two radioactive isotopes (in this case ${}^9\text{Li}$ and ${}^8\text{Li}$) under identical experimental conditions to distinguish the source of SLR in a given situation, enhancing thusly β -NMR's capabilities of studying the nanoscale. Indeed, using this method we were able to show that the SLR rate in Pt is caused by primarily magnetic interactions, whereas in SrTiO_3 the main effect driving the SLR is electric quadrupolar in origin. One major limitation when using the ${}^9,8\text{Li}$ isotopic comparison method is that the effective β -decay asymmetry of ${}^9\text{Li}$ is very low. This is due to the fact that ${}^9\text{Li}$ has three different decay paths, two of which have opposite asymmetries that nearly cancel. This results in a very small β -NMR signal which makes the ${}^9\text{Li}$ β -NMR measurements very time-consuming. To partly overcome this issue, we developed a method for distinguishing the decay paths of ${}^9\text{Li}$ by using the α -particles coming from the decay of ${}^9\text{Li}$. This method is termed α -detection for Lithium-9 Enhanced Initial Asymmetry ($\alpha\text{LithEIA}$) and can in principle increase the effective asymmetry of ${}^9\text{Li}$ by a factor of ~ 3 .

The second part of this work (Ch. 4-6) describes the development (from first principles to full material studies) of the ${}^8\text{Li}$ α -radiotracer method, which is capable of studying nanoscale Li diffusion using the α -decay of ${}^8\text{Li}$. Indeed, we employed this method to study ${}^8\text{Li}$ diffusion in rutile TiO_2 (see Ch. 6), which is a material where Li diffusion is very fast and quasi one dimensional. Rutile has potential uses as an anode in Li-ion batteries. Based on our measurements, we were able to show that Li^+ gets trapped upon reaching the (001)-surface of rutile, which is very hard to establish with other techniques and might be causing the reported difficulty of Li^+ intercalation in bulk rutile. Furthermore, we found that the diffusivity of Li^+ in

rutile follows a bi-Arrhenius relationship. At high- T , the corresponding Arrhenius component is in agreement with what other techniques (including β -NMR) have found. Below ~ 200 K, a second Arrhenius component becomes dominant, which has an activation energy similar to what was found with β -NMR below 100 K as part of a Li-polaron complex [29], as well as close to the activation energy calculated theoretically [44].

This is the only direct method for studying nanoscale Li diffusion and therefore might be proven very useful in understanding the motion of Li^+ interstitials through various materials and their interfaces, as well as in the pursuit of next-generation Li-ion battery materials, the importance of which is described in the next part of this introduction.

1.2 Li-ion Diffusion - Solid State Li-ion Batteries

1.2.1 Importance of Li-ion Batteries

The current global fossil-fuel-based economy poses a series of economical, political and environmental risks to the planet, which include the depletion of key energy sources, the risk of politically-induced fuel price crisis (similar to the 1973 oil crisis), as well as the potentially devastating results of the ongoing (man-made) climate change. Indeed, the global CO_2 emissions have increased dramatically over the past few decades, despite the efforts by the international community to contain them (Kyoto 1997 protocol, Paris 2015 accords). To avoid (or at least mitigate) the above crisis, a strong turn towards clean energy solutions is required, both in the energy production and in the transportation sectors. A key issue in both cases is to find feasible ways to store electrical energy.

Given that the most mature renewable energy technologies are wind and solar, which are generally not readily available when the demand is high, highly efficient energy storage systems integrated with the electric grid are required for a real shift towards renewable energy. Electrochemical storage systems (i.e., batteries and capacitors) are able to store the surplus energy from renewable energy power plants to be used when the electricity demand is higher than the supply [45]. Batteries in particular are highly efficient in storing energy and have long lifetimes, with Li-ion batteries being able to provide a higher energy return factor than other types [46].

Turning to the transportation sector, sustainable transport requires the replacement of the internal combustion engine (ICE) by zero (or low) emission vehicles, such as electric vehicles (EVs) and hybrid electric vehicles (HEVs). These require power sources with high output and energy density, as well as fast charging times. Li-ion batteries play already a key role as power sources in HEVs and EVs, as they are considered the best available option [47]. Indeed, over the last few years Li-ion

powered vehicles moved very successfully from proof-of-principle prototypes to widely used commercial products (see Fig. 1.1) [48, 49].

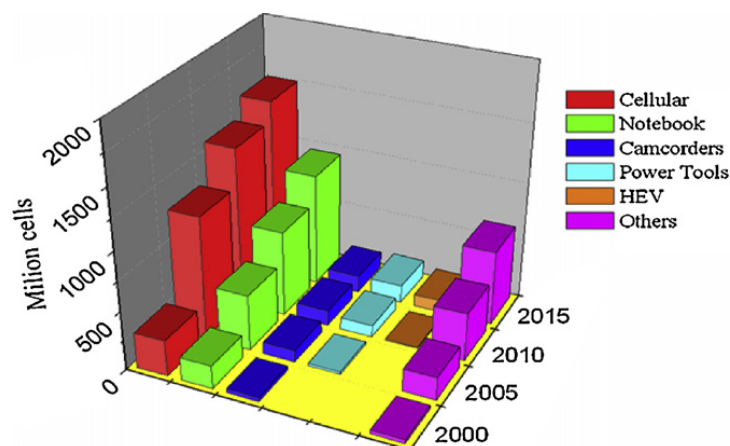


Figure 1.1: Li-ion battery market expansion (2000-2015). Adapted from Ref. [50].

Conventional Li-ion batteries have a graphite anode, a lithium metal oxide cathode (e.g., LiCoO_2 , LiMO_2) and a liquid or polymer gel electrolyte, which is a solution of lithium salt in an organic solvent (such as LiPF_6 in EC-DMC). The working principle of such a battery involves the (reversible) transport of Li^+ between an anode through the electrolyte towards a cathode. A schematic of a conventional C/ LiCoO_2 battery can be seen at Fig. 1.2.

When the battery is charged, the lithium ions are stored in the anode. During discharging, lithium ions diffuse through the electrolyte and separator diaphragm and into the cathode, where Co ions change valence to accommodate the oxidized Li^+ . The resulting charge imbalance drives the flow of electrons in the external circuit through the load. Note that in order to avoid short circuiting the current through the load circuit, the electrolyte has to be able to conduct the Li ions but at the same time be an electrical insulator. During charging, a voltage is applied to drive electrons back to the anode which causes the lithium to diffuse from the cathode back into the anode.

These conventional Li-ion batteries work with a typical voltage of $\sim 4\text{ V}$ and a specific energy 100 Whkg^{-1} to 150 Whkg^{-1} [51].

Conventional Li-ion batteries present, however, a number of challenges. These include low energy density, high cost, as well as relatively fast aging [53]. These characteristics ultimately relate to the motion of Li^+ interstitials in such materials, in terms of how fast Li^+ diffuses, but also to the extent of Li uptake and intercalation, the effect of Li concentration on its motion, as well as its fate as it diffuses to

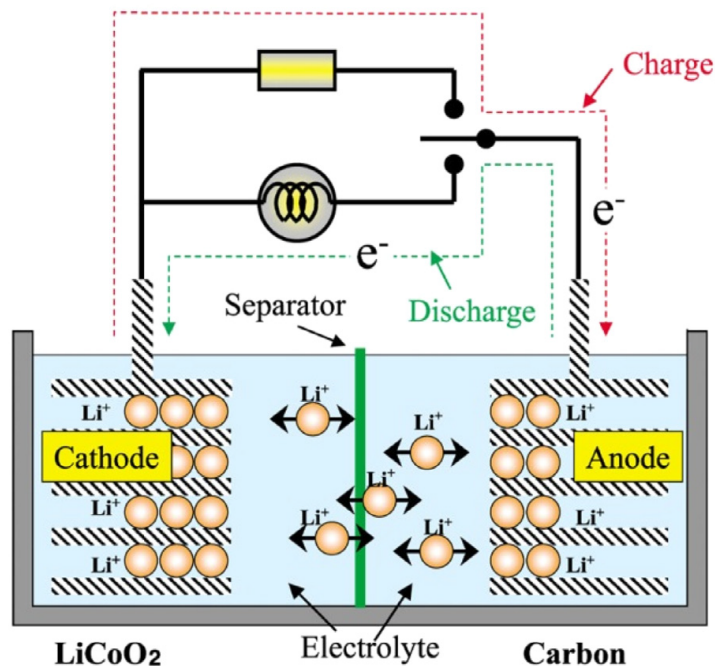


Figure 1.2: Schematic of a (C/LiCoO₂) Li-ion battery. Adapted from Ref. [52].

the interfaces of such materials. In particular, diffusion of lithium ions inside materials used in Li-ion batteries is important, since it ultimately determines the charging/discharging rate of the battery.

The need to overcome these drawbacks, as well as to enhance Li-ion batteries' relative advantages, motivates the search and study of novel electrode materials with superior characteristics. To that end, present-day research efforts focus on finding materials to replace current electrode and electrolyte materials with others having better characteristics in terms of cost, energy/power, safety and lifetime. Replacement materials for the graphite and LiCoO₂ electrodes should have a higher energy density and/or lower cost, whereas a replacement of the liquid electrolyte solution with a solid electrolyte would result in safer Li-ion battery systems, since the liquid electrolytes tend to be more susceptible to fires and hydrogen gas liberation.

To be able to identify potential Li-ion battery materials with superior characteristics, experimental techniques capable of studying Li diffusion in different systems and under different conditions are required. Sect. 1.2.2 describes the most commonly used methods for studying Li diffusion in scales of μm and above and Sect. 1.2.3 the techniques capable of investigating nanoscale Li diffusion.

In addition, understanding the characteristics of the Li motion across interfaces

of materials is also of great importance, as in an actual battery Li^+ will have to be able to seamlessly move across material boundaries to diffuse from one electrode to the other across the electrolyte.

1.2.2 Experimental Methods for Studying Solid State Diffusion

Many experimental techniques have been used to study diffusion in solids. These are generally split into *direct* and *indirect* methods (see Fig. 1.3).

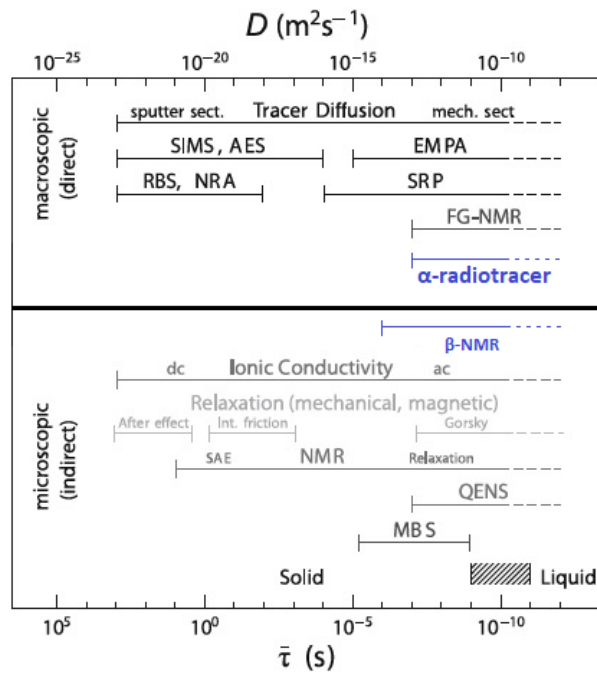


Figure 1.3: Direct and indirect methods for studying solid state diffusion with their ranges in terms of diffusivity (D) or mean residence time ($\bar{\tau}$). Adapted from Ref. [54] with the addition of β -NMR and α -radiotracer (in blue).

The direct methods rely on Fick's laws (see Ch. 4) and relate directly to the macroscopically defined diffusion coefficient D . In this sense, they can be thought of studying macroscopic (or long-range) diffusion. Important examples of such techniques include the radiotracer method [55, 56], secondary ion mass spectroscopy (SIMS) [57], electron microprobe analysis (EMPA) [58] and field gradient NMR [59]. Spreading resistance profiling (SRP) is used to study dopant diffusion in semiconductors. It can be considered to be a direct method as it can generate a depth profile for the spreading resistance, even though it requires a

transformation to convert that into a concentration profile. The technique developed as part of this thesis, namely the nanoscale ^8Li α -radiotracer method, also belongs in this category.

Even though most NMR techniques study diffusion indirectly (see below), field-gradient NMR (FG-NMR) is considered as a direct method. It employs a field gradient (either static or pulsed) over the sample and permits thusly the measurement of macroscopic diffusion without the need of invoking an atomistic model for the diffusion. FG-NMR, just like all NMR techniques – with the exception of β -NMR – require big samples and therefore is not applicable for nanoscale diffusion measurements, as it is limited by the gradient (dB_0/dz) that can be produced.

The radiotracer method is the most commonly used technique for studying self diffusion in solids, provided that radioactive isotopes of the diffusing element with suitable half-lives exist. This technique studies diffusion by introducing tracer quantities of the radioisotope at one side of the sample (see Fig. 1.4). After some time, the sample is cut in slices and the diffusion coefficient is extracted by measuring the radioactivity of each slice. Even though this technique is suitable over a large range of diffusion coefficients, it is not applicable for nanoscale diffusion. Moreover, it cannot study Li diffusion, because of the lack of suitable radioisotopes – the Li radioisotope with the longest half-life is ^8Li , but its 0.8 s half-life is not sufficient for this method –.

There are variations of the above technique, which use non-radioactive tracers with mass spectroscopy detection instead of radioactivity and are therefore able to study Li diffusion. They follow the steps outlined at Fig. 1.4, but they measure the density of the imported tracer in each slice by some other means, e.g., by optical absorption [60].

The rest of the direct techniques are of a narrower scope and applicability. SIMS uses sputter profiling and is therefore capable of studying low diffusivities over small diffusion scales. Auger electron spectroscopy (AES) is only able to study the diffusion of foreign atoms, as it cannot distinguish between different isotopes. Rutherford back scattering (RBS) is well suited for the study of heavy solutes in light solvent, in contrast with nuclear reaction analysis (NRA), which can study light solutes, provided that there is a suitable nuclear reaction with a narrow resonance.

On the other hand, *indirect methods* are techniques for studying diffusion that are not directly based on Fick's laws. They rather infer the diffusion rate of atoms in a solid by measuring phenomena related to the atomic motion. They directly measure atomistic quantities such as correlation and relaxation times(rates), line-widths, etc. From these, the hop rate τ_0^{-1} is extracted, which in turn is translated into a macroscopic diffusion rate using Einstein-Smoluchowski's law (see Sect. 4.2.3).

Most of the indirect methods are based on nuclear or radioactive signals and probes. One important exception is impedance spectroscopy (IS) [61], which

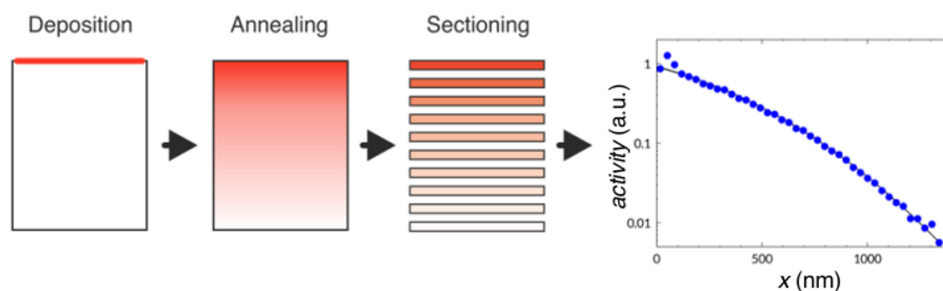


Figure 1.4: The steps for measuring diffusion with the (radio)tracer method. First the tracer is deposited at one surface, then the sample is annealed for some time. Finally, it gets sliced in thin layers and the tracer quantity of each slice is measured. From that, the diffusion coefficient can be extracted. Adapted from Ref. [54]. In contrast, both β -NMR and the ^8Li α -radiotracer method are non-destructive to the sample.

measures the complex electric impedance of the material under study versus AC frequency. Mössbauer spectroscopy (MBS) is not widely applicable because of the small number of Mössbauer isotopes. The most important of them is ^{57}Fe , which makes possible to study Fe diffusion with MBS [62]. Quasi-elastic neutron scattering (QENS) [63] can be also used to study fast diffusion rates, provided that the material of interest has isotopes with large quasi-elastic scattering cross-sections.

Nuclear magnetic resonance (NMR) along with spin-lattice relaxation spectroscopy (SLR) [54] are widely used to infer diffusion rates. They are applicable in a broad range of diffusivities and for a large selection of diffusing species. These techniques employ the nuclei of certain lattice atoms as spin-probes and they use the line-width of the resonance and/or the spin-lattice relaxation rate to extract the diffusion rate of interstitial ions.

1.2.3 Studying nanoscale Li diffusion

Nanostructured Li-ion battery materials (nanoparticles, nanofibers, thin-films, etc) have been found to exhibit substantially increased mass transport capabilities [64–67] compared to their bulkier forms, leading to enhanced electrode charge-discharge rates. This stems from the shorter diffusion lengths for Li^+ transport between the different parts of the battery, but also because of the much larger electrode-electrolyte contact areas, that allows for a highly increased lithium intercalation.

Even though there are many techniques capable of studying Li diffusion, very few of them are applicable to study Li diffusion at the nanoscale – or in nano-sized samples – and all of them are indirect. They include impedance spectroscopy

(IS) [68], low-energy muon spin rotation (LE μ SR) [69] and β -detected nuclear magnetic resonance (β -NMR) [22, 29].

In the literature, there are many cases of materials that the various methods yield diffusion rates differing by many orders of magnitude under the same conditions, e.g., in rutile TiO₂ [29, 60, 68, 70–73], or in LiCoO₂ [74–76]). A direct method applicable to the nanoscale could potentially shed light on these discrepancies.

To that end, we developed a spin-off of the classical radiotracer method, namely the ⁸Li α -radiotracer method, which uses the attenuation of the (grand)daughter α -particles coming from the radioactive decay of ⁸Li, in order to study nanoscale Li diffusion.

This direct method for studying Li diffusion differs from conventional radiotracer diffusion experiments in several key areas: it is non-destructive to the sample; it is sensitive to atomic motions over the nanometer length scale [56, 76–78]; and it is amenable to the use of short-lived radioisotopes with relatively short half-lives $\tau_{1/2}$ (Li has no radioactive isotopes with $\tau_{1/2} \gg 1$ s). It makes use of a focused 3 mm diameter low-energy ⁸Li⁺ ion beam to inject a target material with the radiotracer atoms. Both during and following the beam pulse, the temporal evolution of the α -decay signal is monitored, whose yield and shape are correlated to the rate of arrival at the crystal surface and the details of the diffusion boundary conditions (e.g., a reflective or absorptive surface).

Such a technique has been developed in Japan for micrometer Li diffusion [79–83] and recently also for nanometer-scale studies [56, 76–78]. As part of this thesis, a new incarnation of the above technique has been developed (Ch. 5 and Ch. 6), sharing many characteristics with its Japanese version, but also having key differences (see Ch. 5). This method is demonstrated not only to be able to extract the nanoscale diffusion rate of Li ions, but also to indicate what happens to Li ions when they reach the sample surface.

1.3 Organization of this Thesis

This thesis presents the recent developments on using ⁸Li as a probe in condensed matter physics. For the case of β -NMR, we show how comparing ⁸Li and ⁹Li one can determine the source of spin relaxation. In addition, we show that the α -particles emitted as part of the decay process can be used to track the motion of ⁸Li or to enhance the beta-decay asymmetry of ⁹Li.

Chapter 2 is intended as an introduction to β -NMR. It includes an outline of the physical basis of the method, a synopsis of the experimental infrastructure employed, as well as a presentation of the different types of measurements that are used in this work.

Chapter 3 then presents the development of the α LithEIA isotopic comparison method, which makes use of ^8Li and ^9Li beams to identify the source of spin-lattice relaxation in β -NMR. This new tool for β -NMR can be very useful in cases that it is not clear whether the primary source of relaxation in a sample is of electric or magnetic origin. However, ^9Li β -NMR is much more time-consuming and tedious (compared to ^8Li), due to the suppressed asymmetry signal associated with that isotope. To amend this issue, the α LithEIA method was developed, which tags the ^9Li β -decays in coincidence/anti-coincidence with an α -particle and is shown to enhance the ^9Li β -NMR signal by a factor of ~ 2 (and theoretically it can enhance it by a factor of ~ 3).

Chapters 4–6 outline the other application of using the α -decay signal in β -NMR, namely studying Li diffusion at the nanoscale (i.e., the ^8Li α -radiotracer method).

Chapter 4 provides the theoretical background of interstitial diffusion theory, both from a macroscopic and a microscopic point of view.

The basis of the ^8Li α -radiotracer method is covered in Chapter 5, which presents the calculations and Monte Carlo simulations which were carried out as part of this work to establish the feasibility of the technique, as well as to provide the tools needed for the extraction of the diffusion coefficient from the experimental data.

Chapter 6 follows the development of the ^8Li α -radiotracer technique by presenting the study of Li diffusion in rutile TiO_2 . With these measurements, we were able to extract both the diffusion coefficient of Li in various temperatures, as well as the energy barrier for Li diffusion. In addition, our measurements show that Li^+ has a high probability ($\geq 50\%$) to get trapped upon reaching the (001)-surface of rutile.

Finally, Chapter 7 summarizes the above results and identifies possible future work to further develop this study.

This thesis contains material taken from three of the author's papers [1–3]. Chapter 2 and 3 are partially taken from References [1, 2], while Chapter 5 and 6 contain material from Reference [3]. This introductory Chapter also partially incorporates material from all these papers.

Chapter 2

Beta-detected Nuclear Magnetic Resonance

This Chapter is intended to be a short introduction to the β -NMR technique, by discussing the physics behind it (Section 2.1), the details of the radioactive, spin-polarized beam production and delivery to the spectrometers (Section 2.2), the interactions of the spin-probes with their environment once inside the material under study (Section 2.3), as well as the experimental modes used to infer these interactions (Section 2.4). Finally, Section 2.5 presents the merits of using the information from the α -decay in parallel to the β -decay in order to enhance the capabilities of β -NMR, which is the primary focus of this thesis.

2.1 Physics of β -NMR

The basis of β -NMR is the parity-violating (nuclear) weak interaction, whereby the direction of the emitted electron (positron) from the decaying nucleus is correlated with the nuclear spin polarization at the time of decay:

$$W(\theta) = 1 + \beta a p \cos(\theta) \quad (2.1)$$

where $\beta = v/c$ is the velocity of the high energy electron (positron) normalized to the speed of light, p is the magnitude of the nuclear polarization vector, θ is the angle between the nuclear polarization and the electron (positron) velocity and a is the asymmetry parameter depending on the properties of nuclear β -decay (see Fig.2.1).

The resulting anisotropic decay pattern for the high energy electron allows one to monitor the nuclear polarization from highly polarized ${}^8\text{Li}^+$ beams (or other β -NMR nuclear probes) implanted in the sample. In particular, the asymmetry in the count rate at time t between two opposing β -detectors is proportional to the component of nuclear polarization along the direction defined by the two detectors:

$$A(t) = \frac{N_B(t) - N_F(t)}{N_B(t) + N_F(t)} = A_0 p_z(t) \quad (2.2)$$

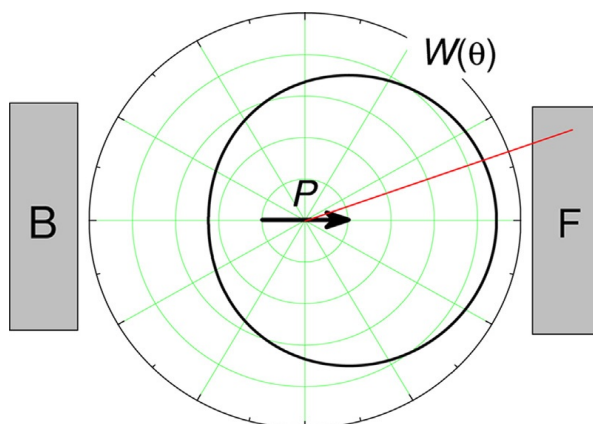


Figure 2.1: Anisotropy of the direction of the emitted β -particle based on the polarization of the parent nucleus. The asymmetry of β -counts at two opposing detectors (B and F) can be used to monitor the degree of nuclear polarization versus time. Adapted from Ref. [22].

where $N_B(t)$ and $N_F(t)$ are the counts measured in the backward and forward detectors, $p_z(t)$ is the component of nuclear polarization along the z -axis defined by the detectors, and t is the time of decay after implantation. The detectors are generally positioned so that z is along the direction of initial polarization.

Note that the asymmetry in the count rate has a maximum value of A_0 at $t = 0$ which is reduced relative to the theoretical asymmetry a , as calculated from the nuclear properties, owing to instrumental effects such as the finite solid angle subtended by the detectors and scattering of the β -particles before reaching the detectors. Note also that $p_z(t)$ and thus $A(t)$, are time dependent, reflecting the fact that the nuclear polarization is subject to spin relaxation processes in the sample (see Sec. 2.3), which in fact is the quantity of interest in a β -NMR experiment.

By changing the energy of the beam (between 0.1 keV to 30 keV) the mean implantation depth can be tuned in a range of approximately 10 nm to 200 nm. Thus, it is possible to perform depth-resolved experiments, which makes this technique ideal for the study of near-surface phenomena [19] (see Sec. 2.2.3).

The most commonly used β -NMR isotope at TRIUMF is ${}^8\text{Li}$, which has a lifetime of $\tau = 1.21$ s, spin $I = 2$, gyromagnetic ratio $\gamma = 6.3015 \text{ MHz T}^{-1}$, and a relatively small –but non-zero– electric quadrupole moment $Q = +32.6 \text{ mb}$ [84]. The fact that ${}^8\text{Li}$ is not a purely magnetic probe makes it possible to study electric quadrupolar phenomena. Moreover, the theory of nuclear β -decay predicts that the theoretical asymmetry parameter a (Eq. 2.1) of ${}^8\text{Li}$ is about 1/3.

Typical radionuclides that have been used as β -NMR probes can be seen at

Tab. 2.1. This thesis focuses exclusively on ${}^8\text{Li}$ and ${}^9\text{Li}$.

Table 2.1: Intrinsic nuclear properties of radioisotopes used in β -NMR. I^π is the nuclear spin (and parity), μ is the magnetic moment, and Q is the electric quadrupole moment. When Q is non-zero, the probe is sensitive to the local electric field gradient else it is sensitive to the local magnetic field alone.

	I^π	τ_β (s)	μ (μ_N)	Q (mb)
${}^8\text{Li}$	2^+	1.2096(5) [85]	+1.653560(18) [86]	+32.6(5) [84]
${}^9\text{Li}$	$3/2^-$	0.2572(6) [87]	+3.43678(6) [86]	-31.5(5) [84]
${}^{11}\text{Be}$	$1/2^+$	13.74(8) [88]	-1.6813(5) [89]	-
${}^{31}\text{Mg}$	$1/2^+$	0.236(20) [89]	-0.88355(15) [90]	-

${}^8\text{Li}$ β -decays to the first excited state of ${}^8\text{Be}$, which in turn decays with a short mean lifetime of 3.01×10^{-22} s into two α -particles, emitted at an angle of 180° in the center-of-mass frame of the ${}^8\text{Be}$ daughter nucleus (Eq.(2.3)).



The average energy of the emitted β is ~ 6 MeV, but due to the three-body decay kinematics, it varies continuously between 0 MeV to 12.5 MeV, with the upper limit defined by the Q-value of the decay and the mass of ${}^8\text{Be}$ (Fig. 2.2a). The mean energy of the emitted α -particles is 1.6 MeV with a full width at half maximum of 0.6 MeV due to lifetime broadening. Because of quantum mechanical mixing of the first and the higher excited states of ${}^8\text{Be}$ [91], the energy spectrum of each α -particle has an asymmetric high energy tail (Fig. 2.2b).

2.2 Experimental Details of β -NMR at TRIUMF

This section describes the process of how TRIUMF produces and delivers to the experimental spectrometer(s) a clean, highly-polarized, intense beam of the required isotope (Sect. 2.2.1). The next part then gives a detailed description of the characteristics of the high-field and low-field β -NMR spectrometers (Sect. 2.2.2).

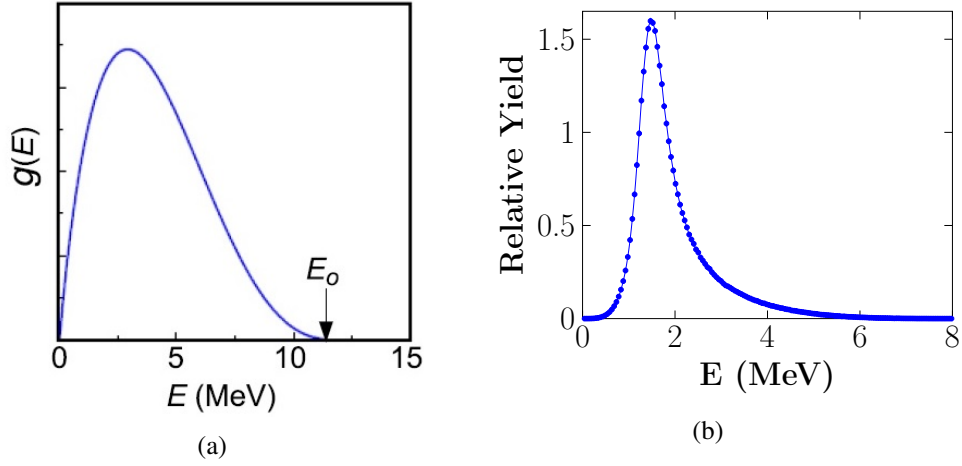


Figure 2.2: Energy distribution of the β -particles (*left*) coming from the decay of ${}^8\text{Li}$ (Adapted from Ref. [92]) and that of the α -particles (*right*) coming from the subsequent decay of ${}^8\text{Be}$ [93].

2.2.1 Polarized Beam Production and Delivery

At TRIUMF, the first step towards the production of the spin-polarized radioactive beam of the specific β -decaying isotope required for the β -NMR experiments (e.g., ${}^8\text{Li}$, ${}^{31}\text{Mg}$, etc) is to extract and accelerate a beam of negatively charged hydrogen ions. An ion source ionizes hydrogen gas to produce H^- ions, which get initially accelerated by a sixty-meter-long electrostatic linear accelerator. This beam is then injected into the main 520 MeV cyclotron (see Fig. 2.3).

The main cyclotron accelerates the negatively charged hydrogen ions using an alternating electric field with a frequency of 23 MHz and a 4000-Tons six-sector normally-conducting magnet made of iron. The magnet produces a magnetic field of 0.56 T using 18 500 A of current. The Lorentz force produced by the combination of the electric and magnetic fields accelerates the ions up to 75% of the speed of light after 1500 revolutions in an outward spiral trajectory inside the cyclotron tank. At the end of the acceleration process, the ion beam passes through a thin carbon foil, which strips the two electrons from the negatively charged ions to produce bare protons. This process reverses the charge of the accelerating beam, which, in turn, reverses the direction of the cyclotron motion and guides the ion beam out of the cyclotron and into the post-acceleration beamline. This extraction process increases the efficiency of the main cyclotron significantly, relative to extracting a beam of bare protons, allowing for a more intensive beam to be produced (up to $\sim 100 \mu\text{A}$).

The beam of 520 MeV protons is then directed towards the Meson Hall, or the



Figure 2.3: Internal view of the 520 MeV main cyclotron vault at TRIUMF. Notice the size of the vault compared to the man at the center. Adapted from Ref. [94].

ISAC facility. In the Meson Hall, it is used to treat ocular melanoma of cancer patients, by selectively depositing the proton's energy in the tumor [95], or it bombards a suitable solid target, which creates a secondary beam of pions which further decays into a muon. The muons are used to study the properties of materials with the μ SR technique [96].

When a beam of a specific isotope is requested, the proton beam is directed towards the Isotope Separation and Acceleration (ISAC) facility [97], where it collides with a carefully engineered target and creates a variety of isotopes [98] by nuclear spallation. The target is chosen to enhance the production and release of the desired isotope(s) and is made, amongst others, by Tantalum (Ta), SiC or Uranium(U)/Uranium Carbide(UC). Ta is the optimal target for production of alkali metals such as ^8Li . The target is kept at a temperature of ~ 2000 to 2500 $^{\circ}\text{C}$ and a positive voltage of 28 to 30 kV. The high temperature allows the newly formed isotopes to diffuse fast to the surface of the target and exit the target vessel through a tube of 1-2 mm diameter. For the production of short-lived isotopes – with half life ~ 10 μs – keeping this diffusion time short can be critical. This is yet another motivation for trying to understand diffusion in solids (see Ch. 4-6).

The positive potential of the target (relative to the grounded extraction electrode) accelerates the ions leaving the target via the small diameter tube and forms an intense beam with a cross section of a few mm, moving towards a high-precision magnetic mass separator. The magnetic field bends the trajectories of the different isotopes by a different angle (depending on their momentum/mass) thereby ensuring that only ions of the desired isotope reach the experiment. ^8Li is very easy to mass-separate, since there are no stable isotopes with a similar mass. Using a typical proton beam current of 40 μA , the ISAC target can seamlessly provide a $^8\text{Li}^+$ beam

with an intensity of 10^8 ions/s.

Before reaching the β -NMR experimental spectrometer(s), the radioactive beam is (nuclear-)spin-polarized in flight by a single-frequency dye laser [39]. This technique is able to polarize the ^8Li ions to a $\sim 70\%$ [99] level.

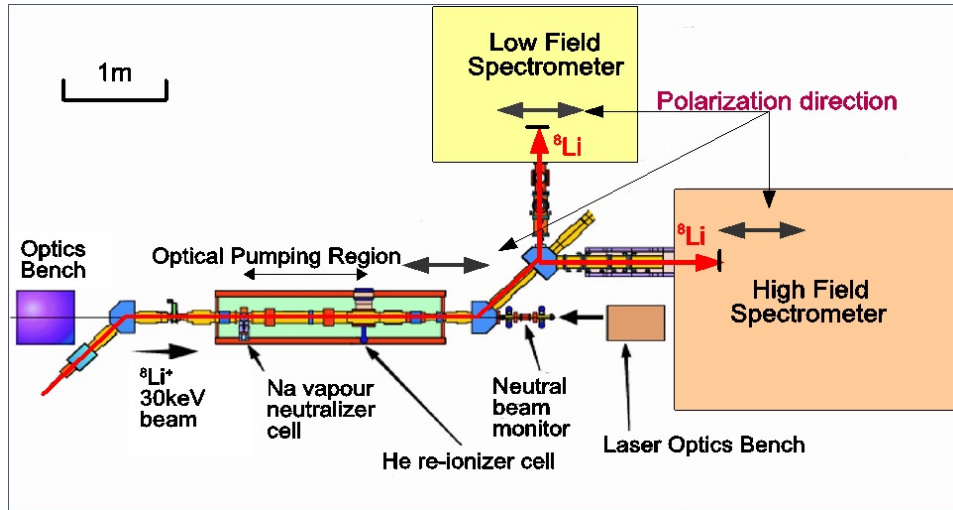


Figure 2.4: Schematic of the polarizer and the section of the beamline leading to the β -NMR and β -NQR spectrometers. Note that the neutralizer cell is currently filled with Rb vapor, not Na. Adapted from Ref. [39].

The first step towards producing a highly spin-polarized beam is to neutralize the beam by passing it through a cell filled with Rb vapor, held at a temperature of $\sim 250^\circ\text{C}$. The Rb vapor is confined in the cell using a recycling jet target. Alkali metals can easily lose one electron to the positively charged ions, thus they effectively neutralize the beam with a typical efficiency of 50%. The neutralized beam then drifts by 1.9 m inside the optical pumping region, whereas the part of the beam that failed to get neutralized is dumped into a Faraday cap by a pair of electrostatic reflection plates. A small longitudinal magnetic field (~ 2 mT) is present inside the optical pumping region, for the purpose of defining the polarization axis. The neutralized beam overlaps with a laser beam created by a dye laser source, counter-propagating in the polarizer beamline. The laser light is circularly polarized with respect to the polarization axis – which is also the axis the beam is propagating on – and is tuned to the Doppler-shifted D1 transition close to 671 nm for ^8Li (see Fig. 2.5). This wavelength corresponds to the energy needed for the transition from the ground state $^1\text{S}_{1/2}$ to the first excited state $^2\text{P}_{1/2}$ of ^8Li . Because the ground state of ^8Li is split into two hyperfine levels, as is the case with many alkali isotopes,

to achieve a high level of polarization, the light has to be tuned at both sub-levels' wavelengths. For the polarization of other isotopes/elements the laser frequencies are tuned using similar considerations.

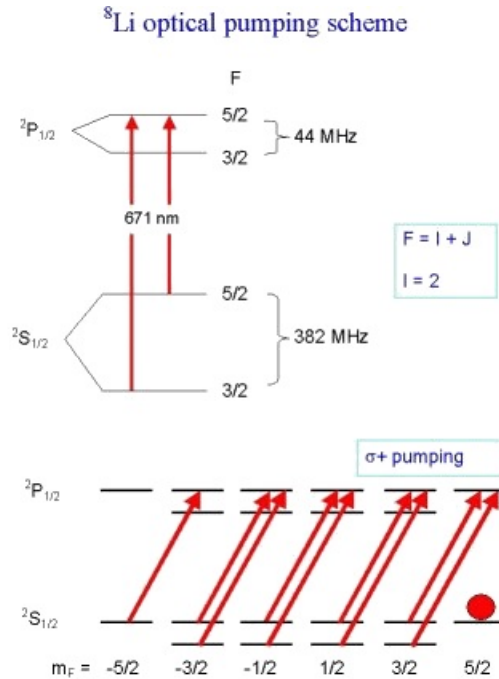


Figure 2.5: Schematic of the spin polarization method for ⁸Li. The upper image shows the ground state and first excited state with their hyperfine splittings. The lower image shows the pumping of the positive helicity (σ^+) after a few cycles of optical pumping. Adapted from Ref. [100].

The Zeeman splitting due to the small longitudinal magnetic field further splits the hyperfine levels to $2F+1$ sub-levels m_F , where $F= I+J$. In the lower part of Fig. 2.5, the effect of illumination with σ^+ (i.e., positive helicity) circularly polarized laser light is shown. The only allowed absorptions are the ones that increase the magnetic quantum number m_F by $+1$. This effect populates gradually the highest angular momentum state of $+5/2$, with both nuclear and electronic polarization having their highest permitted value. Spontaneous fluorescence – which is allowed for transitions satisfying $\Delta m_F=0, \pm 1$ – has a lifetime of 27 ns, thus, the drifting time through the optical pumping region ($\sim 2 \mu\text{s}$) allows for the ⁸Li atoms to go through dozens of pumping cycles of laser light absorption and fluorescent emission.

The net effect of this process is that the ⁸Li nuclei are nuclear-spin-polarized

and the majority ends up at the nuclear spin state $m_I=+2$ (-2 for the σ^- helicity). This corresponds to a high level of nuclear polarization ($\sim 70\%$), which is defined as:

$$P(t) = \frac{1}{I} \sum_{m_I} m_I p_{m_I}(t) \quad (2.4)$$

where m_I is the nuclear spin quantum number, $P(t)$ is the nuclear polarization (along the axis defined by the external magnetic field) versus time and $p_{m_I}(t)$ corresponds to the population of the m_I -th state at that point in time.

After the polarizing process, the neutral beam enters into a cell filled with cold He gas that re-ionizes the ions with an efficiency of about 1/2. The part of the beam that is left neutral is dumped at the neutral beam monitor (NBM) – made by a thin palladium foil – which measures its intensity and polarization. The re-ionized part of the beam is steered by an electrostatic bender, which delivers it to either the high-field or the low-field spectrometer, referred usually as the β -NMR and β -NQR spectrometers, respectively. These electrostatic benders do not affect the polarization direction, which is determined by the helicity of the laser beam directed along the axis of the polarizer.

The section of the beamline after the polarizer leading to the β -NMR spectrometer includes three Einzel lenses, which electrostatically focus the beam to the center of the sample. Two sets of manual slits can be used to collimate the beam and reduce the beam spot on the sample. The size and the position of the beamspot is a very sensitive function of a large number of parameters. The beam is accelerated to a certain energy when extracted from the ISAC target and its trajectory and size are influenced by the upstream elements (Einzel lenses, magnetic quadrupoles), as well as the magnetic field B_0 inside the spectrometer. If the beam reaches the spectrometer perfectly centered on the magnet axis of the superconducting solenoid, then the Einzel lenses and the bias voltage of the sample should not affect its trajectory. In reality it is very hard to tune the beam to arrive perfectly, so the combined effect of the magnetic field and the electrostatic bias results into a spiraling motion leading to a beam spot which depends slightly on the magnetic field and the deceleration potential.

To ensure a good beamspot in all required magnetic fields and electric biases, before the start of the experiments, the ISAC operator tunes the EM elements of the beamline with ${}^7\text{Li}^+$ until good beam transport is achieved and then fine-tunes the last downstream elements using a ${}^8\text{Li}^+$ beam until a centered, adequately small beamspot is achieved in all required conditions. For each condition (magnetic field and electrostatic bias) the beamspot is imaged by a charge-coupled device (CCD) camera lying outside vacuum behind an optical port, using a scintillating

sapphire at the sample position. The camera images the front surface of the sample using a mirror installed inside the main chamber which bends the optical path by approximately 90° .

2.2.2 β -NMR and β -NQR Spectrometers

For all the experiments related to this thesis, TRIUMF's dedicated β -NMR and β -NQR spectrometers were used. In both spectrometers, the sample material is kept under ultra high vacuum (UHV) at the end of ISAC's beamline. A superconducting magnet can generate a magnetic field of up to 9 T around the sample of the high-field β -NMR spectrometer, pointing along the probe ions' spin polarization. A regular conducting Helmholtz magnet is capable of creating a field of 0-20 mT (i.e., 0-200 Gauss) at the low-field β -NQR spectrometer. The platforms on which the spectrometers are positioned are electrically isolated from ground so they can be raised to several kV, effectively increasing the electric potential of the samples. This way, the mean implantation depth of the radioactive beam inside each sample crystal can be controlled by the applied platform voltage [101]. In this section, the characteristics of these two instruments will be presented. As part of this thesis, an upgraded version of the β -NQR cryostat – the so-called “cryo-oven” – was designed and fabricated. Its specific characteristics can be found in Appendix A.

2.2.2.1 The β -NMR spectrometer

The high field spectrometer, usually referred to simply as the “ β -NMR spectrometer”, has a longitudinal geometry, in the sense that the nuclear polarization and the direction of the external magnetic field all coincide with the direction of the beam's motion and they are perpendicular to the surface of the sample under study.

The β -NMR apparatus is a cold finger UHV-compatible cryostat from Oxford Instruments (see Fig. 2.6), capable of maintaining a vacuum of up to 10^{-10} Torr. This level of vacuum is achieved via a system of load locks that allow for changing the sample without venting the main chamber. To change the sample, the cryostat is driven back by a motor that stretches a bellows, out of the bore of the superconducting magnet, until the sample holder port of the cryostat lies directly below the load lock and gate valve shown in the figure below.

The sample is mounted outside vacuum on an aluminum sample holder, at the end of a stainless steel rod (see Fig. 2.7). The typical size of β -NMR-compatible samples is 8 mm x 10 mm x 0.5 mm. Thin films, or samples of smaller sizes are mounted on a substrate (usually made of sapphire due to its high thermal conductivity and natural scintillation properties) by using UHV-compatible silver paint. The sample is then attached on the sample holder by two small Al clamps.

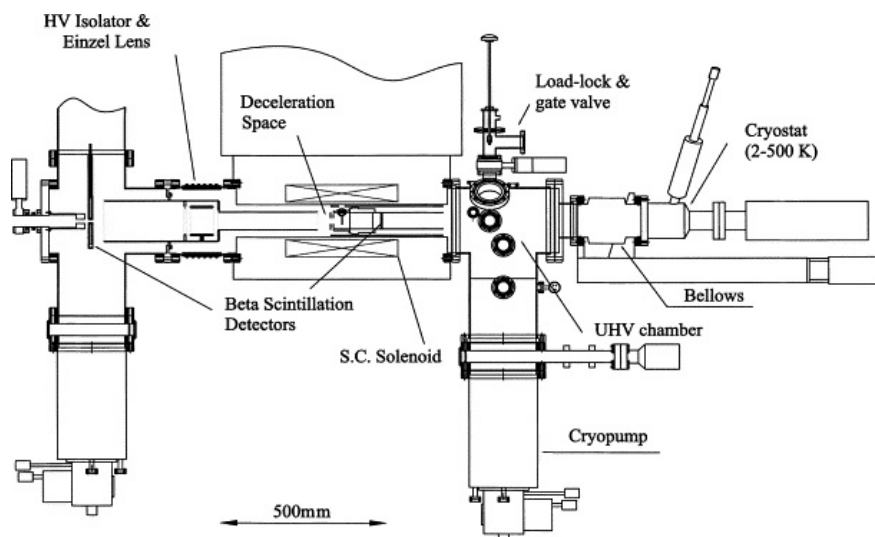


Figure 2.6: High-field β -NMR spectrometer. The ion beam enters from the left side, passing through the hole of the upstream scintillation detector and reaches the sample sitting at the center of the deceleration space with the polarization parallel to its momentum. A cryopump is used to maintain the UHV vacuum in the sample space and a cold finger cryostat to control the sample temperature. Adapted from Ref. [33].

The sample holder is mounted into the cryostat using a load lock so the main chamber can be maintained at UHV during sample changes. After the sample is mounted, the cryostat is driven back in the bore of the magnet. Typically a sample change requires between 45 min and one and a half hour.

The sample is positioned at the center of a superconducting solenoid magnet capable of generating a uniform static magnetic field B_0 of up to 9 T. Since the nuclear polarization is longitudinal, the β -detectors are positioned upstream and downstream of the sample and initial polarization direction (see Fig. 2.1). Both are plastic scintillation detectors. The downstream detector – the so-called “Forward detector” – lies outside vacuum behind a thin stainless steel window. The β particles easily pass through the window without much attenuation compared to their average energy (see Fig. 2.2a), but all α -particles are blocked. The upstream detector – the “Back detector” – has a hole in the middle to allow for the incoming beam to reach the sample. Due to the focusing effect of the strong magnetic field, the Back detector has to be positioned outside the bore of the magnet in order to allow the β particles to reach it, instead of moving further upstream by passing through its central hole. The two detectors cover very different solid angles in the absence of a

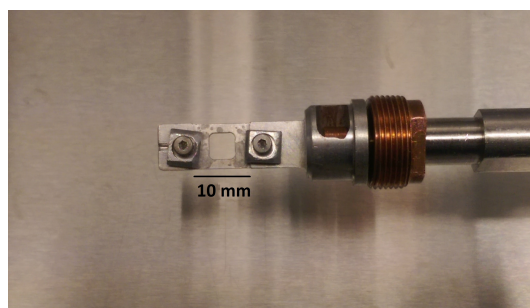


Figure 2.7: β -NMR sample holder. At the rightmost side the end of the sample rod is visible, on which the copper part of the sample holder is screwed. The sample is mounted on the sample holder using two small clamps.

magnetic field, but they have similar effective solid angles, when a high magnetic field is applied.

A non-resonant helical transmission line can generate a transverse radio-frequency (RF) field $B_1(t)$ in a range of frequencies ω up to 45 MHz. The direction of $B_1(t)$ is perpendicular to both the static magnetic field B_0 and the polarization of the beam. It is used for frequency-resolved experiments (see Sec. 2.4.1).

The temperature of the sample is controlled using a combination of liquid helium flow and a resistive heater. A Lakeshore temperature controller can automatically maintain the sample at a constant temperature by balancing the cooling power of liquid helium with the appropriate amount of current passing through the heater. This allows one to control the sample temperature in the range 3.5 K to 318 K. The whole apparatus sits on a platform, on which a biasing voltage of up to ± 30 kV can be applied.

2.2.2.2 The β -NQR spectrometer

The low-field β -NQR spectrometer differs from the high-field β -NMR spectrometer in several ways. In contrast with β -NMR, the geometry of the β -NQR spectrometer is transverse. The beam is implanted into the sample with its momentum normal to the sample's surface, but its nuclear polarization is perpendicular to its momentum, i.e., parallel to the surface of the sample-material. This is evident from Fig. 2.4 since the polarization is longitudinal in the polarizer. The two 45° benders in Fig. 2.4 are electrostatic and thus do not influence the direction of nuclear polarization.

The static applied field B_0 can be completely absent, permitting for zero-field experiments. For low-field measurements, B_0 is oriented (anti)parallel to the polarization of the beam. It is generated by passing current through a Helmholtz

coil, which creates a uniform magnetic field around the sample (of 0-20 mT) at the sample position.

A small vertical Helmholtz coil can generate a transverse RF field $B_1(t)$ in a range of frequencies from 0-2 MHz. The direction of this field is perpendicular to both the polarization of the beam and its momentum. In other words, if the beam momentum vector defines the z -axis of a lab-frame, then the polarization vector would be on the y -axis and the RF magnetic field on the x -axis (see Fig. 2.8).

As discussed in Sec. 2.1, the β -detectors should be positioned along the line defined by the initial nuclear polarization. Thus, in the case of the β -NQR spectrometer, they are to the left and right of the sample, lying outside vacuum behind two thin stainless steel windows. They are naturally referred to as the “Left” and “Right” detectors, respectively. They are fast plastic scintillators which convert the energy of the incoming β -particles into light, which is turned into electrical signal by a photomultiplier tube (PMT).

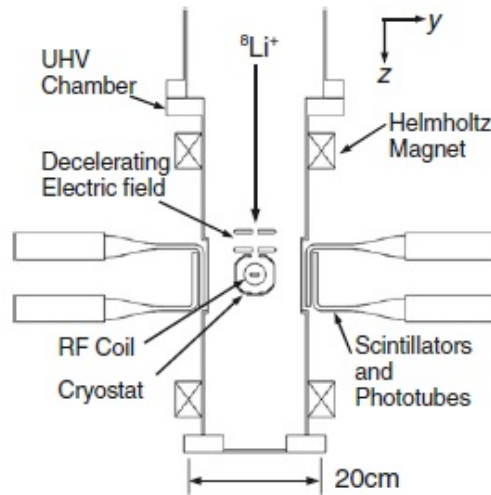


Figure 2.8: Over-view of the β -NQR spectrometer. The ion beam enters from the top of the figure (parallel to the z -axis), with its polarization along the y -axis, on which the two β -detectors are situated. Note that the coordinate system in this over-view is slightly unusual, as the z -axis is generally defined to be along the direction of the magnetic field and the nuclear polarization. Adapted from Ref. [33].

The samples are loaded into the cryostat from above, through a vacuum load-lock, using a long (~ 1.6 m) stainless steel rod and a process similar to that for β -NMR. The β -NQR sample holder has four sample positions (see Fig. 2.9). Each position can be filled with a sample of dimensions $12 \times 12 \times 0.5 \text{ mm}^3$ a priori,

reducing thus the number of sample changes needed during an experimental run period. Sample changes need to be done at ~ 300 K. Each sample change typically takes about 1-2 hours. The rod can be turned by hand from outside vacuum around the x-axis of Fig. 2.8, thus introducing an angle between the sample surface and the beam axis. This allows for angle-resolved experiments, which are crucial for studying electric quadrupolar phenomena [29].



Figure 2.9: The β -NQR sample holder (made of copper) with four samples mounted. In contrast to the β -NMR one, it has four sample stations, which reduces significantly the number of sample changes needed during an experimental run period.

Similarly to the β -NMR spectrometer, the temperature of the sample is controlled by a combination of liquid helium flow and a heater, using a Lakeshore controller to stabilize or change the temperature effectively. The lower thermal mass of this cryostat permits a much faster temperature change (tens of K/min) compared to the β -NMR cryostat (1-2 K/min). The β -NQR cryostat has a temperature range between 4.5 K and 300 K.

The β -NQR platform can be raised to a high voltage of 30 kV allowing the energy of implantation to be adjusted between 0.1 keV and 30 keV which corresponds to a mean implantation depth between about 10 and 200 nm.

2.2.3 Beam Implantation Profiles

Changing the energy of the ion beam through varying the β -NMR/NQR platforms bias voltage allows for depth resolved measurements. The higher the energy of the ion beam, the deeper the incoming ions stop on average. The energy range accessible with ISAC's ion beams permits for a mean implantation depth of 10 nm to 200 nm. This can be used to study, among other things, how the temperature of phase transitions depends on proximity to the sample's surface [19], the dynamics close to a buried interface of two heterostructures [20], studying the vortex lattice at a superconducting substrate [102], or long-range magnetic effects in thin films

caused by the proximity to a magnetic [103] substrate. In all these cases, it is paramount to know the depth profile of the β -NMR ion probes upon implantation.

The ion implantation (statistical) profile can be simulated using the *Stopping and Range of Ions in Matter* (SRIM) software. SRIM is a well established Monte-Carlo-based algorithm used extensively in condensed matter physics. It generates the statistical stopping distribution of the incoming ion beam by simulating the trajectory of each implanted ion individually (see Fig. 2.10). Each ion follows a different path due to stochastic processes, such as Rutherford scattering to different lattice ions resulting into abrupt changes in the direction of motion, as well as different momentum transfers between the incoming ions and the lattice.

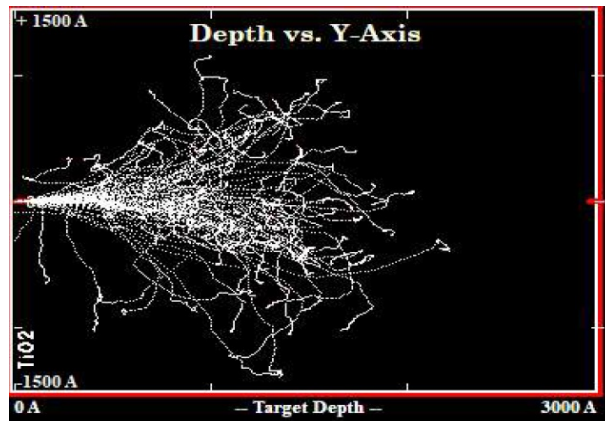


Figure 2.10: Example of ^8Li tracks after implantation in rutile TiO_2 , as simulated by SRIM-2013.

When the energy of the ion beam is increased, both the mean implantation depth and its standard deviation (also referred to as “ion straggle” in this context) of the stopping distribution increases. As an example, Fig. 2.11 depicts the depth profiles for $^8\text{Li}^+$ ions implanted in TiO_2 for different beam energies.

Comparisons between SRIM and experiments [104] show that for Li ions, 81% of the simulated profiles that were compared to experiments differ from the experimental points by less than 10% of the value predicted by SRIM.

A known issue with SRIM predictions is that it treats all target materials as being amorphous. In some instances, though, the crystalline structure of the target could provide some channeling paths for the incoming ions along specific directions. If such a direction differs from the implantation angle below a critical angle, then the channeling effect cannot be neglected and the actual implantation profile could have a large tail towards the bulk of the crystal, which would be absent in the SRIM calculation.

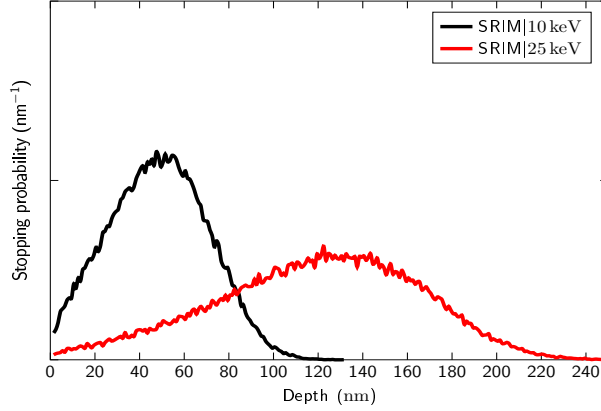


Figure 2.11: ^8Li beam implantation profile in TiO_2 as simulated by SRIM-2013 for a beam energy of 10 and 25 keV. By increasing the energy of the beam, both the mean implantation depth and the ion struggle increase.

The critical angle of channeling is given by [105]:

$$\psi \approx \sqrt{\frac{(Z_1 e)(Z_2 e)}{E(d/2)}} (\text{rad}) \quad (2.5)$$

where Z_1 is the atomic number of the ion beam, Z_2 that of the target material, $e^2 = 1.44 \times 10^{-5} \text{ MeV \AA}$, E is the energy of the beam (in MeV) and d is the effective distance of the target's atoms along the channeling pathway (in Angstroms).

The effect of channeling of lithium ions implanted along the c -axis of rutile TiO_2 will be discussed at Sect. 6.3.

Apart from the implantation profile itself, SRIM can also provide estimates on other processes, such as the mean number of ion/hole pairs created on the track of an ion, as well as the damage inflicted on the sample's lattice due to the implantation process.

2.3 Spin Interactions of β -NMR probes in a lattice

After implantation, the β -NMR probe stops at well defined interstitial position(s) where there is a minimum in the potential energy surface. The nuclear spin polarization will evolve in time according to a spin Hamiltonian which describes the interaction between the nuclear spin and the surrounding crystalline lattice.

There are two basic kinds of interactions described by the corresponding spin Hamiltonian. These can be generally categorized into magnetic (Sect. 2.3.1) and

electric quadrupolar interactions (Sect. 2.3.2), with the latter being applicable only for nuclear probes with a non-zero electric quadrupole moment.

2.3.1 Magnetic Interactions

The nucleus, which is a compound system consisting of neutrons and protons, has a characteristic magnetic moment μ proportional to its total angular momentum \mathbf{J} :

$$\mu = \gamma \mathbf{J} = \gamma \hbar \mathbf{I} \quad (2.6)$$

where γ is a scalar quantity called the gyromagnetic ratio, \hbar is the reduced Plank constant and \mathbf{I} is a dimensionless angular momentum (operator).

As discussed in Sec. 2.2.1, the application of a magnetic field \mathbf{B} lifts the degeneracy of the magnetic quantum number m to form the nuclear Zeeman states. The Hamiltonian defining this process is given by:

$$\hat{H}_m = -\mu \cdot \mathbf{B} \quad (2.7)$$

Without loss of generality, one can set $\mathbf{B} = B_0 \hat{z}$, so Eq. 2.7 can be rewritten as:

$$\hat{H}_m = -\gamma \hbar B_0 \hat{I}_z \quad (2.8)$$

Thus, the eigenvalues of Eq. 2.8 are the eigenvalues of \hat{I}_z , multiplied by a constant, i.e.:

$$E_m = -\gamma \hbar B_0 m, \quad m = -I, (-I+1), \dots, (I-1), I \quad (2.9)$$

The nucleus can change its spin state by absorbing energy equal to the energy difference ΔE of the initial and final states:

$$\hbar \omega = \Delta E \quad (2.10)$$

This change can only happen if the interaction causing it contains a non-zero matrix element connecting the initial and final states. Experimentally, this is achieved by applying a (weak) oscillating magnetic field $\mathbf{B}_1(t) = B_1 \cos(\omega t) \hat{x}$ perpendicular to the static field $B_0 \hat{z}$. The Hamiltonian governing this perturbation is:

$$\hat{H}_{pert} = -\gamma \hbar B_1 \cos(\omega t) \hat{I}_x \quad (2.11)$$

The matrix element of this Hamiltonian connecting states m and m' is:

$$\langle m' | \hat{H}_{pert} | m \rangle \propto \langle m' | \hat{I}_x | m \rangle \quad (2.12)$$

which is non-zero only if $m' = m \pm 1$.

This defines the amount of energy ΔE that should be given to the nucleus to change its state, as well as the corresponding resonance frequency ω_0 of the oscillating B_1 field given by Eq. 2.11:

$$\begin{aligned} \hbar\omega_0 &= \Delta E = \gamma\hbar B_0 \Leftrightarrow \\ \Leftrightarrow \omega_0 &= \gamma B_0 \end{aligned} \quad (2.13)$$

After the spin-probes stop in the sample, they interact with the net magnetic field \mathbf{B}_{net} at their stopping position, given by:

$$\mathbf{B}_{net} = \mathbf{B}_0 + \mathbf{B}_{int} \quad (2.14)$$

where \mathbf{B}_0 is the (static) external field and \mathbf{B}_{int} is the internal magnetic field due to the surrounding material at the implantation site of the nuclear probe.

Thus, their resonance frequency of absorption will differ from Eq. 2.13 and will be instead:

$$\omega_L = \gamma B_{net} \quad (2.15)$$

where ω_L is the Larmor resonance frequency of the nuclear spins in their crystal environment.

In β -NMR, the net magnetic field is extracted by sweeping the frequency ω of \mathbf{B}_1 . When it coincides with the Larmor frequency of the nuclear spin-probes under the influence of \mathbf{B}_{net} , the nuclear spins will start to precess around \mathbf{B}_{net} (in the rotating reference frame) and thus the polarization present will be diminished. In Sec. 2.4.1 the details of extracting \mathbf{B}_{int} using this effect will be presented.

2.3.2 Electric Quadrupolar Interactions

The nucleus of each isotope consists of Z protons and $N=A-Z$ neutrons, where Z is the atomic and A the mass number uniquely defining the isotope. Because of the fact that the nucleus is not a point-like object, but rather a complicated system of its constituent nucleons, the nuclear structure can be understood – from an electromagnetic point of view – as a series of electric and magnetic multipoles, that depend on the spin of the nucleus.

For the simple case of $I=1/2$ the nucleus can be thought as an electric monopole and a magnetic dipole (i.e., it has charge $+Z$ and magnetic moment μ), but for $I>1/2$, there is also a non-zero electric quadrupole moment eQ , due to the fact that the distribution of charge for high-spin nuclei is non-spherical. As a result, nuclei with spin $I \geq 1$ will interact with an electric field gradient (EFG) present at the nuclear position.

The EFG is defined by a matrix, the EFG tensor, with each of its elements calculated by:

$$V_{ij} = \frac{\partial^2 V}{\partial x_i \partial x_j} \quad (2.16)$$

where V is the electromagnetic potential at the site of the probe nucleus, measured in Volts. V_{ij} is measured in V/m^2 .

This general tensor can be diagonalized by rotating the frame to the so-called principal axis system (PAS). In this frame of reference, the EFG tensor has only three non-zero elements across its diagonal, namely V_{xx} , V_{yy} and V_{zz} with $\det(V) = 0$. These three axes are selected so that $|V_{yy}| \leq |V_{xx}| \leq |V_{zz}|$. V_{zz} is then called the principal component of the EFG tensor.

In the PAS frame, the Hamiltonian describing the interaction of the electric quadrupole moment of the nucleus with the applied EFG is given by:

$$\hat{H}_q = \frac{3eQV_{zz}}{4I(2I-1)\hbar} [I_z^2 - \frac{1}{3}I(I+1) + \frac{\eta}{3}(I_x^2 - I_y^2)] \quad (2.17)$$

where I is the spin of the nucleus and η is the asymmetry parameter of the EFG. η takes values between 0 and 1 and is zero in the case of axial symmetry. It is defined by the diagonal terms of the EFG tensor by Eq. (2.18).

$$\eta = \frac{V_{xx} - V_{yy}}{V_{zz}} \quad (2.18)$$

In the case of the spin-2 ^8Li , Hamiltonian (2.17) reduces to:

$$\hat{H}_q^{I=2} = h\nu_q [I_z^2 - 2] + \eta\nu_q [I_x^2 - I_y^2] \quad (2.19)$$

where ν_q is the quadrupole (transition) frequency given by:

$$\nu_q = \frac{e^2 Qq}{8h} = \frac{eV_{zz}Q}{8h} \quad (2.20)$$

where $eQ=V_{zz}$ is the principal component of the EFG tensor. Even at zero magnetic field, the nuclear spin sub-levels $|m\rangle$ are split due to H_q . For spin-2, there are two resonant frequencies, one at $\nu = \nu_q$ stemming from the $|\pm 1\rangle \rightarrow |0\rangle$ transition and one at $\nu = 3\nu_q$ corresponding to the $|\pm 2\rangle \rightarrow |\pm 1\rangle$ transition (see Fig. 2.12).

The position of the resonant frequencies in a given crystal environment can be studied with the β -detected nuclear quadrupole resonance (β -NQR) technique with zero applied field ($B_0 = 0$). A β -NQR resonance spectrum (see Sec. 2.4.1) would

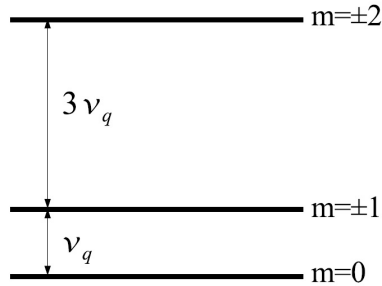


Figure 2.12: The energy splitting of the magnetic sub-levels of ${}^8\text{Li}$, due to the axial part of Hamiltonian (2.19). Adapted from Ref. [106].

reveal 2I satellite resonances due to the single quantum transitions ($\Delta m = \pm 1$) and 2I-1 resonances due to the double quantum transitions ($\Delta m = \pm 2$).

A change in the strength of the EFG would shift the resonant frequencies of the β -NQR spectrum, whereas a departure from axial symmetry (i.e., $\eta > 0$) would introduce a mixing of the $|\pm 2\rangle$ states with a relevant frequency splitting $\Delta_{\pm 2} \sim 3\eta^2\nu_q$. Thus, β -NQR can in principle be used to study any structural phase transitions in a material.

2.4 Types of Measurements

Regardless of the chosen spin-probe (e.g., ${}^8\text{Li}$, ${}^9\text{Li}$, ${}^{31}\text{Mg}$), or the spectrometer used for a specific β -NMR or β -NQR study, there are two basic types of measurements that can be employed for the study of the local properties of crystals with the β -NMR technique: Either the frequency of the transverse RF field is scanned to reveal the resonance(s) of the nuclear probes in their crystal environment using (usually) a continuous ion beam, or the time evolution of the β -decay asymmetry is registered in the absence of a RF field while using a pulsed ion beam. The former type is generally referred to as a “frequency scan”, whereas the latter is known as a “SLR run”.

If a typical ion beam rate of $10^6 {}^8\text{Li}^+/\text{s}$ is assumed, both types of measurements would require 15 min to 40 min for acquiring a run with reasonable statistical uncertainties. For other isotopes this time can be much longer (see Chap. 3).

2.4.1 Resonance Spectra

Before discussing fluctuations and spin relaxation it is important to note that the quasi-static (or time-averaged) parameters of the spin Hamiltonian (e.g., local

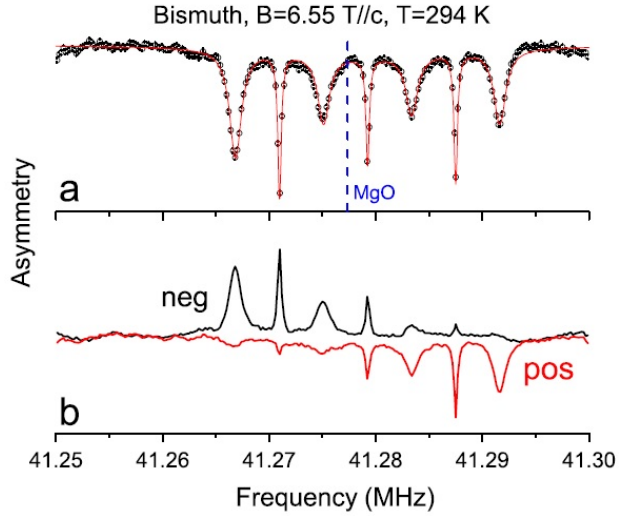


Figure 2.13: (a) Combined resonance spectrum for ^8Li in a Bismuth single crystal at 294 K with four single quantum transitions (SQT) at $\nu = \pm\nu_q$ and $\pm 3\nu_q$, interlaced by three sharper double quantum transitions (DQT). Due to the high degree of nuclear polarization, most ^8Li probes start at the $|m = \pm 2\rangle$ state and thus the “outer” resonances corresponding to the $|\pm 2\rangle \rightarrow |\pm 1\rangle$ transition (e.g., the ones at $\nu = \pm 3\nu_q$ for the SQT) have a larger amplitude than the inner ones, reflecting the larger probe population of the state. (b) The same spectrum, but helicity-resolved. The fact that the position of the resonances is reversed for the two helicities indicates that the resonances are quadrupolar, as the sign of the frequency ν of each resonance (compared to the Larmor frequency) depends only on the nuclear spin state which is reversed for the opposite helicity. Thus the spectra of the two helicities are reflections of each other from the Larmor frequency. Adapted from Ref. [22].

magnetic field or electric field gradient) are directly obtained from the β -NMR resonance spectra. Such spectra may be observed by implanting a continuous beam of highly polarized probe nuclei in the sample in the presence of a static external magnetic field B_0 applied along \hat{z} . One then monitors the lifetime averaged detector asymmetry:

$$\langle A(\omega) \rangle = \int_0^\infty \exp(-t/\tau) A p_z(\omega, t) dt \quad (2.21)$$

as a function of the frequency (ω) of the smaller RF magnetic field $B_1 \cos(\omega t)$ oriented perpendicular to B_0 and the initial polarization direction \hat{z} . In contrast to classical NMR, the external field B_0 is not used to create the nuclear polarization,

but rather simply to hold the polarization and control the resonance frequency.

The RF frequency $\nu = \omega/2\pi$ is varied in steps $d\nu$ in a range around the expected resonance frequency. Every frequency step lasts typically for at least one nuclear lifetime (e.g., at least for a second for ${}^8\text{Li}$), in order to avoid the spin-probe's memory effect, namely having at a given time in the sample probes from the previous frequency steps still present. That would create an unwanted mixing between the measurements of different frequencies. The actual lingering time at each frequency bin is selected by balancing the trade off between the need to minimize the aforementioned memory effect and the time investment required for the acquisition of a resonance spectrum.

A reduction in the time integrated asymmetry $\langle A(\omega) \rangle$ occurs when the frequency of B_1 matches the Larmor resonance frequency (Eq. (2.15)) just like in continuous wave (CW) NMR. This reduction is caused by the resonant precession of the nuclear spins around \mathbf{B}_1 (in the rotating reference frame), which results into depolarization of the spins.

Once a frequency scan is complete, the helicity of the laser is reversed and the frequency scan is repeated with the opposite spin polarization (see Fig. 2.14). The asymmetries of the two helicities will have opposite signs and the combined asymmetry spectrum can be obtained by averaging the absolute values of them:

$$\bar{A} = \frac{A^+ - A^-}{2} \quad (2.22)$$

where \bar{A} is the combined asymmetry and A^\pm is the asymmetry for each laser helicity.

This process removes many sources of systematic error associated with the β -NMR measurement. For instance, in the geometry of the β -NQR spectrometer, any source of β -scattering between the sample and the L/R detectors that is asymmetric between the two detectors will shift the asymmetries of both helicities by a constant, frequency-independent value, but the combined asymmetry will be completely unaffected by such an effect, as the constant would cancel out.

A resonance measurement consists typically of several ($\sim 2-20$) scans for each helicity, in order to minimize the statistical uncertainties. If any given frequency scan is identified as problematic (e.g., due to a proton trip or problems with the laser), it can be individually disregarded before averaging all scans into a single resonance spectrum.

The resonance shift compared to that of a reference material allows for the study of the local internal magnetic field \mathbf{B}_{int} . In β -NMR, the most commonly used reference material is MgO, which is a non-magnetic insulator with very few nuclear moments and also $\nu_q = 0$, thus the ${}^8\text{Li}$ β -NMR resonance is very narrow and more or less unshifted except for a small chemical shift. Therefore, for MgO it holds

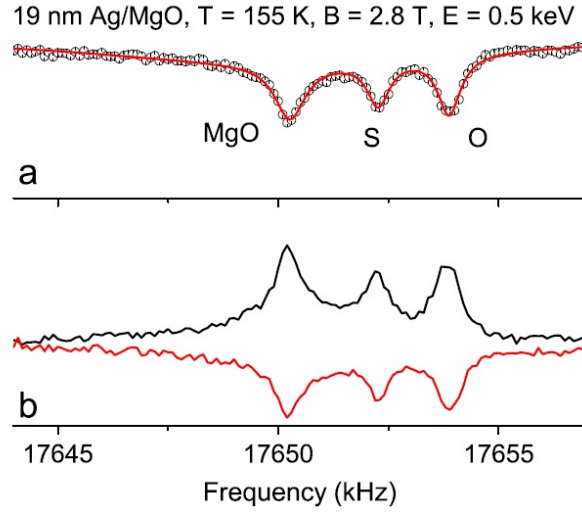


Figure 2.14: (a) Combined resonance spectrum for ^8Li implanted in a epitaxial Ag film (19 nm) grown on MgO at 155 K. There is one resonance from MgO and two from the thin Ag film. The resonance labeled O is attributed to ^8Li in the octahedral interstitial site in Ag, whereas the resonance labeled S is due to ^8Li in the substitutional site in Ag. All these sites have cubic symmetry and therefore show no quadrupolar splitting. (b) The same spectrum, but helicity-resolved. The position of the spectra is the same for both helicities, which indicates that they are not due to quadrupolar effects. Adapted from Ref. [22].

approximately that $\nu_{\text{MgO}} \sim \gamma B_0$. As a result, the resonance shift $\Delta\nu$ of a material relative to MgO yields:

$$\Delta\nu = \nu - \nu_{\text{MgO}} = \gamma B_{\text{net}} - \gamma B_0 = \gamma B_{\text{int}} \quad (2.23)$$

where Eq. (2.14) is used to get the last equality.

The position of the resonance(s) is determined by the quasi-static or time averaged parameters of the spin Hamiltonian. Nevertheless, as in conventional NMR, the shape of the β -NMR resonance may still be sensitive to the fluctuations in the local environment. For example in the fast fluctuation limit the line width is narrowed and varies as $\Delta^2 \tau_c$ where Δ is the static line width and τ_c is correlation time for fluctuations in spin Hamiltonian terms responsible for the line narrowing.

Coupling between the nuclear quadrupole moment and any local electric field gradient will lead to additional structure (e.g., quadrupolar splittings, see Sec. 2.3.2), as in conventional NMR. By gradually varying the frequency of the RF field, a

spectrum of all the resonances of the system can be generated.

The power of the RF field is what destroys the nuclear polarization, so its value can affect (in a well-defined way) the resonance spectrum. If the RF power is small, it won't be enough to depolarize all spin-probes at resonance, so the asymmetry peak will have a small amplitude and will be hard to resolve. This effect suppresses the β -NMR signal, so it would make a resonance measurement more time consuming. On the other hand, a strong RF would depolarize the probes on resonance completely, but it would also partially destroy the polarization of probes being slightly off-resonance. This effect artificially broadens the resonance and is generally referred to as "power broadening". Due to these effects, sometimes it is necessary to measure the same resonance using different RF powers, in order to be able to distinguish the underlying resonance width from the power broadening.

2.4.2 Spin Lattice Relaxation Spectra

Information on the fluctuations of the electromagnetic fields in a material of interest is obtained through measurements of the (longitudinal) spin-lattice relaxation (SLR) rate in the absence of a RF magnetic field. Note that this type of measurement does not provide any spectral resolution of the fluctuations driving the SLR.

The SLR may be studied by implanting a series of beam pulses into the sample and then monitoring $\mathcal{A}(t)$, which is the convolution of the asymmetry $A(t-t')$ with the beam pulse $N(t')$ where t' is the time of arrival for a given probe and $t-t'$ is the time spent in the sample before its β -decay:

$$\mathcal{A}(t) = \int_{-\infty}^t N(t')A(t-t')dt' \quad (2.24)$$

In general the SLR rate, usually denoted as $1/T_1$ (with T_1 being the longitudinal spin-lattice relaxation time), originates from fluctuations in the local magnetic field (and the EFG for nuclei with $I \geq 1$) occurring in a direction perpendicular to the nuclear polarization axis. They can be arising from fundamental processes such as phonon scattering, magnon scattering, conduction electron scattering, diffusion, etc.

The measured SLR relaxation rate depends mostly on those fluctuations that have an appreciable spectral density close to the Larmor frequency. Since ν_L is related to the total magnetic field (see Eq (2.15)), the SLR relaxation rate depends on the applied magnetic field B_0 , so the latter can be varied to allow for the study of fluctuations of different frequencies.

In the case that the SLR is caused by fluctuating magnetic dipolar interactions, the $1/T_1$ is often approximated using the Bloembergen-Purcell-Pound (BPP) theory. The ansatz of BPP is that the fluctuations driving the relaxation are described by a

autocorrelation function which is proportional to $\exp[-t/\tau_c]$, where τ_c is the correlation time. The Fourier transform of the autocorrelation function is a Lorentzian describing the spectral density of the fluctuation. The observed relaxation rate is proportional to the magnitude of the spectral density at the Larmor frequency. In the case of the magnetic dipole interaction driving the SLR, $1/T_1$ is given by:

$$\frac{1}{T_1} = K \frac{\tau_c}{1 + \omega_0^2 \tau_c^2} \quad (2.25)$$

where K is a constant depending on the nuclear probe and the dipole-dipole separation distance.

In the simplest case of all nuclear probes being at equivalent environments with a well defined $1/T_1$ rate, the SLR rate can be extracted by fitting the SLR spectrum using a single exponential:

$$A(t-t') = \exp[-(t-t')/T_1], \quad (2.26)$$

Substituting this into Eq. (2.24) and assuming a square beam pulse during the time interval $[0, \Delta]$, one obtains a form for the asymmetry during and after the pulse, by averaging over all arrival times:

$$\mathcal{A}(t) = \begin{cases} A_0 \frac{\tau'}{\tau_\beta} \frac{1 - \exp(-t/\tau')}{1 - \exp(-t/\tau_\beta)} & t \leq \Delta \\ A(\Delta) \exp[-(t-\Delta)/T_1] & t > \Delta \end{cases}, \quad (2.27)$$

where τ_β is the radioactive lifetime, $1/\tau' = 1/\tau_\beta + 1/T_1$ and A_0 is the initial asymmetry at the time of implantation. Note that the SLR spectrum has two distinct regions (see Fig. 2.15): during the beam pulse ($0 < t < \Delta$) the asymmetry relaxes towards a dynamic equilibrium value [107]:

$$\bar{\mathcal{A}} = \frac{A_0}{1 + \tau_\beta/T_1}, \quad (2.28)$$

Note that this equilibrium value is the ‘‘baseline’’ (i.e., off-resonance) asymmetry of the resonance spectrum (see Sec. 2.4.1). After the beam pulse ($t > \Delta$) $\mathcal{A}(t)$ decays towards the Boltzmann equilibrium value, which is essentially zero on our scale. There is a pronounced kink in $\mathcal{A}(t)$ at $t = \Delta$ when the beam pulse ends. This is also the time with the highest event rate and smallest statistical uncertainty in $\mathcal{A}(t)$. The statistical uncertainties of β -NMR measurements are governed by Poisson statistics, so the relative uncertainty of a measurement decreases by the square root of the number of counts. Because of the radioactive decay law (see Eq. (2.29)), the number of decay events are maximum when the largest number of radionuclides are present in the sample, which is exactly at time $t = \Delta$.

$$\frac{dN(t)}{dt} = N(t)\exp(-t/\tau_\beta), \quad (2.29)$$

where $N(t)$ is the number of nuclides present in the sample at time t .

The beam-on time Δ is set to several nuclear lifetimes (typically $\Delta \sim 4\tau_\beta$) and the beam-off region should be adequate for all nuclear probes to decay before another beam pulse arrives ($\sim 10\tau_\beta$). After the end of the measuring period described above, the laser helicity is reverted and another beam pulse is implanted, having the opposite nuclear polarization. As in the case of a frequency scan (see Sec. 2.4.1), the SLR spectra of the two helicities can be combined using Eq. (2.22) to generate the combined SLR histogram.

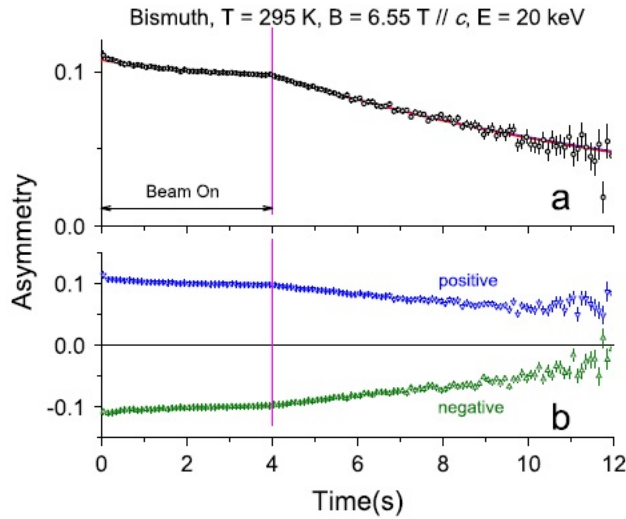


Figure 2.15: SLR spectrum of ^8Li implanted in a single crystal of bismuth at 295 K. The combined asymmetry is shown in (a). In (b), the helicity-resolved SLR spectra are shown. Adapted from Ref. [22].

2.5 Enhancing the capabilities of β -NMR using α detection

According to Eq. (2.3), each ^8Li decay leads to the production of a β - and two α -particles (plus an electron antineutrino). So far, ^8Li β -NMR has ignored completely the subsequent α -decay of ^8Be and any information that it could be carrying. One

aim of this thesis is to couple the information from the α - and β -particles in order to expand the capabilities of β -NMR.

As mentioned in Sect. 2.1, ^8Li has a non-zero electric quadrupole moment. This makes it possible to study with the same probe both magnetic and electric quadrupolar phenomena (see Sect. 2.3.1 and Sect. 2.3.2). On the other hand, in certain instances it might be hard to identify the relative contributions of these underlying interactions to the spin lattice relaxation rate.

As part of this thesis, we showed that it is possible to resolve the primary source of relaxation in a material, by performing an isotopic comparison using two different β -decaying isotopes of the same element (in this case ^8Li and ^9Li). The different nuclear characteristics of the two isotopes (spin, electric quadrupole moment) result in different SLR rates for the two isotopes in the limits of either *purely* magnetic or electric quadrupolar interactions (see Ch. 3).

A major limitation when using the isotopic comparison of $^9\text{Li}/^8\text{Li}$ is that the signal from ^9Li is heavily suppressed, i.e., ^9Li has a smaller effective β -decay asymmetry. Indeed, we would typically spend many hours acquiring a single ^9Li SLR spectrum, compared to 15-20 min for ^8Li , and still our uncertainties were dominated by the ^9Li measurements. Even though we don't need to compare the $1/T_1$ rates for ^9Li and ^8Li for every condition, but only for a few temperatures and fields, it would still be advantageous to enhance the ^9Li signal.

The reason for the lower ^9Li asymmetry is that ^9Li can β -decay into three different energy levels of ^9Be , two of which have opposite asymmetries that nearly cancel when weighted by their branching probabilities. Nevertheless, two of the three main decay channels of ^9Li further decay into two α -particles, which makes it possible to differentiate between the different channels by tagging the β -particles in coincidence or in anti-coincidence with an α . In this thesis we designed a system that allows for the aforementioned α -tagging (see Sect. 3.3.2). The effective asymmetry of an α -tagged measurement was found to be 3 times larger than that without α -detection.

Thus, we showed that by coupling the signal of the β and α -decays of ^9Li , we can amend considerably the limitations of using the isotopic comparison method in ^8Li β -NMR, establishing it as a new tool for β -NMR.

In addition, being able to detect the α -particles coming from the decay of ^8Li allows us to measure the rate with which lithium ions diffuse inside materials. To measure lithium diffusion, a short beam pulse of ^8Li ions gets implanted in the sample material. The energy of the beam defines the initial depth profile of the ions. Upon implantation, the lithium ions start diffusing through the sample and decay at random times (following the decay rate of ^8Li) to ^8Be and then immediately into two α -particles. The α -particles attenuate inside the material very fast, so the highest energy α -particles can come only from decays close to the surface.

In order to establish the feasibility of this technique and identify the optimum detection geometry a detailed Monte Carlo simulation of the geometry and physics of the experiment using the Geant4 simulation package was carried out. Geant4 was developed at CERN, and it is a very powerful and flexible toolset for particle-material interactions (see Ch. 5).

Based on the aforementioned simulations, we designed a new cryostat that is suitable for this study (see Appendix A). The new cryostat has a nominal temperature range of 5 K to 400 K (compared to 3.5 K to 300 K of the old β -NQR cryostat), thus is really a cryo-oven (which is of course an oxymoron). Being able to reach higher temperatures can be critical for studying slow diffusion in materials where the diffusion is too slow at room temperature, since the diffusion rate increases exponentially with temperature in materials that follow Arrhenius law.

Following the commission of this new spectrometer, we conducted proof of principle experiments on rutile TiO_2 (see Ch. 6), where we were able to directly measure the diffusion rate of lithium at a nanometer scale over a wide temperature range. With this measurement we showed that the temperature dependence of the diffusion is bi-Arrhenius, with a second, previously unknown Arrhenius component below ~ 200 K and also proved that Li^+ gets trapped upon reaching the (001)-surface of rutile, which explains the reported suppressed Li intercalation in this material.

In the remaining chapters of this thesis, these two applications of the α -detection system coupled to ^8Li β -NMR will be presented.

Chapter 3

Using α -tagged ${}^9\text{Li}$ β -NMR to Distinguish the Source of Spin Lattice Relaxation in ${}^8\text{Li}$ β -NMR

As ${}^8\text{Li}$ has a non-zero electric quadrupolar moment, a key issue in any ${}^8\text{Li}$ β -NMR experiment is to identify the source of spin-lattice relaxation (SLR) and in particular whether the fluctuations driving the SLR are magnetic or electric in origin. Unlike the positive muon, μ^+ ($I = 1/2$), ${}^8\text{Li}$ ($I = 2$) is *not* a pure magnetic probe and its relaxation is sensitive to both fluctuating magnetic fields and electric field gradients (EFG's).

In some cases, the primary source of relaxation may be inferred. For example, in simple metals the observed relaxation is linear in temperature [107] as expected from the Korringa relaxation [108], which originates from the scattering of the spin of the conduction electrons at the Fermi surface from the nuclear spin, mediated through the (magnetic) contact hyperfine interaction.

However, in more complicated instances, such as heterostructures comprised of magnetic and non-magnetic layers, it becomes difficult to determine the contribution of each type of relaxation. $\text{LaAlO}_3/\text{SrTiO}_3$ multilayers are particularly illustrative of this point; the bulk layers are non-magnetic insulators, while there is evidence of magnetism at their interfaces [20].

In conventional NMR it is possible to differentiate between relaxation mechanisms by isotopic variation of the nuclear probe (if suitable isotopes exist), since the absolute relaxation rates for each isotope scale according to their nuclear moments. For two isotopes with significantly different nuclear moments (e.g., ${}^6\text{Li}$ and ${}^7\text{Li}$ [109]) the ratio of the relaxation rates should be distinctly different in the limits of either pure magnetic or pure electric quadrupolar relaxation. Here we test the feasibility of isotope comparison applied to β -NMR — using ${}^8\text{Li}$ and ${}^9\text{Li}$, two β -radioactive isotopes.

The stopping sites of ${}^8\text{Li}$ and ${}^9\text{Li}$ are often interstitial rather than substitutional as in the case of conventional NMR. However, we expect that both implanted ${}^8\text{Li}$ and ${}^9\text{Li}$ will probe the same sites. Measurements on ${}^9\text{Li}$ are more time consuming

than for ${}^8\text{Li}$. This is related to the fact that ${}^9\text{Li}$ lies one neutron further away from the valley of stability, consequently the beam intensity in this experiment was about 10 times lower and ${}^9\text{Li}$ has a more complicated β -decay scheme, which results in a β -decay asymmetry about 3 times smaller than for ${}^8\text{Li}$, as will be discussed below.

Measurements reported here were made in Pt metal, where the spin relaxation rate of ${}^8\text{Li}$ (${}^9\text{Li}$) is dominated by Korringa scattering [110], which is magnetic, and in strontium titanate (SrTiO_3), which is a non-magnetic insulator with a large static electric quadrupolar interaction for implanted ${}^8\text{Li}$. SrTiO_3 is a common substrate material but also has interesting properties on its own which have been studied extensively with a wide variety of methods including β -NMR. Although we expect the quadrupolar fluctuations in EFG caused by lattice vibrations to dominate the spin relaxation, there are also potential magnetic sources of relaxation that could contribute as explained below.

In the following sections we first summarize the theoretical considerations behind the isotopic variation method. This is then followed by the experimental results along with a discussion.

3.1 Isotopic Comparison Method

The magnitudes of each contribution to the spin-lattice relaxation rate (SLR) for a given probe nucleus scale according to their nuclear properties; namely, their spin, I , magnetic moment, μ , and electric quadrupole moment, Q . Measurements of SLR rates for two different isotopes under identical experimental conditions (i.e., magnetic field, temperature, etc.) can be compared through their ratio, R :

$$R(I, I') \equiv \frac{1/T_1(I)}{1/T_1(I')} = \frac{1/T_1^{\text{M}}(I) + 1/T_1^{\text{Q}}(I)}{1/T_1^{\text{M}}(I') + 1/T_1^{\text{Q}}(I')}, \quad (3.1)$$

where I and I' denote the spin quantum number of each isotope and $1/T_1^{\text{M}}(I)$, $1/T_1^{\text{Q}}(I)$ are the SLR rates due to magnetic and electric quadrupolar interactions, respectively.

Two limits are of interest here: when the relaxation is *solely* due to either magnetic or quadrupolar interactions within the host-sample.

In the former case, Eq. (3.1) reduces to the ratio of pure magnetic relaxation, R_{M} , which in the limit of fast fluctuations (i.e., $\tau_c^{-1} \gg \omega_0$, where τ_c is the NMR correlation time and ω_0 is the Larmor resonance frequency, see Sect. 2.3.1) is:

$$R_{\text{M}}(I, I') = \left(\frac{\mu/I}{\mu'/I'} \right)^2 = \left(\frac{\gamma}{\gamma'} \right)^2, \quad (3.2)$$

where μ and γ are the magnetic moment and gyromagnetic ratio of each isotope. Note that the fast fluctuation limit ensures that $1/T_1$ is independent of ω_0 , which simplifies the ratio considerably.

In the other case, Eq. (3.1) yields the ratio of relaxation rates in the pure quadrupolar limit, R_Q :

$$R_Q(I, I') = \frac{f(I)}{f(I')} \left(\frac{Q}{Q'} \right)^2, \quad (3.3)$$

where Q are the nuclear quadrupole moments, and [111]

$$f(I) = \frac{2I+3}{I^2(2I-1)} \quad (3.4)$$

Thus, given the nuclear moments of each isotope, one can calculate the ratio of relaxation rates when either mechanism is dominant. Using Eqs. (3.2) and (3.3), along with the nuclear spins and moments for ^8Li and ^9Li (see Table 2.1), we find the limiting cases for $T_1^{-1}(^9\text{Li})/T_1^{-1}(^8\text{Li})$: 7.679 64(16) and 2.1362(4) for R_M and R_Q , respectively.

The difference between these limits is not as pronounced as for ^6Li and ^7Li [109], where R_M and R_Q differ by a factor of ~ 90 [112]. Nevertheless, ^8Li and ^9Li are sufficiently different that the nature of fluctuations and resulting spin relaxation (magnetic versus electric quadrupolar) may be differentiated by such a comparison.

3.2 Experimental Demonstration of the Isotopic Comparison Method

To demonstrate the comparison of ^8Li and ^9Li in β -NMR, two very different materials were selected.

The first is Pt which is a d-band metal with a face cubic centered (fcc) crystal structure in which the ^8Li resides at a site with little or no quadrupolar interaction (i.e., the octahedral interstitial site, at which the EFG is zero by symmetry). In this test case we expect the relaxation to be predominantly magnetic, as $1/T_1$ is known to depend linearly on temperature [107], as expected from Korringa scattering.

SrTiO_3 on the other hand is a non-magnetic paraelectric – on the verge of being ferroelectric [113] – insulator with few nuclear moments and no conduction electrons (so no Korringa relaxation). Previous work in SrTiO_3 shows that ^8Li experiences a large quasi-static quadrupolar interaction [25]. Thus in this case, we expect quadrupole fluctuations to play a more important role. Nevertheless, it is still unclear to what extent magnetic relaxation can be neglected in SrTiO_3 , as there could be defect-related magnetic effects present.

For example, O vacancies in SrTiO₃ result in two Ti³⁺ ions which are typically paramagnetic. In principle, the resulting paramagnetic defects would have low frequency magnetic fluctuations which will contribute to the SLR of the implanted Li nucleus in SrTiO₃, as dilute paramagnetic effects are well known to affect the $1/T_1$ in both solids and liquids.

3.2.1 Platinum

The sample was a high-purity (99.999%) Pt foil with dimensions 12x12 mm² and thickness of 0.1 mm. It was cut from the same initial foil that was studied with β -NMR by *Ofer et al.* [110]. The implantation energy was 18 keV, which corresponds to a range of 42 nm and a straggle of 23 nm for both isotopes of lithium. The implantation profile was estimated using the Monte-Carlo-based SRIM-2013 software [104].

The resonance spectra (see Sect. 2.4.1) at 1.90 T and 300 K for both ⁸Li and ⁹Li can be seen in Fig. 3.1. To account for power broadening, the spectra were fit to a Voigt line shape [101] *simultaneously*, sharing a common (normalized) resonance frequency and Gaussian width.

For ⁸Li, the intrinsic Gaussian FWHM was found to be 0.85(10) kHz. This value is somewhat smaller than those reported previously in Pt [114], where power broadening was not taken into account. By comparing the ⁸Li resonance in Pt with that in the standard β -NMR reference material MgO [115], the Knight shift is estimated as -309.8 ± 1.9 ppm, in agreement with previous measurements. For ⁹Li in Pt at 1.90 T and 300 K, a single resonance at 33.18685 ± 0.00028 MHz with FWHM of 6.8 ± 0.6 kHz is observed.

The fact that ⁸Li and ⁹Li resonance measurements in Pt exhibit a single narrow line below 300 K, indicates that both isotopes occupy a single site with a vanishing (static) EFG [101, 114]. The spectrum is simpler than in other metals, where multiple Li⁺ sites are found below 300 K [23, 24, 116–120].

Given the simplicity of the spectrum, we expect SLR in Pt to follow a single exponential form (see Eq. 2.27).

The SLR rates for ⁸Li⁺ and ⁹Li⁺ implanted at 300 K were measured in magnetic fields of 1.90 T and 6.55 T — the latter shown in Fig. 3.2. For both isotopes the length of the beam pulse ($\sim 3.3\tau_\beta$) and the total observation time ($\sim 9.9\tau_\beta$) were chosen to minimize the statistical uncertainties.

Temperature dependent SLR of ⁸Li⁺ in Pt has been studied previously by *Ofer et al.* [110] between 3 K to 295 K at 4.10 T, where the SLR rate was found to increase linearly with temperature, implying Korringa relaxation [108]. This relation holds for high magnetic fields and different implantation energies.

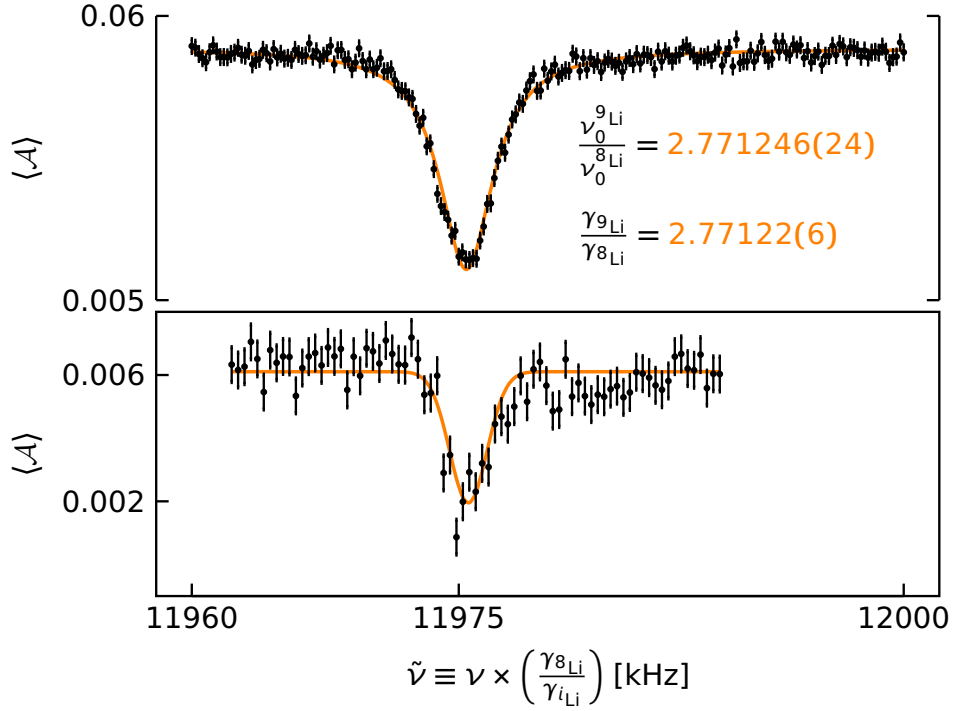


Figure 3.1: Resonance spectra in Pt foil at 300 K and 1.90 T with ^8Li (*top*) and ^9Li (*bottom*). The frequency has been normalized to the gyromagnetic ratio of each isotope.

The temperature-dependent $^8\text{Li}^+$ SLR rates at various magnetic fields are shown in Fig. 3.3, including our measurements, as well as results from *Ofer et al.* [110].

The ^8Li SLR rate at 6.55 T is in good agreement with the Korringa fit by *Ofer et al.* [110], extrapolated to 300 K, whereas the measured SLR rate at 1.9 T is lower by about 10%. It is unlikely that this is a real effect since any additional source of relaxation would *increase* the relaxation at the lower magnetic field which is opposite to what is observed. The slight reduction in $1/T_1$ measured at 1.9 T suggests there may be a small systematic error related to the fact that the beam spot is a bit larger at that magnetic field (thus there could be a small non-relaxing background signal from $^8\text{Li}^+$ stopping outside the sample) and the ratio between the β -rates in the two detectors is different compared to the higher field. However, it should be noted that the measured ^8Li SLR rates in Pt foil appear to increase linearly with temperature, independent of implantation energy and applied magnetic field.

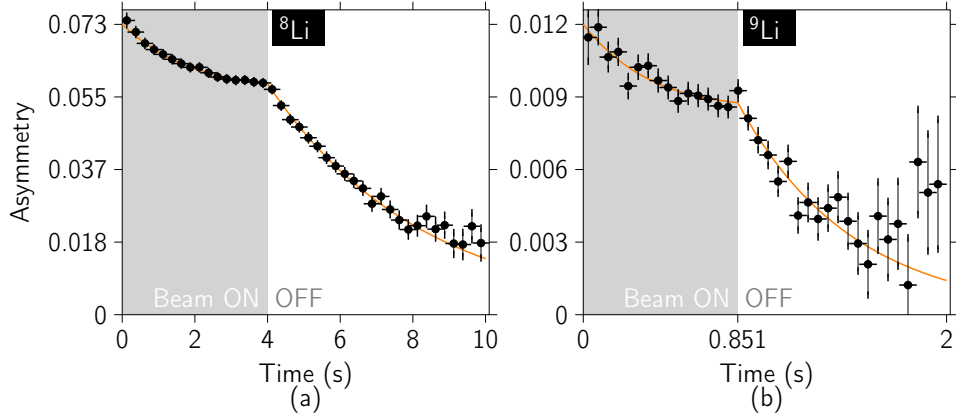


Figure 3.2: SLR spectra for ${}^8\text{Li}^+$ (left) and ${}^9\text{Li}^+$ (right) implanted in Pt foil with an energy of 18 keV at 300 K 6.55 T. The solid orange lines are fits to Eq. (2.27). Note the different time scales, which reflect the lifetime of each radionuclide. The absolute SLR rate for ${}^9\text{Li}^+$ is 1.60(10) and 0.2368(26) for ${}^8\text{Li}^+$.

The ratios of $T_1^{-1}({}^9\text{Li})/T_1^{-1}({}^8\text{Li})$ at 6.55 T and 1.90 T are in good agreement with each other and we find a relaxation rate ratio, R_{Pt} , of 6.8(4) and 5.9(9) at 6.55 T and 1.90 T, respectively.

3.2.2 Strontium Titanate

SrTiO_3 was chosen for this study since it is a non-magnetic insulator, and a material where the ${}^8\text{Li}$ relaxation is expected to be dominated by electric quadrupolar interactions. It has been studied extensively with low-energy ${}^8\text{Li}$ β -NMR [18, 106, 121].

SrTiO_3 is a cubic perovskite at 300 K (Fig. 3.4). Implanted ${}^8\text{Li}$ occupies three equivalent interstitial non-cubic sites [19], namely the face-centered sites in the unit cell centered at Sr^{2+} . At 300 K, the EFG is axially symmetric, with the main axis along $\text{Sr}-{}^8\text{Li}-\text{Sr}$.

Two SrTiO_3 samples were studied in this experiment. Both were $10 \times 8 \times 0.5 \text{ mm}^3$ single crystals with the (100) orientation, i.e., with the a cubic axis perpendicular to the face of the sample. Both samples were epitaxially polished (0.2 nm RMS roughness). Sample 1 (S1) was left bare, while sample 2 (S2) was capped with 30 nm of LaTiO_3 ¹. At the implantation energy of 18 keV, a negligible fraction of ${}^8\text{Li}^+$ ions stop in the LaTiO_3 film, or the near surface region. This was checked for both ${}^8\text{Li}$ and ${}^9\text{Li}$ by using SRIM-2013 [104].

¹Note that the thin layer of LaTiO_3 was for a different experiment, but had no effect on the current experiment, since it was so thin that most of the ${}^8\text{Li}$ passed through it.

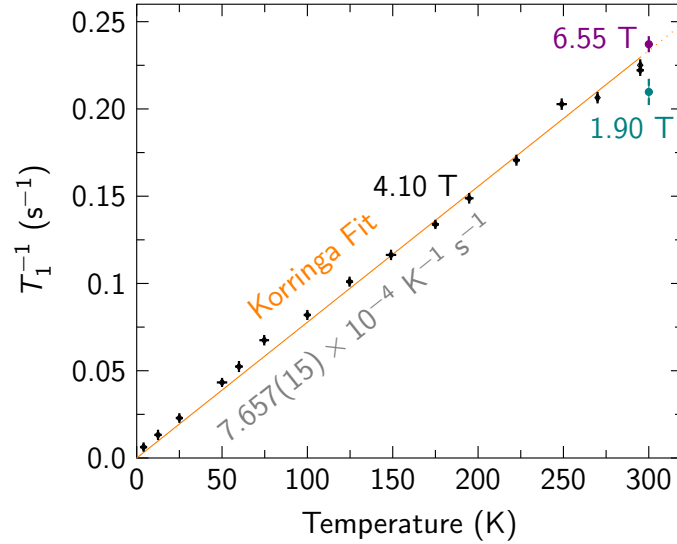


Figure 3.3: Measured SLR rates for ^8Li implanted in Pt. The relaxation rate increases linearly with temperature, appearing insensitive to both implantation energy and magnetic field strength, consistent with a Korringa mechanism [108]. Measurements from this work are highlighted in colored disks, while black diamond markers indicate data from earlier measurements on Pt foil [110]. The solid orange line is Korringa fit to *all* the SLR rates in Pt and differs somewhat from the result of *Ofer et al.* due to the additional data points from this work.

Figure 3.5 shows the SLR spectra for ^8Li and ^9Li at 300 K at various magnetic fields between 0 mT to 15 mT applied along the (100) cubic crystallographic axis of sample S1. It is evident from the data that the relaxation is more complex than in Pt since a single exponential fails to describe the decay of spin polarization.

The spectra were best fitted with a two-component exponential function, but given that one of the relaxation rates is found to be nearly zero, a phenomenological relaxation function of the following form [121] was used:

$$A(t-t') = f \exp[-\lambda(t-t')] + (1-f), \quad (3.5)$$

where f is the fraction of the relaxing asymmetry ($0 \leq f \leq 1$) and $\lambda \equiv 1/T_1$.

Since f is approximately field-independent in our range of fields, the SLR spectra for ^8Li and ^9Li were fit globally, sharing a common f , which turned out to be 0.347(3).

One might expect this since a magnetic field applied along the (100) direction breaks the local symmetry between the 3 otherwise equivalent sites. More specifi-

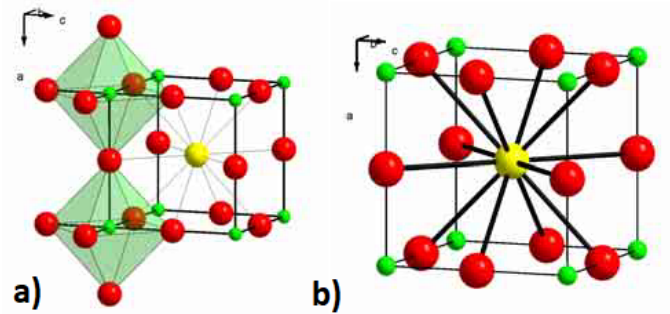


Figure 3.4: The crystal structure of the cubic perovskite SrTiO₃. A Sr²⁺ (yellow sphere) lies at the center of the unit cell, with O²⁻ ions (green spheres) at the corners of the cube and Ti⁴⁺ ions (red spheres) at the octahedral holes created by the oxygens. Implanted ⁸Li⁺ occupies one of the face-centered sites of the unit cell. Adapted from Ref. [122].

cally the EFG tensor is axially symmetric about one of the three orthogonal cubic axes, with only a small asymmetry factor $\eta \sim 0.01$ [123] (see Sect. 2.3.2). Thus the applied magnetic field is either along the EFG axis or perpendicular to it. However f was about the same in zero-field (ZF) and given that the two 90 degree sites don't contribute to the ZF signal and that f is about the same at ZF, the more complex relaxation function observed in SrTiO₃ must be unrelated to the angle between the magnetic field and the symmetry axis of the EFG.

Consequently there must be an additional source of fluctuations affecting the SLR for all 3 sites in the same way but in an inhomogeneous manner either in time or space. Previous studies have found that the relaxing fraction f is also temperature independent [121]. This suggests that the origin of the relaxing component should be structural, associated with defects close to about one third of the implanted Li, with the rest being in a non-relaxing environment away from such centers.

Regarding the relaxation function, note that this is an unfamiliar regime, where the Zeeman interaction is smaller than $\nu_Q = 153.2$ kHz (see Sect. 2.3.2) over the full range of fields, since even for our highest field measurement at 15 mT, $(\gamma/2\pi)B = 94$ kHz. At high fields (several Tesla), previous work suggests that $f = 0$ [25]. In the high-field limit, the relaxation of any β -NMR experiment approaches zero, because the Zeeman splitting becomes larger than the fluctuation rate terms giving rise to relaxation, which in turn converts the relaxing component into a non-relaxing one, leading to $f = 0$. There is likely some change that will happen around 50 mT, where the Zeeman interaction really starts to take over. In addition, the fraction f is expected to be independent of the sample orientation, since SrTiO₃ is a cubic

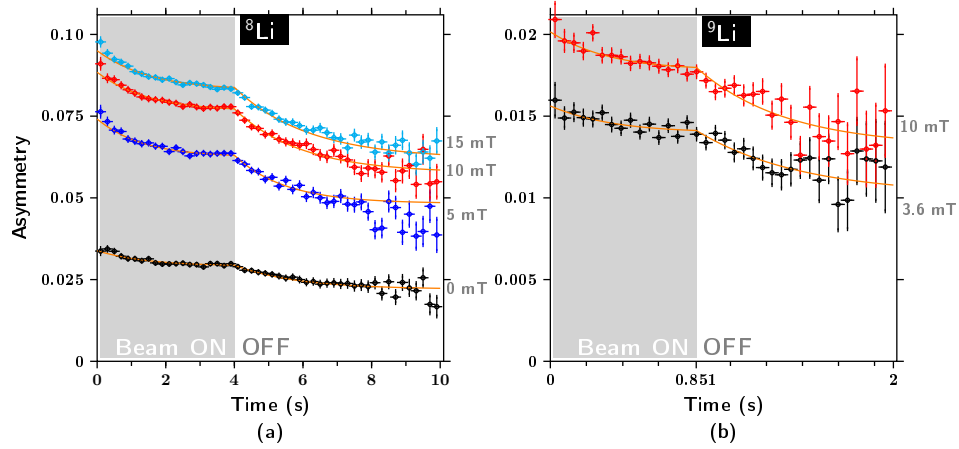


Figure 3.5: SLR spectra of ^8Li (*left*) and ^9Li (*right*) in single crystal SrTiO_3 (sample S1) at 300 K. The solid orange lines are a global fit to Eqs. (2.24) and (3.5) where a common parameter f is shared between all spectra, as it was found to be approximately field-independent in this field range.

material.

In sample S1, the SLR rate for ^8Li is found to vary weakly with applied magnetic field below 15 mT, reaching a plateau below 5 mT (see Fig. 3.6). It is likely, but unclear due to the limited statistics, that a similar behavior occurs for ^9Li . At 300 K, the ratio of the $^9\text{Li}/^8\text{Li}$ SLR rates for SrTiO_3 , R_{STO} , was found to be 3.7(7) at 10 mT and 2.4(5) at 3.6 mT.

For comparison, the SLR rate of ^8Li and ^9Li was also measured in a second SrTiO_3 sample (S2) (see Fig. 3.7).

The fit for sample S2 using Eq. 3.5 does not include a small but very fast relaxing component that can be identified at the early part of Figure 3.7. Given the large statistical uncertainties of the ^9Li spectrum, it would be over-fitting to add an extra fast relaxing component, in addition to the two terms of Eq. 3.5. Moreover, this very fast relaxing component is not present in other studies on SrTiO_3 (including our current measurements for sample S1), which means that this extra fast relaxation is most probably related to lithium stopping outside the sample (e.g. due to beam instabilities or backscattering off the target material). In low magnetic field, having a percentage of the incoming lithium stopping outside the sample often manifests as a small but very fast relaxing component, irrelevant to the material under study.

The ratio of relaxation rates in sample S2 at 10 mT was found to be 2.4(5).

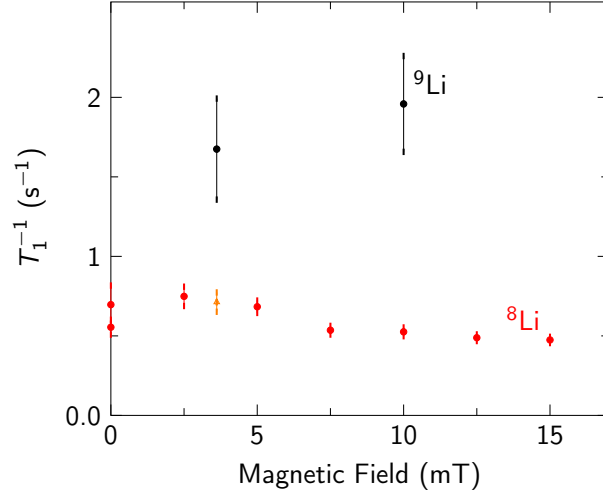


Figure 3.6: Field dependence of $1/T_1$ for ^8Li and ^9Li in SrTiO_3 at 300 K. The (orange) triangle represents a linear interpolation at 3.6 mT from the 2.5 mT and 5 mT ^8Li measurements.

3.2.3 Ratio of Relaxation Rates

The ratio of relaxation rates in platinum $R_{Pt} = 6.82(29)$, which is the weighted average of the measurements at 6.55 T and 1.90 T. Note that this value is somewhat less than expected from the pure magnetic limit R_M (Fig. 3.8).

The reason for this discrepancy could be the non-zero temperature. All measurements were taken at 300 K where the lithium ions could have some quadrupolar contribution due to local vibrations and scattering of phonons which leads to a fluctuating EFG. However $1/T_1$ is very linear in temperature, whereas any such contributions would have a stronger temperature dependence. It would be interesting to repeat the measurements at a lower temperature to check if R_{Pt} is closer to the magnetic limit or not. In any case, an electric quadrupolar contribution to $1/T_1$ cannot be very large in Pt at 300 K.

We also reported a value of R_{STO} in two samples of SrTiO_3 . In the first sample, the weighted average R_{STO} of the measurements at 3.6 mT and 10 mT yielded 2.9(4). This value is close, but not within experimental error of the quadrupolar limit of $R_Q \approx 2.14$. After taking into account the measurement on the second SrTiO_3 sample, which was 2.4(5) at 10 mT, the weighted ratio of relaxation rates in SrTiO_3 is found to be 2.7(3), closer to the quadrupolar limit. Still there is a small disagreement which suggests some small magnetic contribution to $1/T_1$.

This small magnetic relaxation may be related to the observed non-exponential

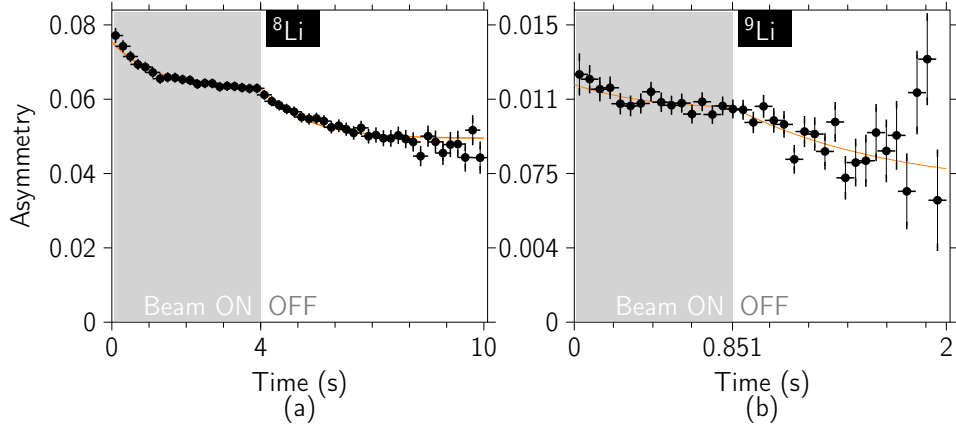


Figure 3.7: SLR spectra of ^8Li (left) and ^9Li (right) in SrTiO_3 (sample S2) at 10 mT and 300 K. The solid orange lines are a global fit to Eqs. (2.24) and (3.5) where a common parameter f is shared between both spectra.

decay of polarization. The relaxing fraction f has been found in previous studies as well and it is approximately temperature independent [121] and independent of the angle between the magnetic field and the crystallographic axis [123]. This suggests that it could be due to the dynamics associated with defects close to some of the implanted Li. These fluctuations would be primarily paraelectric [123], but a small portion could be magnetic in origin. For example any O vacancies a few lattice sites away would give rise to paramagnetic Ti^{3+} ions, in addition to paraelectric fluctuations. A typical level of oxygen vacancies in SrTiO_3 of about 1 – 2% would result in lithium having such a defect for a nearest or next-nearest neighbor 20 – 30% of the time, which could explain the fraction $f \sim 0.3$.

As to whether these defects are primarily intrinsic to the crystal or caused by the beam implantation, note the following: There is no doping taking place with ^8Li , since each ion decays into a β and two α -particles (plus an electron antineutrino). ^9Li , on the other hand, decays into the stable ground state of ^9Be half of the time, so some Be doping should be expected. Based on the total number of implanted $^9\text{Li}^+$, the typical width of the beamspot and the implantation depth simulated by SRIM-2013, this doping is calculated to be in the order of parts per billion (50 ppb for Pt, 130 ppb for SrTiO_3). Such a small concentration should not create any considerable effect.

In addition, a typical lithium ion can create multiple Frenkel pairs (~ 80 defects/ion in Pt, ~ 90 defects/ion in SrTiO_3), so their concentrations are expected to be higher. Using again SRIM, their concentration was calculated in the order of 100

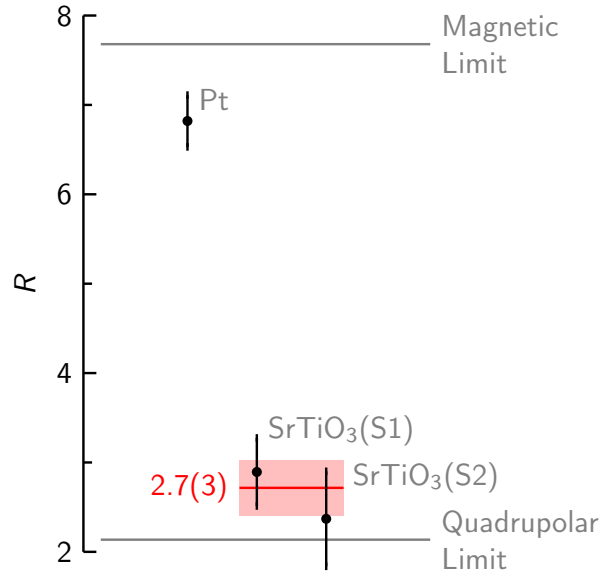


Figure 3.8: Ratios of ${}^9\text{Li}$ to ${}^8\text{Li}$ $1/T_1$ relaxation rates in Pt (weighted average of all measurements) and in the two SrTiO_3 samples. The red line represents the weighted average of the measurements in both SrTiO_3 samples.

ppm in SrTiO_3 and ~ 50 ppm in Pt. These numbers correspond to the upper limit of Frenkel pairs present, as in reality some would anneal away quickly. Note that these defects would be formed gradually with time, i.e., they would affect primarily the measurements taken last. Such time-dependence was not observed, though. Also, here we assume that there is no recombination of the created Frenkel pairs, which, given the temperature of the experiments, should not be the case. Therefore, these concentrations represent the upper boundary of the extrinsic defects.

In comparison, the intrinsic defects in SrTiO_3 (primarily O vacancies) are in the $\sim 1\%$ range, orders of magnitude higher than even the upper limit of extrinsically caused defects. From that, we conclude that the small magnetic part of the relaxation in SrTiO_3 was not caused by the beam implantation.

3.3 Enhancing the Effective Asymmetry of ${}^9\text{Li}$ Using α -tagging

Fig. 3.2 and 3.5 reveal that the uncertainty associated with the ${}^9\text{Li}$ measurements was much larger than ${}^8\text{Li}$, even though we typically spent ~ 10 times more time for

the acquisition of the ${}^9\text{Li}$ spectra. The figure of merit for a β -NMR measurement is A^2N , where A is the observable asymmetry and N is the total number of decay events — both factors for ${}^9\text{Li}$ are significantly reduced relative to ${}^8\text{Li}$. Since ${}^9\text{Li}$ lies further away from the valley of nuclear stability, it has a shorter half-life and fewer ions were extracted from the ion source and delivered to the spectrometer ($\sim 10^6 \text{ s}^{-1}$ vs $\sim 10^7 \text{ s}^{-1}$ for ${}^8\text{Li}^+$). This in turn reduced the factor N for ${}^9\text{Li}$. Also, the asymmetry for ${}^9\text{Li}$ is much smaller than for ${}^8\text{Li}$ (see Sec. 3.3.1). As a result, about 90% of the data acquisition was spent on ${}^9\text{Li}$, since these results dominated our uncertainty in the ratio of the relaxation rates.

To further develop the capabilities of the isotopic comparison method in β -NMR, we designed a system that was able to enhance the effective initial asymmetry of ${}^9\text{Li}$ by a factor of ~ 2 . That system, coupled with the development of certain aspects of TRIUMF's ISAC facility that increased the intensity of ${}^9\text{Li}^+$ beams by a factor of ~ 10 , suppressed greatly the uncertainty of ${}^9\text{Li}$ measurements, making the figure of merit for ${}^9\text{Li}$ comparable to ${}^8\text{Li}$.

In this section the basis of the new system is presented (Sec. 3.3.1), followed by the proof-of-principle experiments (Sec. 3.3.2).

3.3.1 α LithEIA Method

The reduction in asymmetry for ${}^9\text{Li}$ compared to ${}^8\text{Li}$ is attributed to ${}^9\text{Li}$'s more complicated β -decay scheme (see Fig. 3.9).

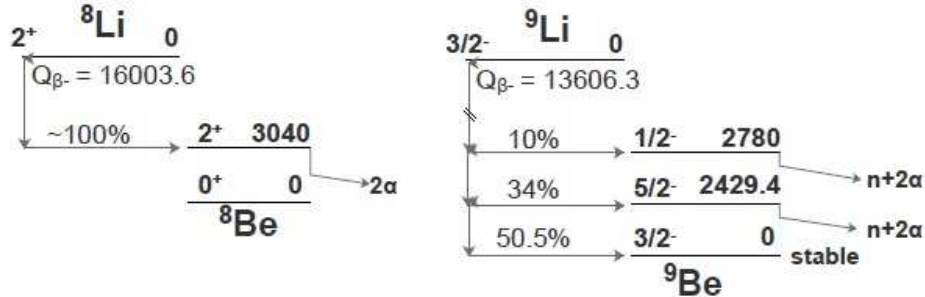


Figure 3.9: Properties of the principle β -decay modes of ${}^8\text{Li}$ and ${}^9\text{Li}$ [124]. Whereas ${}^8\text{Li}$ decays always to the first excited state of ${}^8\text{Be}$, ${}^9\text{Li}$ can decay to the ground state or one of the excited states of ${}^9\text{Be}$.

In particular, ${}^9\text{Li}$ has three main decay channels, two of which have opposite asymmetries that nearly cancel after weighting by the branching probabilities (Eq. 3.6).

$$a = a_{gs}p_{gs} + a_1p_1 + a_2p_2 = 0.505(-0.4) + 0.34(0.6) + 0.1(-1) = -0.096, \quad (3.6)$$

where a_{gs}, p_{gs} are the asymmetry and branching probability of the ${}^9\text{Li}$ β -decay to the ground state and a_i, p_i are the values associated with the decay to the i -th excited state of ${}^9\text{Be}$ (see Tab. 3.1).

Thus, most of the observed asymmetry derives effectively from the weakest decay mode which has a branching probability of only 0.1 but a large theoretical asymmetry parameter $a = -1.0$. The relevant branching probabilities and asymmetries of each decay mode are reported in Fig. 3.9.

Table 3.1: The asymmetry (a) of each decay mode of ${}^9\text{Li}$ [124]. The total asymmetry for ${}^9\text{Li}$ is the sum of the asymmetry weighted by the relevant probability of each decay mode.

${}^9\text{Be}$ state	Probability	I^π	a	Decay mode
ground state	50.5%	$3/2^-$	-2/5	stable
2429.4 MeV	34%	$5/2^-$	3/5	$n+2\alpha$
2780 MeV	10%	$1/2^-$	-1	$n+2\alpha$

From Tab. 3.1, note that by tagging the ${}^9\text{Li}$ β -events according to whether an α is emitted or not, it would be possible to distinguish between the decays going to the ground state of ${}^9\text{Be}$ versus the excited states and isolate their contributions. An efficient α -detection system can enhance the initial asymmetry of the ${}^9\text{Li}$ spectra significantly, since it should be possible to register two spectra in parallel, one with the β detected in coincidence with an α , and one without an α . Using Eq. 3.6, the former spectrum would have an initial asymmetry of $a = 0.236$, twice as big as that obtained without α -detection. The latter spectrum would have an increased initial asymmetry of $a = 0.4$ if the α -detection efficiency is close to 100%, making the effective asymmetry of the measurement 3 times larger than that without α -detection (see Fig. 3.10).

If the α -detection efficiency is lower than 100%, then some of the β -particles coming from a decay to an excited state of ${}^9\text{Be}$ would mistakenly be added to the anti-coincidence spectrum (i.e., β -with-no- α of Fig. 3.10). This would effectively lower the asymmetry of the anti-coincidence spectrum. The asymmetry of the anti-coincidence spectrum versus the α -detection efficiency is given by Eq. 3.7:

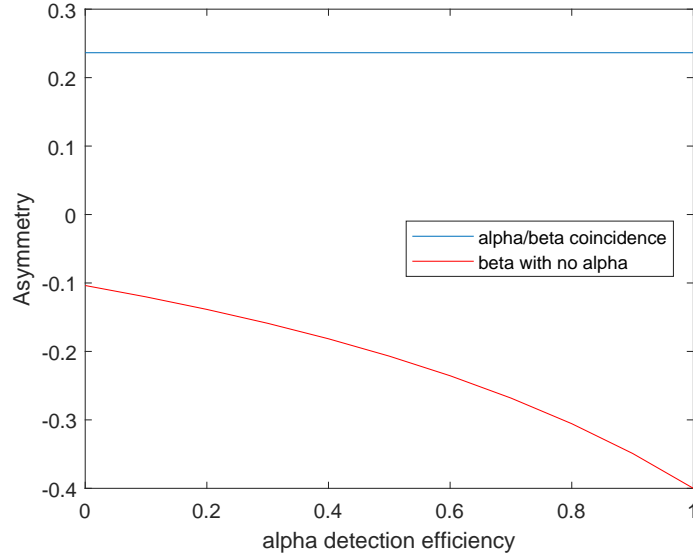


Figure 3.10: Theoretical initial β asymmetry detected in coincidence with an α (blue), or in the absence of an α (red), for varying α -detection efficiency. The asymmetry of the anti-coincidence spectrum depends on the α -detection efficiency because coincidence events with undetected α -particles would falsely mix the two spectra.

$$a_{b\bar{\alpha}}(e) = \frac{a_{gs}p_{gs} + a_1p_1 * (1 - e) + a_2p_2(1 - e)}{p_{gs} + p_1(1 - e) + p_2(1 - e)} = \frac{-0.202 + 0.158(1 - e)}{0.505 + 0.44(1 - e)}, \quad (3.7)$$

where e is the efficiency of the α -detector ($0 \leq e \leq 1$).

Also note, that when the ${}^9\text{Li}$ decays into an excited state of ${}^9\text{Be}$, it subsequently emits *two* α -particles, at an angle of 180° . This means that an efficient α -detector can register all decays that emit an α , by just covering half the solid angle, namely 2π , instead of the total 4π .

Thus, our proposed detection system consists of a hat-like detector over the sample with a hole for the beam to enter, as well as a system of lenses to guide the produced photons from the scintillator to a photomultiplier tube (PMT) outside the ultra high vacuum (UHV). Most of the α -particles will only have to cross a few nanometers of material (depending on the implantation depth) to reach the scintillator, so they will escape the sample without much attenuation. This has been confirmed with a Monte-Carlo Geant4 simulation [125].

This detection system will be referred henceforth as α LithEIA (α -detection for Lithium-9 Enhanced Initial Asymmetry), spelled “*alíthea*” from the Greek word for “truth” ($\alpha\lambda\acute{\eta}\theta\epsilon\iota\alpha$ ²). α LithEIA was incompatible with the current β -NMR and β -NQR cryostats (see Sec. 2.2.2), so we designed a new apparatus (the so-called “cryo-oven” (see Appendix A)) that would permit us to detect at the same time the α - and the β -particles, but also was designed to be an upgrade over the old β -NQR cryostat.

3.3.2 Experimental Testing of the α LithEIA Method on ZnS(Ag)

We decided to perform a proof of principle experiment of α LithEIA, using ZnS(Ag) as the sample. The main advantage of this is that it ensured a very high efficiency for detecting the α -particles, given that all the ${}^8\text{Li}^+$ stopped directly in the ZnS(Ag) scintillator. In other words, the ZnS(Ag) served both as the sample and the detector.

ZnS is a cubic material in the sphalerite form. When doped with Ag, the resulting compound is known to be an extremely bright scintillator [126] ($\sim 95,000$ photons/MeV). Commonly it is used in a polycrystalline form, sprayed as a powder on a surface. The incoming α -particles produce a high number of photons, with an intensity peak at a wavelength of 460 nm [127], caused by the recombination between shallow donors and simple silver substitutional acceptors [Ag_{Zn}] [128]. The small thickness of the powder suppresses significantly the scintillation due to incoming β -particles, which attenuate in a much longer range (see Sect. 5.2.2.4), making this material ideal for the α -detection system of this study.

In the first part of this experiment, we studied with ${}^8\text{Li}$ β -NMR a polycrystalline powder of ZnS doped with 6% Ag, deposited on a (fairly transparent) Al_2O_3 substrate. The light emitted from the α -particles propagating in the ZnS paste, was passing through the transparent substrate and was guided to a photomultiplier tube (PMT) lying outside vacuum, by a system of two convex lenses. As the same α -detector assembly was used for the study of ${}^8\text{Li}^+$ diffusion, a more detailed discussion on the geometry of the detector can be found in Ch. 5. As a high α -detection efficiency is highly advantageous (see Fig. 3.10), the energy threshold of the PMT was set just above the noise level.

We acquired a ${}^8\text{Li}$ resonance spectrum at 10 K (Fig. 3.11) and in addition verified that the scintillating properties of this material are unchanged in a wide range of temperatures (5-310 K), by imaging the scintillation produced by the implanted beam with a CCD camera.

The resonance spectrum was fitted best with two Lorentzian curves, both centered at the same frequency (129.197(4) kHz). The two curves had very different

² $\alpha\lambda\acute{\eta}\theta\epsilon\iota\alpha$ has an interesting etymology: $\alpha\lambda\acute{\eta}\theta\epsilon\iota\alpha > \alpha + \lambda\acute{\eta}\theta\eta$ = something that should not be forgotten, i.e., the truth.

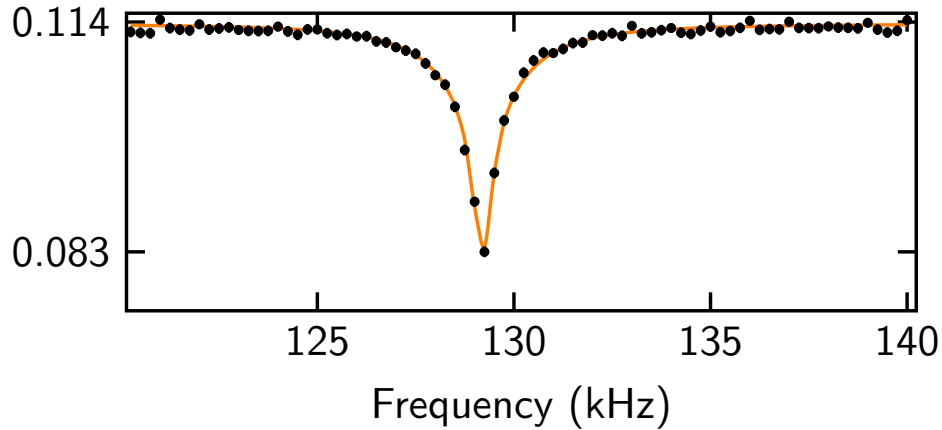


Figure 3.11: Resonance spectrum for ^8Li in $\text{ZnS}(\text{Ag})$ at 10 K.

widths: The narrow one had a FWHM of 0.64(5) kHz, whereas the wide line had a FWHM of 2.61(25) kHz. The amplitude of the narrow line was twice as big as that of the wide line.

Based on the unit cell structure of $\text{ZnS}(\text{Ag})$, we expect ^8Li ions to inhabit the tetrahedral interstitial sites, with four sulfur nearest neighbors (Fig. 3.12), as both Ag^+ and Zn^{2+} have a $(-1)e$ relative charge and this Li^+ is attracted to these centers.

The multicomponent nature of the resonance is most likely related to the disordered nature of the sample since it is $\sim 6\%$ Ag doped with other defects present as well. We attribute the narrow resonance to lithium ions being in a slowly relaxing environment, whereas the wide resonance should be due to ^8Li being at positions that lead to fast but inhomogeneous relaxation. Such centers of relaxation could be complexes of Ag^+ with other paramagnetic centers and other defects, which can produce a small EFG at the ^8Li site. Near the lithium implantation site, there are six possible sites for doped Ag ions to be. Thus, at a 6% doping level, there is a 31% probability of lithium to have at least one Ag ion as a (next-nearest) neighbor. This model is supported by the fact that the amplitude of the narrow resonance is twice as large as the wide resonance, i.e., $1/3$ of the resonance amplitude is due to the fast relaxing component and $2/3$ due to the slow component.

In addition to the resonance spectrum, the temperature dependence of SLR (Fig. 3.13) further supports the aforementioned model. The SLR spectra were fitted best with a two-component fit, with one of the two $1/T_1$ rates being systematically compatible with zero at all temperatures, therefore it was fixed to zero, leading to a fitting just like that of Eq. 3.5.

Evidently, both the fraction f of the relaxing component and the relaxation rate

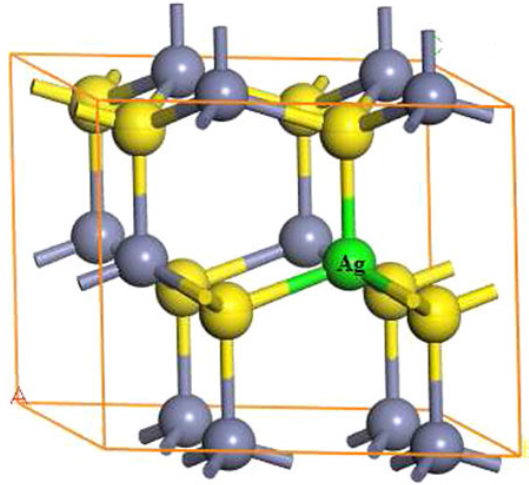


Figure 3.12: The crystal structure of ZnS(Ag). The yellow spheres represent S, the gray Zn and the green Ag ions. Implanted $^8\text{Li}^+$ is expected to occupy one of the tetrahedral interstitial sites, with four sulfur nearest neighbors. Adapted from Ref. [129].

$1/T_1$ are temperature-independent in the region 5 K to 225 K. In this temperature range, the fraction of the relaxing component is ~ 0.3 , further supporting the view that the relaxation is due to electric quadrupolar interactions of ^8Li with Ag atoms present at the vicinity. The relaxation rate $1/T_1$ is $\sim 1 \text{ s}^{-1}$ in this temperature range, but it increases up to 3 s^{-1} at 310 K. In the region 225 K to 310 K, the fraction f of the relaxing component increases as well, up to ~ 0.6 . This behavior is consistent with lithium becoming gradually mobile above 225 K, thus increasing the probability of being near at least one Ag ion for some time during its lifetime.

Turning to the ^9Li measurement, we measured an SLR spectrum at 310 K. In contrast to Sect. 3.2, this time we registered three spectra in parallel. Except for the regular (untagged) SLR spectrum without any consideration to the emitted α -particles, we also registered each count to either the coincidence (α -tagged) or the anti-coincidence (no- α -tagged) spectrum, depending on whether an α was also detected accompanying the β . These three spectra (with fits to Eq. 3.5) can be seen in Fig. 3.14.

From Fig. 3.14, note that both the α -tagged and the no- α -tagged spectra have a significantly increased initial asymmetry compared to the untagged spectrum, without any loss in statistics, since each untagged count is also stored in some of the two tagged spectra as well. The no- α -tagged spectrum had an initial asymmetry twice as big and the α -tagged spectrum four times as big as the untagged spectrum.

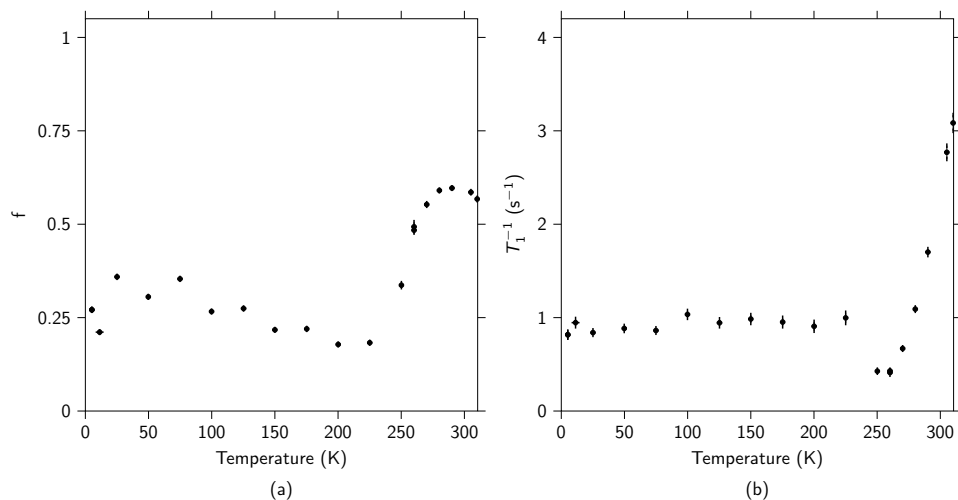


Figure 3.13: Temperature dependence of the fraction of the relaxing component f (left) and the relaxation rate $1/T_1$ (right) in ZnS(Ag).

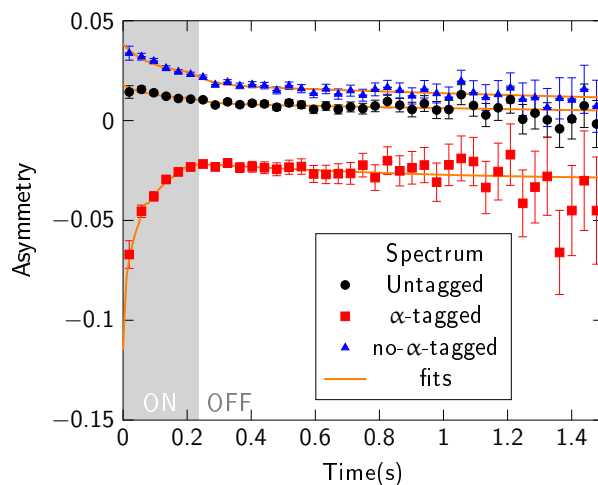


Figure 3.14: Untagged (black circles), α -tagged (red squares) and no- α -tagged (blue triangles) spectra of ^9Li β -NMR at 310 K in ZnS(Ag).

Tab. 3.1 indicates that the probability of ^9Li to decay with an α is 49.5%. Therefore, if our system could detect all α -decays, the α -tagged and no- α -tagged spectra would have roughly equal counts. Based on the number of counts stored at the two histograms, our α -detection efficiency was $\sim 50\%$.

Table 3.2: Fits of the untagged, α -tagged and no- α -tagged spectra of ^9Li β -NMR at 308 K in ZnS(Ag).

Spectrum	f	slow $1/T_1$ (s^{-1})	fast $1/T_1$ (s^{-1})	χ^2
Untagged	0.50(4)	0.41(15)	19(6)	1.15
no-α-tagged	0.480(20)	0.34(8)	18(3)	1.10
α-tagged	0.192(9)	0.000(5)	100(68)	1.06

From Tab. 3.2 it is evident that the fit of the anti-coincidence (i.e., no- α -tagged) spectrum agrees well with the fit of the untagged spectrum, but with uncertainties in its fit-parameters smaller by a factor of ~ 2 . The fit for the coincidence spectrum does not agree with either of the other two, due to the effect of rate-dependent distortion. Indeed, there is a pile-up effect present, due to which the energy threshold of the α -detector effectively decreases.

ZnS is known to emit light with a pulse having a long tail in time (Fig. 3.15).

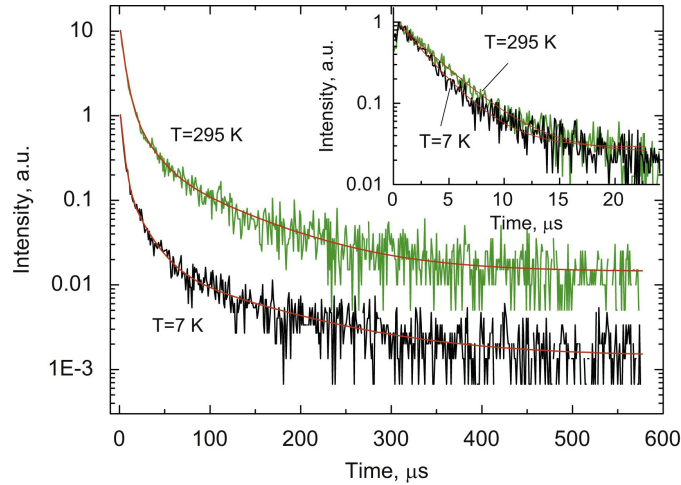


Figure 3.15: The normalized decay curves of the light emitted from a ZnS(Ag)/ ^6LiF scintillator illuminated with 5.5 MeV α -particles. Adapted from [130].

The decay time of ZnS(Ag) phosphors is longer for α -particles than γ 's and can be as long as 100 μs [131]. This can cause significant pile-up even for small α -rates, that artificially allows low-energy α -particles to pass over the detector's threshold. In this case, as the energy threshold was set just above noise, the pile-up effect resulted in noise being miscounted as α -events, thus mixing decays without

an α into the coincidence spectrum in a *time-dependent* manner.

Even though this time-dependent distortion effectively rendered the α -tagged spectrum unusable, we were able to increase the efficiency of the ${}^9\text{Li}$ measurement by a factor of ~ 2 , not very far from the maximum expected theoretical gain of ~ 3 (see Sect. 3.3.1). In Sect. 7.2, some ideas as to how to overcome this issue in the future will be presented.

3.4 Conclusions

We have measured the ratio between $1/T_1$ of ${}^9\text{Li}$ and ${}^8\text{Li}$ in Pt and SrTiO_3 in order to help identify the nature of the fluctuations responsible for the spin relaxation (i.e., if they are magnetic or electric quadrupolar). In Pt, the relaxation is single exponential and the ratio R_{Pt} was found to be very close to, but slightly less than, the pure magnetic limit. This is consistent with Korringa relaxation being dominant as suggested by the linear temperature dependence in $1/T_1$ reported previously. Nevertheless the small reduction in R_{Pt} relative to the pure magnetic limit means that excitations causing a fluctuating EFG may provide a small contribution to the observed spin relaxation.

In SrTiO_3 at 300 K the results confirm that the dominant source of relaxation is electric quadrupolar. However, the relaxation function is more complicated involving a relaxing part and a non-relaxing part. This suggests there is some inhomogeneous source of fluctuations/spin relaxation, possibly due to nearby defects. The ratio R_{STO} is close to, but slightly larger than, the pure quadrupolar limit, indicating that there may be some small magnetic contribution. However, the main source of spin relaxation is quadrupolar. This is consistent with expectations given the large quasi-static nuclear quadrupole interaction.

Most importantly, we have demonstrated that the method of isotope comparison can be used in β -NMR to distinguish the nature of the fluctuations responsible for $1/T_1$. This represents an important new tool for β -NMR, since in many systems there is uncertainty in the source of relaxation that cannot be removed simply by varying experimental parameters.

To further develop the method of isotopic comparison in β -NMR using ${}^8\text{Li}$ and ${}^9\text{Li}$, we designed and tested a system of tagging the β -particles coming from the decay of ${}^9\text{Li}$ in coincidence with/without an α -particle. This system was demonstrated to increase the effective asymmetry of ${}^9\text{Li}$ by a factor of ~ 2 . This development, coupled with the tenfold increase in ${}^9\text{Li}^+$ rate that was achieved recently at TRIUMF, increases the figure of merit of the ${}^9\text{Li}$ β -NMR measurements by a factor of ~ 40 , making it comparable with that of ${}^8\text{Li}$.

Chapter 4

Principles of Interstitial Diffusion in Solids

Diffusion of ions in solids is a mass transport mechanism of great significance for many branches of material engineering, fabrication and science. Its applications include – amongst others – diffusion hardening (e.g., steel), sintering and corrosion of metals, semiconductor doping, as well as solid state batteries, a subset of which (namely, the search for better Li-ion battery materials, see Sect. 1.2) is the main focus of the second part of this thesis.

In this Chapter, a short outline of the theory of interstitial (self)diffusion will be presented, both from a macroscopic (Sect. 4.1) and a microscopic (Sect. 4.2) point of view. The following two Chapters introduce the ^8Li α -radiotracer method both from a theoretical and computational (Ch. 5), as well as from an experimental perspective (Ch. 6).

4.1 Macroscopic Theory of Solid State Diffusion

In contrast to the cases of a species moving (diffusing) through a gas or a liquid, the diffusion in a (crystalline) solid is restricted and is based on one (or several) hopping mechanism(s).

We consider first solute atoms which occupy interstitial positions in the crystal lattice. In such a case, diffusion is mediated by the interstitial ions hopping from one energetically favorable site to the next, by passing over an energy barrier. The lattice atoms are not permanently displaced due to this process. This is called an *interstitial mechanism* for diffusion. This is conceptually the simplest process, but also the most relevant to this work, since Li diffusion in Li-ion battery materials is usually based on such a mechanism.

If the solute atoms are similar in size to that of the host crystal atoms, then they can substitute a lattice ion and form a substitutional solution. The diffusion of such atoms relies on the existence of vacancies close to the solute atom, since in this case it can jump to the neighboring vacancy. This process is called a *vacancy mechanism* for substitutional diffusion and it is generally slower than the simple interstitial case

(under the same thermodynamical conditions).

Several other cases exist in between the two mechanisms discussed above, such as divacancy substitutional diffusion (requiring two vacancies close to the solute atom), or interstitialcy (i.e., indirect interstitial) diffusion, which is a collective motion of an interstitial solute atom and an interstitial host atom.

The scope of this chapter is to provide the theoretical framework for the study of Li interstitial diffusion in Li-ion battery materials, so only this case will be presented.

4.1.1 Fick's Laws

4.1.1.1 First law

From a macroscopic point of view, the diffusion of a species (e.g., atoms of a specific element or isotope) in a solid is described by Fick's laws. The first law is defined by the formula:

$$\mathbf{j} = -\mathcal{D} \nabla c, \quad (4.1)$$

where \mathbf{j} is the flux, i.e., the number of atoms passing through a cross-sectional area per unit time, \mathcal{D} is the diffusion coefficient tensor and c is the concentration of the diffusive species, namely the number of atoms per unit volume. The dimensions of the diffusion tensor are length squared over time, so it is measured in units of m^2/s (or cm^2/s).

In isotropic media, such as cubic crystals, icosahedral quasi-crystals, or amorphous metals, the diffusion tensor reduces to a scalar D (i.e., is direction-independent), but generally is a symmetric tensor of rank 2. Every such tensor can be written in diagonal form, so Eq. 4.1 reduces to a system of three equations after rotating the coordinate system to that of the orthogonal principal directions (x_1, x_2, x_3):

$$j_1 = -D_1 \frac{dc}{dx_1}, j_2 = -D_2 \frac{dc}{dx_2}, j_3 = -D_3 \frac{dc}{dx_3} \quad (4.2)$$

where D_1, D_2, D_3 are called the principal diffusivities. Generally these three can be unequal and the diffusion along a random direction (a_1, a_2, a_3) is given by:

$$D(a_1, a_2, a_3) = D_1 \cos^2(\theta_1) + D_2 \cos^2(\theta_2) + D_3 \cos^2(\theta_3) \quad (4.3)$$

where θ_i denotes the angle between a_i and the principal axis-i.

In the case of systems with uniaxial symmetry, such as tetragonal, hexagonal or trigonal lattices, two of the principal diffusivities are equal and the diffusion coefficient depends only on the angle Θ between the direction in question and the axis of symmetry:

$$D(\Theta) = D_1 \sin^2(\Theta) + D_3 \cos^2(\Theta) \quad (4.4)$$

4.1.1.2 Second law

The second Fick's law can be derived from the first law (Eq. 4.1), if coupled to a conservation (or continuity) equation:

$$\frac{\partial c}{\partial t} = -\nabla \cdot \mathbf{j} \quad (4.5)$$

Equation 4.5 holds if the species undergoing diffusion is conserved (i.e., doesn't take part in chemical reactions, radioactive decay etc). In such cases, coupling Eq.4.1 and Eq. 4.5 leads to Fick's second law:

$$\frac{\partial c}{\partial t} = \nabla \cdot (\mathcal{D} \nabla c) \quad (4.6)$$

If the diffusivity does not depend on the concentration – which is always the case for tracer studies like the present –, then the diffusion equation along direction x is given by:

$$\frac{\partial c}{\partial t} = D \frac{\partial^2 c}{\partial x^2} \quad (4.7)$$

Eq. 4.7 is usually referred to as the diffusion equation. This can be solved analytically under given initial and boundary conditions.

4.1.1.3 Infinite medium solution

In the case of diffusion in an infinite 1D medium, starting with a concentration $c(0,0)$ at $x = 0$ at time $t = 0$ and $c(x,0) = 0$ elsewhere, Eq. 4.7 yields the following solution:

$$c(x,t) = \frac{c(0,0)}{2\sqrt{\pi Dt}} \exp(-x^2/4Dt) \quad (4.8)$$

The characteristic length scale of this equation is the so-called *diffusion length* $\sqrt{2Dt}$.

4.1.2 Temperature Dependence of Diffusion: Arrhenius Law

Generally speaking, the diffusivity (also known as diffusion rate) is temperature and pressure dependent. Temperature especially has a pronounced effect on the diffusion rate, which is suppressed at low temperatures and rises rapidly with increased T . It

is found empirically that in many cases (but not always) the diffusion rate over a certain temperature interval follows Arrhenius law:

$$D(T) = D'_0 \exp(-\Delta H/k_B T), \quad (4.9)$$

where ΔH is the activation enthalpy of diffusion (in units of eV/atom), k_B is the thermodynamic Boltzmann constant and D'_0 is the so-called pre-exponential factor. The latter can be written as:

$$D'_0 = D_0 \exp(\Delta S/k_B), \quad (4.10)$$

where ΔS is the diffusion entropy and D_0 can be calculated using the Einstein-Smoluchowski relation (see Sect. 4.2.3). Using the thermodynamic equation at constant pressure:

$$\Delta G = \Delta H - T\Delta S, \quad (4.11)$$

where ΔG is the Gibbs free energy of activation, Eq. 4.9 can be written in terms of D_0 directly as:

$$D(T) = D_0 \exp(-\Delta G/k_B T), \quad (4.12)$$

Note that the thermodynamic Gibbs free energy of activation corresponds to the activation energy E_A defined by the characteristics of the particle's microscopic motion (see Sect. 4.2.3).

An Arrhenius diagram depicts the logarithm of the diffusion rate (in units of m^2/s or similar) versus inversed temperature (in K^{-1}), i.e., the graphical representation of the function $\log_{10}[D(1/T)]$. If the system under study follows Arrhenius law, then its Arrhenius diagram will be linear, with the slope being $-\Delta H/k_B$ (or equivalently $-E_A/k_B$).

4.2 Microscopic Theory of Diffusion

The macroscopic theory of diffusion follows the example of classical thermodynamics, both in the concepts it employs (Gibbs free energy, diffusion entropy, etc), as well as in the way of viewing the corresponding phenomena. This parallelism extends also to the fact that the laws of both macroscopic theories can be derived from microscopic statistical arguments. The microscopic (or atomistic) path to diffusion is the subject of this section, which aims to recover Fick's second law and to relate the diffusion pre-exponential factor D_0 and Gibbs free energy for diffusion ΔG with microscopic parameters of the lattice and its vibrations.

To that end, the problem of the random walk of a particle in a (rigid) lattice will be considered, both in the case of diffusion in an “infinite” lattice, as well as in the case of diffusion close to a surface. The connection of this construct to Fick’s formalism is achieved by using Einstein-Smoluchowski’s law (Sect. 4.2.3).

4.2.1 One Dimensional Random Walk

Before discussing the problem of the random walk of a particle in a lattice, it is important to address a common misconception about the term “random” in this context. In this classical treatment, the individual particles (ions, molecules, atoms, etc) do not move randomly at any given point in time, but rather they follow a trajectory governed by the potential landscape of the lattice around them, as well as their momentum. The randomness of their long-range motion stems from the stochastic collisions between the diffusive species and their lattice neighbors. These collisions change the magnitude and direction of the particles’ momentum, making their apparent motion to seem random, when viewed in isolation from their environment.

The general formulation of the random walk problem contains a number n_p of particles, each undergoing a series of N random displacements $\mathbf{r}_1, \mathbf{r}_2, \dots, \mathbf{r}_N$ with each step being independent of the previous ones both in direction and magnitude, but with the probability of \mathbf{r}_i lying between \mathbf{r} and $\mathbf{r} + d\mathbf{r}$ governed by a pre-defined distribution function $\tau_i(\mathbf{r})$. The diffusion process is then given by calculating the probability $W(\mathbf{R})d\mathbf{R}$ that the particle will be at the interval $[\mathbf{R}, \mathbf{R} + d\mathbf{R}]$ after N displacements [132].

Studying the one-dimensional random walk of a particle is the simplest case of the aforementioned scenario and is very relevant to this work, since the diffusion of lithium in rutile TiO_2 – which was selected to be the test case of the technique for studying nanometer scale lithium diffusion presented in this thesis – is known to be highly one dimensional (see Sect. 6.1).

In the case of an one dimensional random walk, we assume that each particle is displaced by steps of equal length l , but with each step having equal probability ($1/2$) to move the particle to the left or to the right. After N steps, the possible positions of a particle starting at 0 is:

$$-N, -N + 1, \dots, 0, N - 1, N, \quad (4.13)$$

where the x-coordinate of the i -th point is given by $i \cdot l$.

To calculate the probability $W(m, N)$ of the particle being at point m after N displacements, note that this would be given simply by multiplying the number of different paths that would lead the particle to point m after N steps with the

probability of each path, normalized to the total number of possible paths with N steps.

Since the probabilities of stepping to the left and to the right are both $1/2$, all paths should be assigned equal probability of $(\frac{1}{2})^N$. Also, to arrive at point m the particle should undergo $(N+m)/2$ steps to the right and $(N-m)/2$ to the left. This is clearly a Bernoulli situation with:

$$W(m, N) = \frac{N!}{[(N-m)/2]![(N+m)/2]!} \left(\frac{1}{2}\right)^N, \quad (4.14)$$

In the limit of $N \rightarrow \infty$ and $m \ll N$ Eq. 4.14 can be simplified using Stirling's formula:

$$\log(n!) = (n + \frac{1}{2})\log(n) - n + \frac{1}{2}\log(2\pi) + O(n^{-1})(n \rightarrow \infty) \quad (4.15)$$

to give:

$$\log(W(m, N)) \simeq -\frac{1}{2}\log(N) + \log(2) - \frac{1}{2}\log(2\pi) - m^2/2N \quad (4.16)$$

which, for large N , leads to the asymptotic formula:

$$W(m, N) = \sqrt{2/\pi N} \exp(-m^2/2N) \quad (4.17)$$

The natural choice for the coordinate for 1D-diffusion is the displacement $x = m \cdot l$. The probability $W(x, N)\Delta x$ is connected to Eq. 4.17 by:

$$\begin{aligned} W(x, N)\Delta x &= W(m, N)\left(\frac{\Delta x}{2l}\right) \\ &= \frac{1}{\sqrt{2\pi N}l^2} \exp(-x^2/2Nl^2) \end{aligned} \quad (4.18)$$

The final step is to insert time into the probability equation, as diffusion is of course a time-dependent process. Assuming that the particle undergoes n displacements per unit time, we can define the diffusion rate as $D = \frac{1}{2}nl^2$ using the Einstein-Smoluchowski relation (see Sect. 4.2.3). After time t , there is (by construction) a number of $N = nt$ displacements, so $Dt = \frac{1}{2}Nl^2$. Equation 4.18 can be rewritten thusly:

$$W(x, t)\Delta x = \frac{1}{2\sqrt{\pi Dt}} \exp(-x^2/4Dt)\Delta x \quad (4.19)$$

A comparison with Eq. 4.8 shows that this statistical analysis of the microscopic interstitial motion recovers the 1D solution of Fick's law (in the limit of a large number of particles and steps).

4.2.2 Boundary Conditions

Equation 4.19 determines the probability of a particle starting at $x = 0$ at time $t = 0$ to be in the interval $[x, x+\Delta x]$ at time t . It supposes an infinite medium in both directions. A very important question, with very relevant consequences for this work, is how Eq. 4.19 would be affected under certain boundary conditions.

In reality, no medium is infinite. Particles diffusing in a crystal (e.g., lithium ions in rutile TiO_2 , see Ch. 5-6) would reach after some time one of the surfaces of the crystal. There, they would either get trapped – thus, their diffusion would come to a stop –, or they would get reflected. Here these two boundary conditions are presented.

4.2.2.1 Absorbing surface

Turning first the case of an absorbing surface at a distance of $m = m_1$ steps away from the starting point $m = 0$. This trapping surface is supposed to absorb all particles that reach it, which means that any diffusing particle that arrives there is not allowed to move any more. Due to that, there are two important questions to answer in this case, namely what is the probability of a particle arriving at some point m after N displacements and also what is the rate of absorption at the surface $m = m_1$.

To calculate the probability $W(m, N; m_1)$, the only difference with the simple case of an infinite medium presented at Sect. 4.2.1 is that all paths that arrive to point m after passing through point m_1 should be excluded. Every such forbidden path can be thought as a path to the image point $(2m_1 - m)$, thus the probability of arriving at point m under the absorbing boundary condition can be written in terms of Eq. 4.17 as:

$$\begin{aligned} W(m, N; m_1) &= W(m, N) - W(2m_1 - m, N) \\ &= \sqrt{2/\pi N} [\exp(-m^2/2N) - \exp(-(2m_1 - m)^2/2N)] (N \rightarrow \infty) \end{aligned} \quad (4.20)$$

By introducing the coordinate x and the diffusion rate D , one can write Eq. 4.20 in a form similar to Eq. 4.19:

$$W(x,t;x_1) = \frac{1}{2\sqrt{\pi Dt}} [\exp(-x^2/4Dt) - \exp(-(2x_1 - x)^2/4Dt)] \quad (4.21)$$

This formula is valid for all $x < x_1$. For $x > x_1$ the probability is zero by construction (all particles will get absorbed before reaching that point).

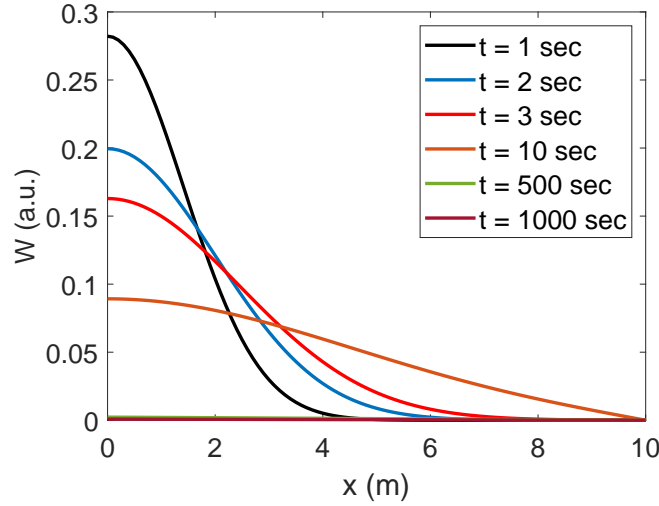


Figure 4.1: Examples of density profiles $W(x,t)$ starting with all particles at the $x = 0$ surface at $t = 0$ (i.e., $W(0,0) = 1$) and diffusing with $D = 1 \text{ m}^2 \text{ s}^{-1}$. There is an accumulative wall at $x = 10 \text{ m}$ which traps all particles reaching it. As a result, the density tends to even out in the $0 \leq x < 10$ space and also gradually get suppressed (e.g., see the profiles for $t = 500$ and $t = 1000$ sec), as more and more particles end up trapped at the wall.

Turning to the second question raised upon defining the current boundary condition, namely what is the rate of absorption at the trapping surface, note that this is given by the probability $a(m_1, N)$ of arriving at the point $m = m_1$ after exactly N steps, excluding all paths that pass through m_1 at an earlier step.

Using similar arguments as above, this probability is given by:

$$\begin{aligned} a(m_1, N) &= \frac{m_1}{N} W(m_1, N) \\ &= \frac{m_1}{N} \sqrt{\frac{2}{\pi N}} \exp(-m_1^2/2N) (N \rightarrow \infty) \end{aligned} \quad (4.22)$$

Finally, by the usual change of variables, one finds the rate of absorption:

$$\frac{da}{dt}(x_1, t) = \frac{x_1}{t} \frac{1}{2\sqrt{\pi Dt}} \exp(-x_1^2/4Dt) \quad (4.23)$$

4.2.2.2 Reflecting surface

In the case of having a reflecting surface at point $m = m_1$, then the probability of arriving at a point m after N displacements is given by simply adding the probability given by Eq. 4.17 with that for arriving at the “image” of m relative to the boundary surface, $2m_1 - m$, again as it would have been calculated in the absence of a boundary condition. Therefore:

$$\begin{aligned} W(m, N; m_1) &= W(m, N) + W(2m_1 - m, N) \\ &= \sqrt{2/\pi N} [\exp(-m^2/2N) + \exp(-(2m_1 - m)^2/2N)] (N \rightarrow \infty) \end{aligned} \quad (4.24)$$

Which leads after changing the variables to the diffusion equation:

$$W(x, t; x_1) = \frac{1}{2\sqrt{\pi Dt}} [\exp(-x^2/4Dt) + \exp(-(2x_1 - x)^2/4Dt)] \quad (4.25)$$

Notice that the only difference of Eq. 4.25 with Eq. 4.21 is the sign of the term corresponding to the image point $2x_1 - x$.

4.2.3 Einstein-Smoluchowski Law

Einstein-Smoluchowski law connects the macroscopically defined diffusion rate D (see Sect. 4.1.1) with the microscopic random motion of the diffusing particles, via the relation:

$$D = \frac{1}{2dt} \langle \mathbf{R}^2 \rangle, \quad (4.26)$$

where d is the dimensionality of the diffusion – i.e., (one half of) the possible diffusion paths on the lattice – and $\langle \mathbf{R}^2 \rangle$ is the mean square displacement of the particle after stepping at random n -times in a time interval t .

\mathbf{R} is by construction:

$$\mathbf{R} = \sum_{i=1}^n \mathbf{r}_i \quad (4.27)$$

Thus:

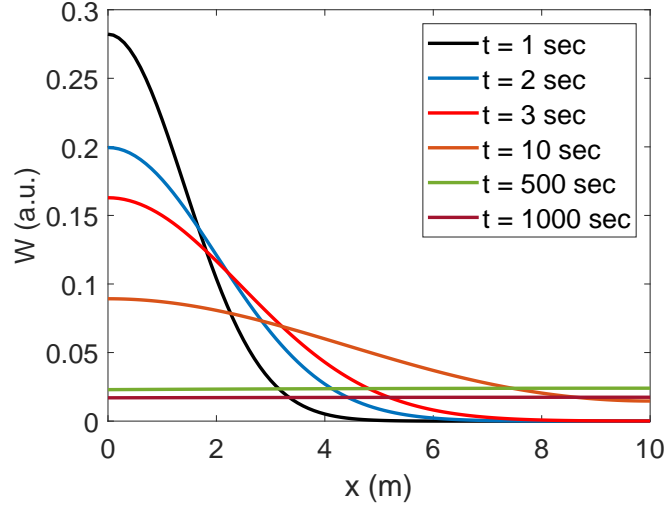


Figure 4.2: Examples of density profiles $W(x, t)$ starting with all particles at the $x = 0$ surface at $t = 0$ (i.e., $W(0, 0) = 1$) and diffusing with $D = 1 \text{ m}^2 \text{ s}^{-1}$. In contrast to Fig. 4.1 there is now a reflective wall at $x = 10 \text{ m}$. This change has minimal effect at early times, when the density tends to even out in the $0 \leq x < 10$ space, but at the long time limit $W(x, t)$ does not get suppressed.

$$\mathbf{R}^2 = \sum_{i=1}^n \mathbf{r}_i^2 + 2 \sum_{i=1}^n \sum_{j=i+1}^n \mathbf{r}_i \mathbf{r}_j \quad (4.28)$$

Which leads to the following expression for $\langle \mathbf{R}^2 \rangle$:

$$\langle \mathbf{R}^2 \rangle = \sum_{i=1}^n \langle \mathbf{r}_i^2 \rangle + 2 \sum_{i=1}^n \sum_{j=i+1}^n \langle \mathbf{r}_i \mathbf{r}_j \rangle \quad (4.29)$$

If the steps are uncorrelated (i.e., the walk is truly random), then the second term averages to zero. Using this fact, one can define the degree of randomness of the walk using the correlation factor f , defined as:

$$f = \lim_{n \rightarrow \infty} \frac{\langle \mathbf{R}^2 \rangle}{\sum_{i=1}^n \langle \mathbf{r}_i^2 \rangle} = 1 + 2 \lim_{n \rightarrow \infty} \frac{\sum_{i=1}^n \sum_{j=i+1}^n \langle \mathbf{r}_i \mathbf{r}_j \rangle}{\sum_{i=1}^n \langle \mathbf{r}_i^2 \rangle} \quad (4.30)$$

For a true random walk, $f = 1$. For dilute interstitial diffusion (which is the focus of this thesis), usually this is the case. This is so, because most neighboring interstitial sites are empty, hence a jump towards any one of them is equally probable and independent of the previous hop.

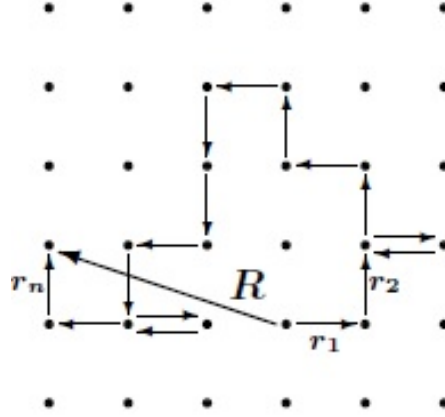


Figure 4.3: Image of n individual random steps \mathbf{r}_i on a lattice, leading to a total displacement \mathbf{R} . Adopted from [54].

If the average step length is l , then:

$$\sum_{i=1}^n \langle \mathbf{r}_i^2 \rangle = nl^2 \quad (4.31)$$

Combining Eq. 4.30 and Eq. 4.31 with Einstein-Smoluchowski law (Eq. 4.26), yields:

$$D = \frac{fnl^2}{2dt} \quad (4.32)$$

To write Eq. 4.32 in a form independent of the number of steps n , one can define the mean residence time τ of a particle at a certain lattice position. The inverse of the mean residence time, τ^{-1} is called the hop rate. By the construction of the problem, the particle undergoes n displacements in time t , so $\tau = t/n$. Substituting this to Eq. 4.32:

$$D = \frac{fl^2}{2d\tau} \quad (4.33)$$

This is the most commonly used form of the Einstein-Smoluchowski expression, since it connects the macroscopically defined diffusion rate with microscopic properties of the lattice and the particle motion that can be found experimentally or through simulations.

Physically, a particle in a lattice hops from an energetically favorable site to the next, by overcoming the potential barrier separating the two. The height of the barrier is equal to the energy difference E_A between the particle's equilibrium position and that of the barrier's saddle point (see Fig. 4.4). E_A is called the activation energy.

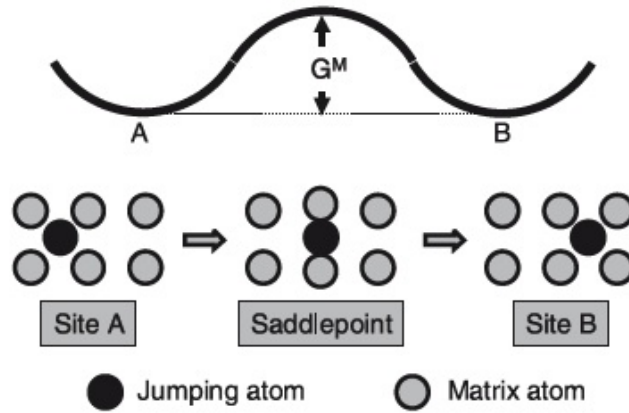


Figure 4.4: Interstitial atom's jumping process. It hops from site A to site B by moving through the saddle point. The energy difference between the energetically favored initial (and final) sites with the saddle point defines the energy barrier E_A . This is also the difference of Gibbs free energy G^M between these points, assuming that the process is reversible (and thus $\Delta S \sim 0$). Adapted from [54].

The hopping over the barrier is possible because at a non-zero temperature the lattice atoms vibrate around their equilibrium positions and this fluctuation of thermal energy provides the particles with enough kinetic energy to overcome the barrier. The frequency of this vibration τ_0^{-1} is of the order of the Debye frequency, with typical values of 10^{12} Hz to 10^{13} Hz. The hop rate would be then equal to $\tau_0^{-1} \equiv \nu^0$ – also known as the attempt frequency – multiplied by the probability of having enough energy to overcome the barrier. This probability follows the Boltzmann distribution, so [133]:

$$\tau^{-1} = \tau_0^{-1} \exp\left(-\frac{E_A}{k_B T}\right) \quad (4.34)$$

Note that Eq. 4.34 leads to Arrhenius law (Eq. 4.9) by substituting τ^{-1} in Eq. 4.33. Then:

$$\begin{aligned}
D &= \frac{fl^2}{2d\tau} \\
&= \frac{fl^2}{2d} \tau_0^{-1} \exp\left(-\frac{E_A}{k_B T}\right) \\
&= D_0 \exp\left(-\frac{E_A}{k_B T}\right)
\end{aligned} \tag{4.35}$$

4.2.4 Isotopic mass effect on diffusion

As a final note on the theory of interstitial diffusion, the isotopic effect will be briefly discussed. Since in this work Li diffusion in solids is studied through the radioactive decay of ^8Li , it is important to address how different the diffusion rate of ^8Li (compared to the stable $^6,7\text{Li}$) is expected to be under identical circumstances.

In the general case, let there be two isotopes of the same element, with relevant masses m_α and m_β . Due to the different masses, the two isotopes are expected to diffuse through the lattice with different diffusion coefficients D_α and D_β .

To quantify the above discussion, Eq. 4.34 will be used, with the notational substitution $\tau^{-1} \equiv \omega$ and $\tau_0^{-1} \equiv v^0$:

$$\omega_{\alpha,\beta} = v_{\alpha,\beta}^0 \exp\left(-\frac{E_{\alpha,\beta}^A}{k_B T}\right) \equiv v_{\alpha,\beta}^0 \exp\left(-\frac{\Delta H_{\alpha,\beta}^M}{k_B T}\right) \tag{4.36}$$

where ΔH^M is the activation enthalpy of diffusion defined at Eq. 4.9. The relevant quantities for the two isotopes are to be distinguished by the use of subscripts, e.g., $v_\alpha^0, v_\beta^0; \Delta H_\alpha^M, \Delta H_\beta^M$.

Under identical thermodynamical conditions, the diffusion barrier is expected to be independent of the mass of each isotope, since all isotopes of the same element have by definition equal charges. This leads to $E_\alpha^A = E_\beta^A = E^A$, or equivalently:

$$\Delta H_\alpha^M = \Delta H_\beta^M = \Delta H^M \tag{4.37}$$

The only exception to the above statement is hydrogen (and to a lesser extent helium). For these very light nuclei, quantum tunneling and zero-point motion cannot be neglected and since these effects are mass dependent, the effective diffusion barrier for, e.g., ^1H and ^2H are expected to be different. For heavier ions, these effects are negligible.

Using Eq. 4.36 to form the ratio of the jump rates, taking into account Eq. 4.37:

$$\frac{\omega_\alpha}{\omega_\beta} = \frac{v_\alpha^0}{v_\beta^0} \tag{4.38}$$

According to the classical rate theory [134], the attempt frequency ν^0 is the vibration frequency of the atom at the direction of the jump attempt. The vibration frequency can then be related to the isotopic mass by imposing Einstein's model for the vibrational frequencies of atoms in a crystal, which treats each atom as an independent (quantum) harmonic oscillator. ν^0 turns out to be proportional to the inverse square root of the mass, thus:

$$\frac{D_\alpha}{D_\beta} = \frac{\nu_\alpha^0}{\nu_\beta^0} \approx \sqrt{\frac{m_\beta}{m_\alpha}} \quad (4.39)$$

For the case of ^8Li vs $^{6,7}\text{Li}$, using Eq. 4.39 the diffusion coefficients for the three isotopes yield: $D_6 = 1.15D_8$ and $D_7 = 1.07D_8$. In other words, according to Einstein's simple model, the diffusion coefficient extracted from ^8Li diffusion should be 10-15% lower than what would be for $^{6,7}\text{Li}$ under identical circumstances. Indeed, for the system studied in the following Chapters, namely Li diffusion in rutile TiO_2 , Eq. 4.39 has been found experimentally to be valid, within error [70] and no isotopic effects on the diffusion barrier were reported.

Chapter 5

Principles of Studying Nanoscale Lithium Diffusion Using the α -Decay of ^8Li

5.1 Basic Principles of the ^8Li α -radiotracer Technique

As part of this thesis we have developed a novel method for directly measuring the rate with which Li ions diffuse inside materials and potentially across their interfaces, namely the ^8Li α -radiotracer method. The primary practical interest is in regard to Li-ion batteries, where Li diffusion determines the charging/discharging rate of the battery and thus is a very important characteristic of all the key components of a Li battery, i.e., the anode, cathode and electrolyte (see Ch. 1.2). In addition, this method can determine whether Li^+ gets reflected or trapped upon reaching the surface of the sample, a fact that is very hard to establish with other techniques. The surface boundary condition for the Li^+ motion can critically affect the ease of Li intercalation in a given material.

The method is a variation of the classical radiotracer method and uses the attenuation of the progeny α -particles from the radioactive decay of ^8Li , to study nanoscale Li diffusion. As explained in Ch. 2, ^8Li decays to one β -particle, two α 's and an electron antineutrino. The energy of an α -particle is attenuated significantly over a depth of 100 nm, which can be comparable to the diffusion length of ^8Li within its radioactive lifetime. The energetic β -particles, on the other hand, are much more weakly attenuated and thus can serve as a convenient way to normalization for the overall ^8Li decay rate.

To measure Li diffusion, a short beam pulse of low energy (0.1 – 30 keV) $^8\text{Li}^+$ ions is implanted close to the surface of the sample (at an average depth of ~ 100 nm) housed in an ultra-high vacuum cold finger cryostat [33, 123]. The energy of the beam defines the initial Li^+ implantation profile. Upon arrival, the $^8\text{Li}^+$ start to diffuse through the sample and undergo β -decay to ^8Be which then decay (immediately) into two energetic α -particles, each with mean energy of 1.6 MeV. Due to their rapid attenuation inside the sample, the highest energy α -particles

escaping the sample originate from ${}^8\text{Li}^+$ that have diffused back to the surface. To further amplify the sensitivity to ${}^8\text{Li}^+$ near the surface, the α -detector is placed at a grazing angle, $\theta \leq 4.4^\circ$, relative to the surface, as shown in Fig. 5.1.

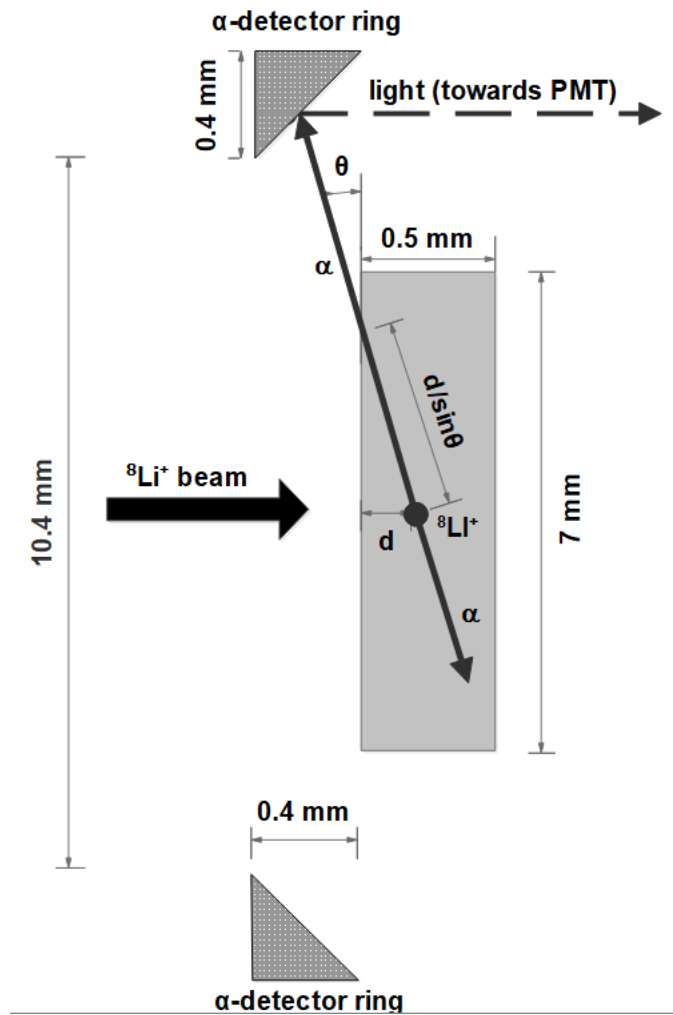


Figure 5.1: Schematic of the ultra-high vacuum (10^{-10} Torr) sample region showing the cross-section of the ring detector. The α -particles originating at depth d that reach the α -detector traverse distance $d/\sin\theta$ [77]. Not to scale.

The α -detector in our setup is an Al ring, whose inside surface is cut at $\sim 45^\circ$ and coated with a thin layer of Ag-doped ZnS, a well known scintillator sensitive

to α -particles [131]. Note that the results of the simulation study presented here are not heavily dependent on the type of the detector, as long as its thickness is sufficient to stop α -particles and at the same time thin enough to keep the β energy deposition inside it to a minimum (see Sect. 5.2.2.4).

The light from the ZnS(Ag) scintillator is collected in the forward direction using two 5 cm \varnothing convex lenses (see Fig. 5.2) which focus the light onto the photo-cathode of a fast photomultiplier tube (PMT). The first lens is attached at the radiation shield of the cryostat – inside the ultrahigh vacuum region –, whereas the second lens and the PMT are positioned outside the vacuum chamber, behind a transparent viewport. A stainless steel tube that is housing the PMT is attached around the optical viewport in order to block all ambient light from reaching the photomultiplier. The PMT pulses have a large signal to noise ratio (> 10) and pass through a timing filter amplifier to be discriminated, so that only the top 1/3 of pulses above the noise level are counted.

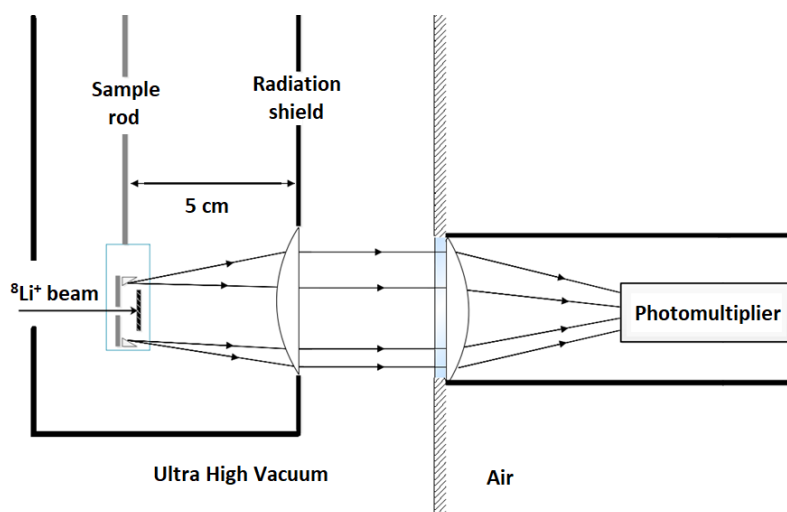


Figure 5.2: Schematic of the α -detection geometry, not to scale. The ${}^8\text{Li}^+$ beam comes from the left of the figure and reaches the $7 \times 7 \times 0.5 \text{ mm}^3$ sample after passing through a pinhole Al collimator, which ensures a centered beam. The α -particles that reach the ZnS scintillator produce light (drawn here as black arrows), which propagates through a series of two focusing lenses towards the face of a photomultiplier tube, lying outside vacuum inside a stainless steel housing that blocks all ambient light. The lens closest to the sample is placed about one focal length away from it ($\sim 5 \text{ cm}$).

To ensure a stable, well defined ${}^8\text{Li}^+$ beamspot at the center of the sample, an

aluminum mask can be placed in front of the sample-detector region, having a small hole (2 mm to 3 mm diameter) at its center to allow for the beam to enter. This system does not allow for beam near the edge of the sample, for that could change artificially the diffusion signal.

This system was incompatible with the geometry of the β -NQR cryostat and for this reason a new custom cryostat was designed, the so-called “cryo-oven” (see Appendix A). The new cryostat has a nominal temperature range of 5-400 K (compared to 3.5-300K of the old β -NQR cryostat). Being able to reach higher temperatures can be critical for studying slow diffusion, since the diffusion rate increases exponentially with temperature in materials that follow Arrhenius’ law. Thus, if the diffusion rate is prohibitively slow in a material at room temperature, one can try to measure it at an elevated temperature.

Using the system described above, the diffusion rate of Li inside the sample is directly related to the time it takes to reach the surface, which in turn relates to the α -rate as a function of time. This method has intrinsic time- and length-scales of $\tau_{1/2} \sim 1$ s and $d \sim 100$ nm, respectively, which leads to a theoretical sensitivity to the diffusion rate D from 10^{-12} to 10^{-8} $\text{cm}^2 \text{s}^{-1}$. This technique thus covers an optimal range of D for battery materials. However, our effective sensitivity limit is closer to 10^{-11} $\text{cm}^2 \text{s}^{-1}$, determined by experimental factors such as the finite acquired statistics and the existence of small distortions from nonlinear detector response.

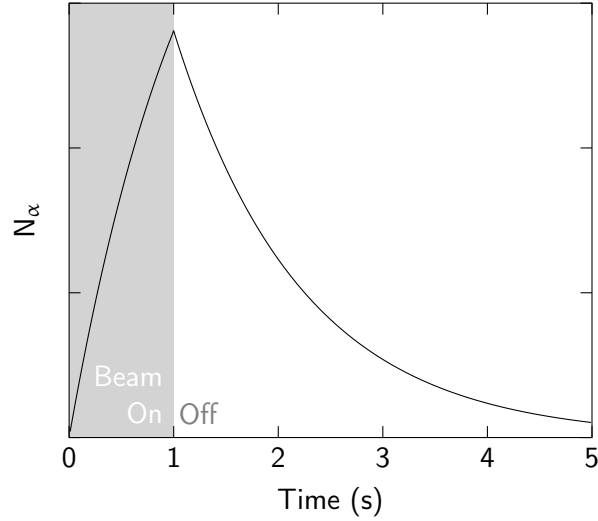


Figure 5.3: Simulated raw counts at the α -detector versus time. There is a sudden change when the beam goes off at 1 s. Prior to that, the number of ${}^8\text{Li}$ ions present at any given moment in the sample was approaching transient equilibrium, whereas after the end of implantation, the remaining ${}^8\text{Li}$ is left to decay away.

In situations where Li^+ is not mobile, the probability of detecting an α is time-independent and the measured α -counts follow the decay rate of ${}^8\text{Li}$ (Fig. 5.3). This can be monitored conveniently using the high energy β -particles from the ${}^8\text{Li}$ decay, which are weakly attenuated over these distances. Thus, the ratio of counts $Y_\alpha = N_\alpha/N_\beta$ is constant in time. On the other hand, when Li^+ is mobile, the ratio is time-dependent when the mean diffusion length in the ${}^8\text{Li}$ lifetime is comparable to the mean depth of implantation, reflecting the fact that the ${}^8\text{Li}^+$ depth distribution (and hence the probability of detecting an α) is evolving in time.

The information on Li diffusion comes from the time evolution of the α -signal. The absolute α -to- β ratio, i.e., the *baseline* ratio of Y_α , in the absence of diffusion, depends on experimental factors such as detector efficiencies, therefore in order to account for these systematics, each α -spectrum is self-normalized to start from unity at time zero, i.e., $Y_\alpha^n(t) = Y_\alpha(t)/Y_\alpha(0)$.

In Sect. 5.2.2, simulated normalized α -signals $Y_\alpha^n(t)$ for several diffusion rates will be presented. By fitting the experimentally acquired normalized α -signal $Y_\alpha^n(t; T)$ at a specific temperature to a library of simulated (or calculated) normalized signals, the diffusion rate of Li at that temperature can be extracted (see Chapt. 6).

A technique similar to the one discussed here has been developed by Jeong et al. [81] for Li^+ diffusion on micrometer and, recently, by Ishiyama et al. [56]

on nanometer length scales; however, the technique reported here differs in a few key ways. In particular, the ^8Li implantation rates accessible at TRIUMF (typically 10^6 - 10^7 $^8\text{Li}^+/\text{s}$) are 1-2 orders of magnitude larger [56], which allows the α -detector to be placed at a grazing angle θ ($\leq 4.4^\circ$ versus $10(1)^\circ$ [78]). This detector configuration significantly decreases the α -counts, but greatly enhances the sensitivity to the near-surface region. Using this development, we were able to perform many α -radiotracer measurements at various temperatures in a limited amount of time, which permitted for the first time the extraction of the Li diffusion activation energy (see Ch. 6).

5.2 Simulations of α -Detected Lithium Diffusion

In this section the aforementioned technique for studying lithium diffusion using the (subsequent) α -decay of ^8Li will be simulated under various conditions. This simulation study is a very important first step towards the realization of the ^8Li α -radiotracer method, because it can provide valuable information on choosing the best possible experimental configuration (e.g., the geometric characteristics of the α -detector, its width, positioning etc), on how to avoid possible pitfalls (such as a high degree of β -contamination in the α -detector) and also how the normalized α -signal $Y_\alpha^n(t)$ changes under various diffusion conditions (faster or slower diffusion rate, different boundary conditions at the sample surface). In all the simulations presented in this Chapter, the sample material is TiO_2 , because this material was selected as the first case to be studying experimentally (see Ch. 6).

In order to extract the Li diffusion rate with the α -radiotracer method, we performed numerical solutions to Fick's laws in 1D to generate the time-evolved depth distribution of $^8\text{Li}^+$, accounting for the boundary conditions of the crystal surface and the initial $^8\text{Li}^+$ stopping profile as simulated by the SRIM Monte Carlo package [104]. The normalized α -signal $Y_\alpha^n(t; D)$ is then obtained using Monte Carlo techniques aided by the Geant4 codebase [125, 135, 136]. The procedure is summarized as follows:

1. The implantation profile of the $^8\text{Li}^+$ beam for an energy E between 0.1 keV to 30 keV for a rutile TiO_2 target is generated using the SRIM Monte Carlo package [104].
2. A custom code was used to diffusively evolve the initial implantation profile with time for various diffusion constants that span five orders of magnitude ($10^{-7} \text{ cm}^2 \text{ s}^{-1}$ to $10^{-12} \text{ cm}^2 \text{ s}^{-1}$) using Fick's law (see Sect. 4.1.1). Two different boundary conditions were considered, namely Li^+ trapped (with a certain probability) or reflected at the surface of the sample.

3. Finally, these temporally evolved profiles of the ${}^8\text{Li}^+$ depth distribution were imported into the Geant4 simulation package. Using Geant4, all the relevant geometrical structures (sample material, detectors, etc), physical interactions (EM, radioactive decays, etc) as well as the energy/momentum distributions of the α - and β -particles were defined and the α -counts versus time at the α -detector were generated.

5.2.1 Temporal Evolution of the Diffusion Profiles

The first part of this simulation study is to generate the beam implantation profiles of the ${}^8\text{Li}$ beam for given beam energies inside the sample (see Fig. 2.11). This is done with SRIM, as discussed at Sect. 2.2.3.

Generally speaking, by increasing the energy of the beam, the mean depth of the ions increases, as does the width of their spatial distribution (i.e., the ion struggle). Different beam energies might be ideal for studying different scenarios, therefore a careful analysis of the optimum beam energy prior to the actual experiment is very important. If the diffusion is very slow, close to the detection limit, it is advantageous to decrease the energy of the lithium beam in order to bring most of ${}^8\text{Li}$ closer to the surface. On the other hand, if the diffusion is very fast, a narrow distribution of lithium close to the surface could lead to most of the change in the α -detected signal happening at the very early times after the beam implantation, possibly lying outside our detection capabilities. In such a case, a higher beam energy would be necessary.

The next step after simulating the beam implantation profile is to study its time evolution due to lithium diffusion. Only diffusion on the axis of implantation (defined here as the z-axis) is considered, because our detection scheme is sensitive only to changes in the depth distribution of lithium.

To observe any effect on the α -detection probability due to diffusion in the xy-plane, the lithium ions would have to be able to reach the edge of the sample in the time scale of a few half-lives of ${}^8\text{Li}$ (~ 6 s). The required diffusion rate for this to happen would be six or seven orders of magnitude larger than a typical diffusion rate of a Li-ion battery material at room temperature. Such an effect is therefore neglected and the xy-distribution of lithium in the sample is considered constant, defined by the properties of the beam. Typically a beam spot of 1 mm to 3 mm diameter is considered, having a Gaussian density distribution. This requirement is realized in the experimental configuration by adding a blocking Al mask in front of the sample, as discussed in Sect. 5.1.

To generate the temporally-evolved depth distribution of the Li ions after a small time interval Δt , the initial implantation spectra are split in infinitesimal bins Δz (1 nm wide) and then each bin is let to diffuse independently using the one

dimensional bulk diffusion equation (Fick's second law):

$$c(z, t) = \frac{c(z', 0)}{2\sqrt{\pi Dt}} \exp\left[-\frac{(z - z')^2}{4Dt}\right], \quad (5.1)$$

where D is the diffusion rate and $c(z, t)$ is the concentration of Li at depth z and time t , due to the diffusion of the initial concentration of the bin at z' . The diffusion length L traveled by a ${}^8\text{Li}^+$ in time Δt is:

$$L = \sqrt{2D\Delta t}. \quad (5.2)$$

The new depth distribution after time Δt is given by superimposing all the point-sources by summing over the diffused profiles of each bin:

$$c(z, t + \Delta t) = \int_0^\infty \frac{c(z', t)}{\sqrt{\pi D\Delta t}} \exp\left[-\frac{(z - z')^2}{4D\Delta t}\right] dz'. \quad (5.3)$$

Where $c(z, t + \Delta t)$ is the new concentration of lithium at depth z , D is the diffusion rate and $c(z', t)$ is the previous concentration of lithium at depth z' .

Apart from the non-zero width of the initial depth distribution, a second complication arises from the fact that not all ions are implanted simultaneously, but rather over some time period $[0, \Delta]$, where Δ is typically set to 1 s. During that time, the initial depth distribution of Li is continuously replenished from the incoming beam. For $t > \Delta$, the beam implantation comes to an end the remaining ${}^8\text{Li}$ are left to diffuse and decay. The algorithm employed here accounts for both the initial depth distribution and the non-zero beam implantation period to calculate numerically the temporal evolution of the depth profiles.

In addition to the aforementioned bulk-diffusion considerations, one has to impose some boundary conditions at the two surfaces of the target crystal. Since at the surfaces of different materials Li ions might interact with different potentials (e.g., potential wells or barriers), two cases of boundary conditions were studied, corresponding to the cases presented at Sect. 4.2.2.

In this section, only the effect of the front sample surface will be presented. This is by far the most important surface, since virtually all of the α -signal comes from decays happening close to it. Also, for typical samples with a thickness of ~ 0.1 mm to 1 mm (see Sect. 6.3), this is the only relevant surface, because the lithium ions won't have time to reach the back of the crystal in a few lifetimes of ${}^8\text{Li}$.

The first boundary condition to be considered is for Li ions to be reflected at the (front) surface of the target. This is probably the most common case in materials that contain Li in their crystal structure; the reason being that all the trap sites for Li ions are occupied. The time-evolved distributions of Li ions for different diffusion constants were calculated, using as a starting point the implantation profile for a

beam implantation energy of 25 keV (Fig. 5.4). The acquired temporally-evolved spectra for a diffusion constant of $D = 10^{-10} \text{ cm}^2/\text{s}$ are presented at Fig. 5.4.

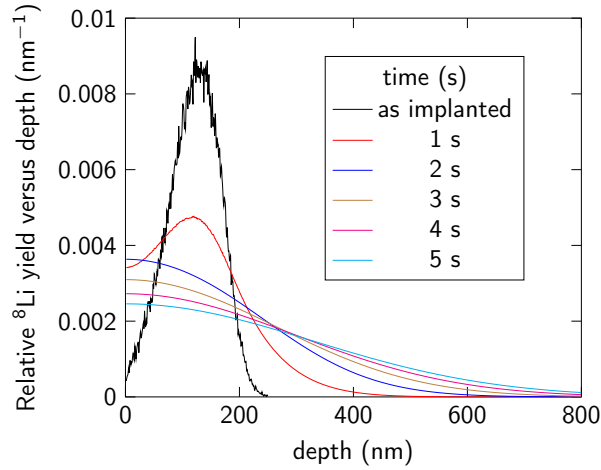


Figure 5.4: Calculated depth profiles of Li ions versus time (using Eq. 5.3) for a beam pulse of 1 s in TiO_2 , diffusion constant $D = 10^{-10} \text{ cm}^2 \text{ s}^{-1}$, a beam energy of 25 keV and with Li ions getting reflected at the surface of the material.

It is evident that the depth profile of the ^8Li concentration is relatively narrow upon implantation, but it broadens significantly after a few seconds. For faster diffusion rates of $10^{-9} \text{ cm}^2 \text{ s}^{-1}$ to $10^{-8} \text{ cm}^2 \text{ s}^{-1}$, the ^8Li ions will get distributed over a wide depth range of several μm after a few seconds.

The second boundary condition we consider is that Li ions get trapped (with 100% probability) when reaching the front surface of the sample. This leads to an increasing percentage of Li at the surface over time. The percentage of Li trapped at the front surface of the sample versus time for various diffusion rates is depicted at Fig. 5.5:

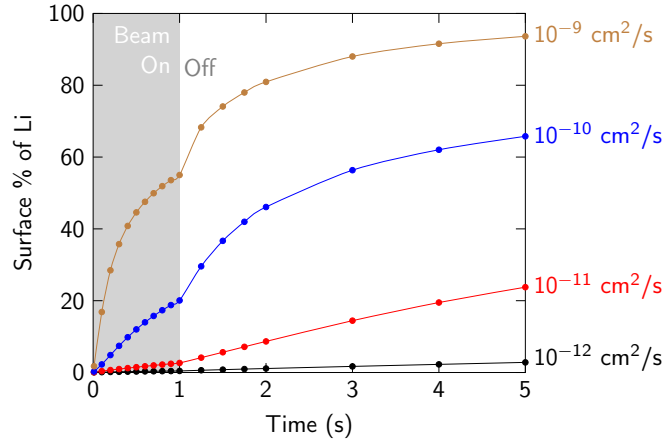


Figure 5.5: Simulated fraction of Li ions trapped at the front surface of a TiO_2 sample versus time, for a beam pulse of 1 s and an initial beam energy of 25 keV.

From Fig. 5.5, it is evident that for a fast diffusion constant of $10^{-9} \text{ cm}^2 \text{ s}^{-1}$, more than 80 % of the remaining Li is trapped at the front surface of the sample after 5 s. Of course Li diffuses in both directions through a random walk, but because it gets trapped at the surface most of it will end up there, after a few lifetimes. For slower diffusion constants these effects get gradually smaller. For diffusion constants in the order of $10^{-12} \text{ cm}^2 \text{ s}^{-1}$, virtually no Li ions will have reached the surface after 5 s. The accumulation of Li at the surface for diffusion rates $>10^{-10} \text{ cm}^2 \text{ s}^{-1}$ approaches saturation after a few Li lifetimes, while slower diffusion rates result in a more linear accumulation. To study slower diffusion rates $10^{-12} \text{ cm}^2/\text{s}$ to $10^{-11} \text{ cm}^2/\text{s}$, one could decrease the energy of the beam, in order to move the distribution closer to the front surface.

Having generated the depth profiles of Li ions as functions of time, diffusion constants and boundary conditions, the next step is to import them into the Geant4 simulation, in order to study the detector response at each scenario (i.e., time, D , E_{beam}).

5.2.2 Geant4 Simulations

Geant4 is a well established software toolkit used for the simulation of particle-material interactions [125], such as the passage of particles through matter, detector response to particle beams, etc. Geant4 is based structurally on the computer language C++ and utilizes a Monte Carlo algorithm and a random number engine. It is designed for use in a very wide range of applications, spanning from high energy and accelerator physics, to nuclear physics, space applications, as well as medical

physics and radiation safety. Indeed, it is applicable in an energy range of meV (such as ion-DNA interactions [137]) to TeV (LHC-related applications).

Geant4 offers an extended toolkit covering all aspects of a particle-detector simulation. By using many predefined libraries and functionalities, the user can define the geometry of the simulation (materials, shapes, dimensions, relative positions, static EM fields), can choose from a number of physical models that determine the processes relevant to the project (including electromagnetic and hadronic interactions, decays etc.), the type, energy and the momentum (distributions) of the primary beam particles, the shape and position of the beam. The user can also define the desired output type at the end of the simulation process, such as the energy deposited in the detector, the number of particles reaching the detector, etc.

Because of its object-oriented and modular architecture, the user is free to choose, load or customize only the tools needed for their specific project. This allows for a comprehensive structure that promotes the understanding of the code, lying far away from black-box-type simulations. In addition, its multi-threading capabilities allow for a nearly linear scale up of the number of simulated events [136].

The code of this simulation study is intended to be very adaptive to different scenarios, therefore the user is allowed to define most aspects of it (using a macro file or the command prompt) at the beginning of each simulation. This way, the user can choose the energy of the ^8Li beam (that corresponds to a SRIM implantation profile to be loaded, see Sect. 5.2.1, the position and size of the (Gaussian) beamspot, the sample's (and substrate's, if applicable) material and dimensions, the lithium diffusion rate that will be simulated, as well as the size, width and depth of the α -detector around the sample. The physical processes and the energy distributions of the decay products of ^8Li are defined internally, so the user would have to re-compile the code, if any changes are needed on these aspects. More details on the structure of this Geant4 project can be found in Appendix B.

The α -detector response is simulated for every required point in time the following way: First, the depth profile of ^8Li is calculated for that time-bin, using the algorithm outlined in Sect. 5.2.1. The user defines how many Monte Carlo events (i.e., simulated ^8Li decays) are required per time-bin. These decays are generated at a random depth that follows the aforementioned depth distribution and their decay product energies (one β , two α and one antineutrino) following the distributions of Fig. 2.2. The initial direction of each particle is random, except for the two α -particles that are emitted always back-to-back due to momentum conservation. Note that the parity violation of the β -decay is not implemented and is neglected as irrelevant to this study.

Each decay product is tracked individually through the geometry of the simulation. At each step of their trajectory all relevant physical processes are taken into consideration and they ultimately define stochastically the new position, direction

and momentum of that particle's trajectory. As a result, both α - and β -particles scatter and lose energy while inside the sample, but over very different length scales, as explained in Sect. 5.1. Part of their energy loss can be transformed into secondary particles (such as low energy photons or electrons) that are also tracked in turn. Any particle that reaches the detector(s) will interact with it and deposit energy. When the total energy deposited in the detector is above a user-defined threshold, then Geant4 registers a count in that detector. Note that all energy deposited is measured, which means that if there is a lot of contamination from other particle species, the detector signal could be potentially swamped. The issue of a possible β -contamination at the α -detector is studied in Sect. 5.2.2.4.

5.2.2.1 Physical processes

In this simulation study, the main relevant physical processes are the electromagnetic interactions and the radioactive decays. Since the energies of all particles that participate in this experiment are not higher than a few MeV, many high energy nuclear processes are forbidden (e.g., pair productions). The only nuclear process (other than β -decay and α -decay) that can in principle be present is low energy elastic nuclear scattering. Note that Geant4 automatically selects only the relevant processes in each scenario based on the energy and type of particles. For instance, if the hadronic interactions are "turned on" in a simulation concerning only leptons, they will have no effect at all.

Because of the vast energy interval of possible Geant4 applications (meV-TeV), there are multiple libraries (called PhysicsLists) that the user can select to simulate the electromagnetic and nuclear interactions with different degrees of accuracy based on the energy scale [138]. Some of them focus on enhanced accuracy and others on better CPU performance. In this study, the PhysicsLists used were selected based only on accuracy considerations. This is because the simulation time-investment scales very rapidly with energy, so in this "low energy" range it is still rather small.

For electromagnetic interactions, the library *G4EmLivermorePhysics* was selected, because it is more accurate than the usual *G4EmStandardPhysics* in the MeV energy range. The hadronic interactions were included by importing the libraries *G4HadronElasticPhysics* and *G4HadronPhysicsQGSP_BERT*, which use the Bertini model as a basis of simulating hadronic interactions. The various aspects of ion nuclear decay physics were covered by importing the relevant libraries (*G4DecayPhysics*, *G4RadioactivePhysics*, *G4StoppingPhysics*, *G4IonPhysics*).

Note that Geant4 failed to generate the energy distribution of the α -particles of Fig. 2.2b, because the quantum mechanical mixing of the two first excited states of ^8Be was not implemented. To solve this issue that was leading to an unphysically narrow energy spectrum for the α -particles, the energy distribution of Fig. 2.2b was

imported by hand. All other aspects of the simulation, such as the energy spectrum of the β and neutrino particles, the momentum distributions etc., were verified to be simulated correctly by Geant4.

5.2.2.2 Geometry

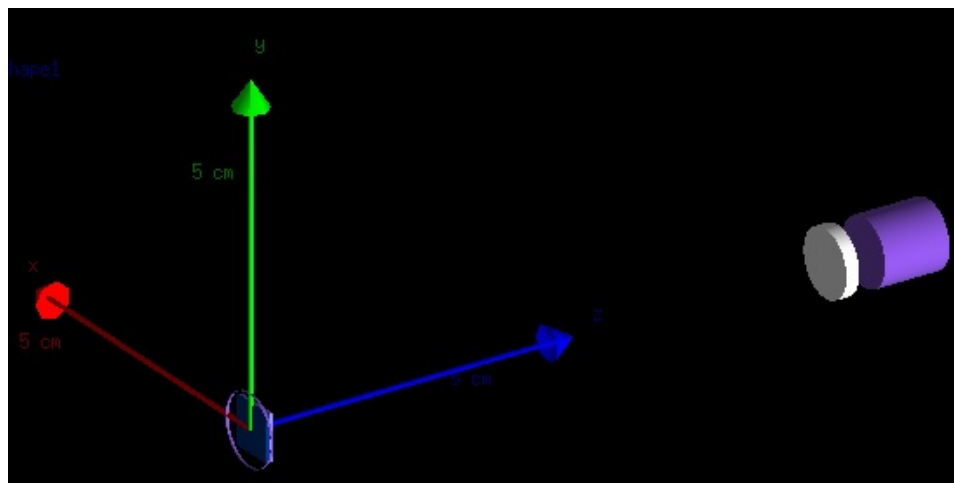


Figure 5.6: Geometry simulated by Geant4. It contains a sample (optionally on a substrate) at the center of the coordinate axes, with the ring α -detector around its beam-facing surface, plus a β -detector behind a collimator at the back side of the sample, used for calibration and testing purposes. The collimator is placed to simulate the stainless steel foil in front of the β -NMR β -detectors that blocks all alphas while allowing the beta particles to reach the detectors without much attenuation.

The geometry of the simulation study can be seen at Fig. 5.6. It is comprised of four different parts:

1. The sample under study (the light blue square at the center of the coordinate system). The user can define its size, thickness and material.
2. At the back side of the sample there can optionally be a substrate. The user is free to define its properties as well, but by default it is made of vacuum (i.e., it does not exist).
3. Around the front surface of the sample, there is a thin scintillating ring (made by default of ZnS(Ag)) for α -detection. This ring is placed in front of the

sample, in the sense that the ending point of the ring parallel to the z-axis is at the same plane with the surface of the sample. The ring has a default width of 10.4 mm diameter, a width of 0.4 mm and a depth of 0.1 mm. It is angled internally to match the specifications of the actual experimental detector. The fact that its depth is very small, makes it sensitive selectively to α -particles, which deposit all their energy very rapidly, while making it completely insensitive to β -particles (see Sect. 5.2.2.4). As with most other aspects of this geometry, the user is free to modify the characteristics of the α -detector.

4. A second detector is placed at a distance behind the sample, lying behind a thin stainless steel collimator, which blocks all α -particles from reaching this β -detector. It is used to normalize the α -detector counts, but its purpose is purely for calibration and testing.

5.2.2.3 α -detector signal

The distribution of the energy deposited at the α -detector at different points in time is depicted at Fig. 5.7, as simulated by Geant4 for a diffusion rate $D = 10^{-9} \text{ cm}^2 \text{ s}^{-1}$ and the two aforementioned boundary conditions at the sample's surface. Note that this is the total energy deposited in the α -detector, by all incoming particles (i.e., α -particles, β -particles and secondary photons and electrons produced by the primary decay products of ^8Li).

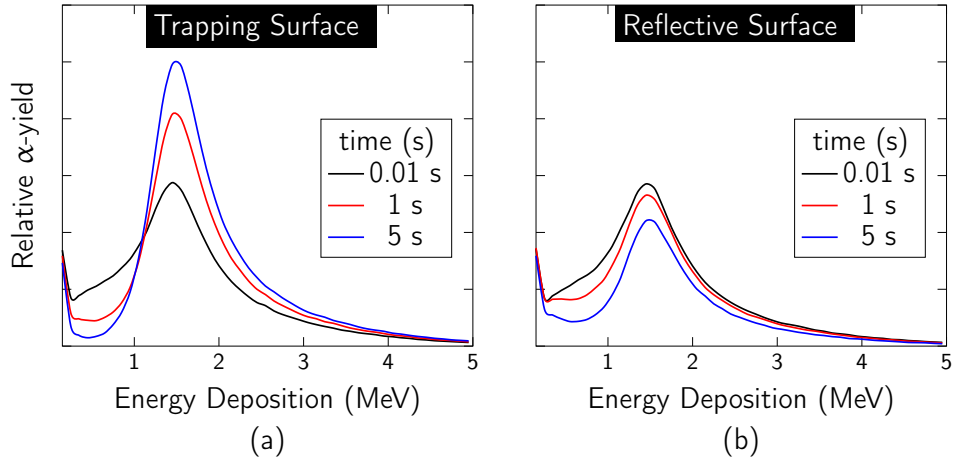


Figure 5.7: Simulation of the distribution of energy deposited at the α -detector per decaying ${}^8\text{Li}$ ion at different times for a ${}^8\text{Li}$ beam energy of 25 keV, with ${}^8\text{Li}$ diffusing with a diffusion rate $D = 10^{-9} \text{ cm}^2 \text{ s}^{-1}$ and Li ions getting trapped (*Left*) or reflected (*Right*) at the sample's surface. In the trapping case, there is a significant increase with time in α -yield at high energies, as an ever increasing percentage of Li^+ gets trapped at the surface and can therefore reach the detector without attenuation, accompanied by a decrease in yield at the low-energy part of the spectrum, as the percentage of Li^+ deep into the sample decreases accordingly. The situation is the opposite for the reflective case.

When ${}^8\text{Li}$ gets trapped at the sample surface (Fig. 5.7(a)), the yield of high energy ($>1.5 \text{ MeV}$) α -counts increases with time, because most of the ${}^8\text{Li}$ will reach the surface after a few lifetimes and will get trapped. The situation is more complicated when Li gets reflected at the surface (Fig. 5.7(b)), because the ${}^8\text{Li}$ ions will initially diffuse (and) towards the surface, but then the distribution will start diffusing primarily towards the bulk of the sample.

In order to suppress the background, namely the part of the signal that has no connection or dependence on lithium diffusion, an energy threshold has been set at 2 MeV. As a result, the α -detector registers a count if at some time (interval) the total energy deposited in the detector is at least 2 MeV. This threshold has been selected in order to maximize the signal-to-background ratio of the detector, while maintaining significant count rates, since it allows to measure $\sim 30\%$ of the unattenuated α -particles. A larger threshold value would reduce the counts of the detector, without any significant effect on the quality of the signal. On the other hand, a smaller threshold gradually decreases the quality of the signal (see Fig 5.8).

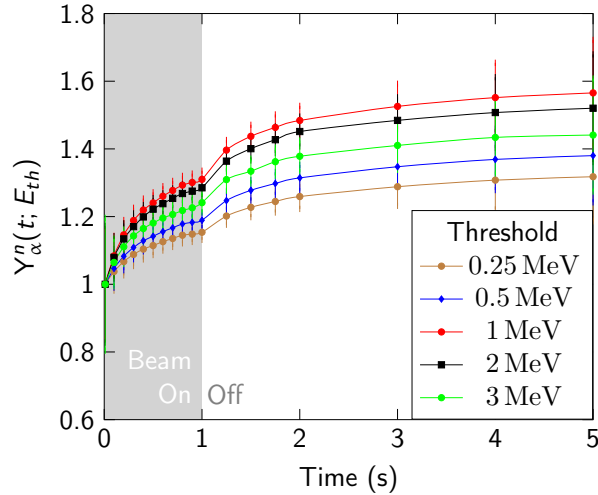


Figure 5.8: The normalized α -spectrum, as simulated with Geant4 in TiO_2 , for different α -detector thresholds, a beam pulse of 1 s, diffusion constant $D=10^{-9} \text{ cm}^2/\text{s}$ and an initial beam energy of 25 keV, using the accumulative boundary condition. Each simulated point is generated by 10^7 ${}^8\text{Li}$ decays. Evidently, the energy threshold does not affect the temporal evolution of the Y_α^n signal, but rather different detector thresholds can enhance or suppress the amplitude of Y_α^n . The error bars are suggestive of what they would be in an actual experiment, based on the statistical \sqrt{N} factor. They are the smallest at the beam off time ($t = 1$ sec), when the number of ${}^8\text{Li}^+$ decays is at maximum (see Fig. 5.3) and they increase substantially after that.

Even though the qualitative characteristics of the normalized α -signal (e.g., the rate of reaching saturation) are unaffected by varying the energy threshold of the α -detector, a threshold between 1 MeV to 2 MeV results into the greatest percentage change of the normalized α -counts with time and thus to the clearest α -signal.

With those considerations in mind, the normalized α -signal with an α -energy threshold of 2 MeV is plotted in Fig. 5.9 as a function of time for lithium trapping at the surface of the sample material:

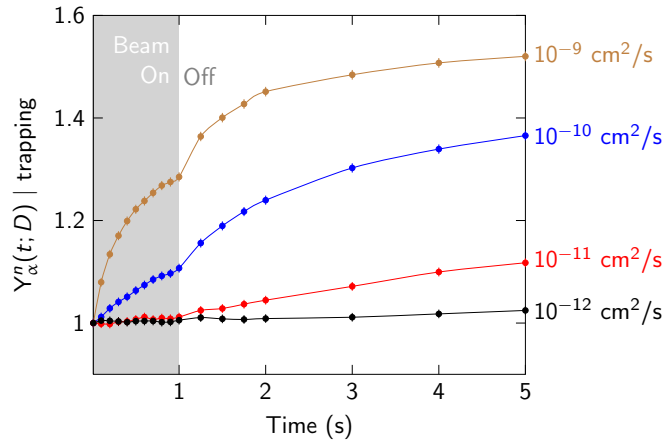


Figure 5.9: The normalized α -signal, as simulated with Geant4 in TiO_2 , for a beam pulse of 1 s, different diffusion rates and an initial beam energy of 25 keV, using the accumulative boundary condition. Each simulated point is generated by 10^7 ^8Li decays.

Comparing Fig. 5.5 and Fig. 5.9, it is clear that the simulated spectrum looks qualitatively very similar to the time evolution of the percentage of ^8Li decaying near the surface. There is a ‘kink’ at $t = 1\text{s}$, when the beam pulse is switched off. Before that time, the initial beam profile gets continuously replenished by the beam, antagonizing the fast lithium diffusion. After the beam is switched off, lithium diffuses in both directions, but because it gets trapped at the surface most of it will end up there, after a few lifetimes (see Fig. 5.5). For fast diffusion (e.g., $D > 10^{-10} \text{ cm}^2/\text{s}$) this leads to a saturation of the signal for $t > 3\text{s}$. For a slower diffusion rate ($D < 10^{-10} \text{ cm}^2/\text{s}$) the saturation regime is out of the range of a few lithium lifetimes, so the signal increases much more linearly and never really saturates. The situation is very different when lithium gets reflected at the surface of the sample (Fig. 5.10).

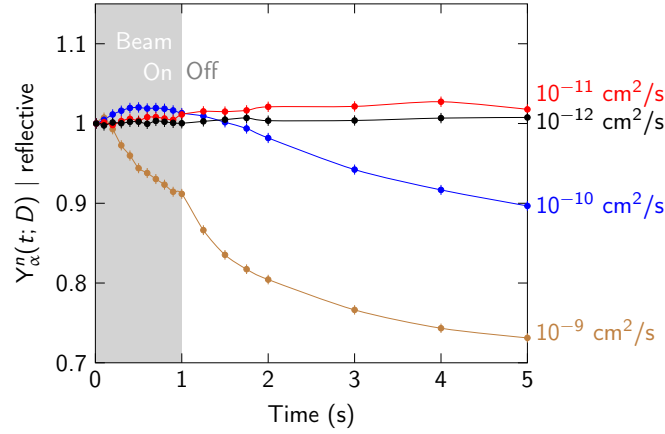


Figure 5.10: The normalized α -signal, as simulated with Geant4 in TiO_2 , for a beam pulse of 1 s, different diffusion rates and an initial beam energy of 25 keV, using the reflecting boundary condition. Each simulated point is generated by 10^7 ^8Li decays.

This boundary condition leads to a more complicated dependence of the α -signal on the diffusion rate. If the diffusion rate is lower than $10^{-11} \text{ cm}^2/\text{s}$, then the Li haven't had time to reach the surface of the sample after 5 s, so the α -signal increases very similarly to Fig. 5.9. For $D = 10^{-10} \text{ cm}^2/\text{s}$, the signal initially increases, as the peak of the ^8Li distribution moves towards the surface, but decreases rapidly at later times, after most of ^8Li has bounced on the surface and moves towards the bulk. If the diffusion rate is faster than $10^{-9} \text{ cm}^2/\text{s}$, then the initial upturn will end almost instantaneously and the α -signal will be monotonically decreasing.

A comparison between Fig. 5.9 and Fig. 5.10 indicates that the simulated α -signal is very different depending on what happens to Li when it reaches the sample surface. Therefore, if the boundary condition for Li reaching the surface of a material is not known *a priori*, it can be deduced by comparing the experimentally acquired α -signal with Fig. 5.9 and Fig. 5.10.

In the general case, where there is a trapping probability P_{tr} between 0 – 1 for $^8\text{Li}^+$ to get trapped at the surface, then for the same diffusion constant the α -signal $Y_\alpha^n(t)$ evolves from its shape with a reflective boundary condition towards its shape with a fully trapping surface, when P_{tr} gradually increases to 1. This is depicted in Fig. 5.11 for a diffusion rate $D = 10^{-9} \text{ cm}^2/\text{s}$.

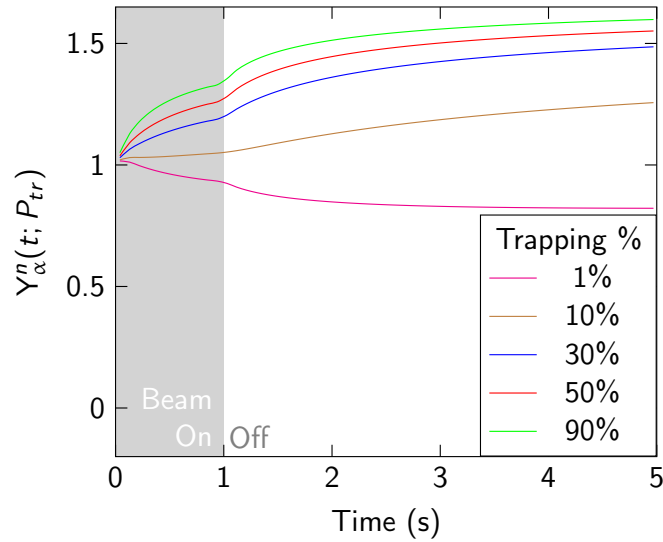


Figure 5.11: The normalized α -signal, for a beam pulse of 1 s, a diffusion constant $D = 10^{-9} \text{ cm}^2/\text{s}$ and an initial beam energy of 25 keV, using various trapping probabilities at the surface of the sample.

Regardless of the nature of the boundary condition at the surface, the α -signal gets increasingly further away from the simple exponential decay of ${}^8\text{Li}$ with increasing diffusion rate. With an accumulating boundary condition ($P_{tr} \sim 1$), faster diffusion results in increasing α -to- β ratio, while a reflecting boundary condition ($P_{tr} \sim 0$) leads to α -counts that decrease with time faster than a simple exponential, as Li bounces off the surface and starts diffusing towards the bulk of the sample.

In both cases, a diffusion constant larger than $10^{-12} \text{ cm}^2/\text{s}$ results in an observable variation from the simple exponential decay line – which is the flat line at the $Y_{\alpha}^n(t)$ spectrum. Studying slower diffusion is possible by decreasing the beam energy and thus moving the lithium closer to the surface (see Fig. 5.12).

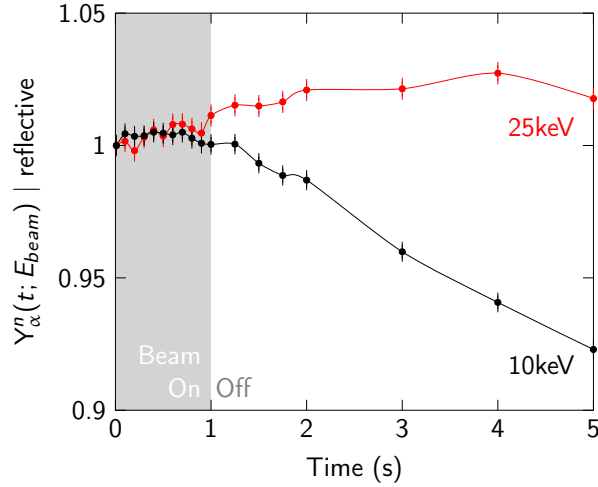


Figure 5.12: Simulated α -signals for a diffusion rate $D = 10^{-11} \text{ cm}^2/\text{s}$ and beam energies of 10 keV and 25 keV, using the fully reflecting boundary condition. Each simulated point is generated by 10^7 ^8Li decays. The (black and red) lines are just guides for the eye.

From the above figure, it is evident that changing the energy of the beam can have a significant effect on the quality of the $Y_\alpha^n(t)$ α -signal. For a beam energy of 25 keV, the signal for a diffusion rate $D = 10^{-11} \text{ cm}^2/\text{s}$ changes by less than 1 % over a period of 5 s, making the measurements of such an effect very time consuming and marginal. On the other hand, reducing the beam energy to 10 keV results into a signal that changes by ~ 10 % over the same time period, thus allowing for an easier measurement of slow diffusion.

5.2.2.4 β -contamination

Since the β -particles are insensitive to nanoscale Li diffusion, having a lot of energy deposited by β -particles inside the α -detector could result to a diffusion-independent background in the α -detector signal, which potentially could swamp the actual α -signal.

For this reason, the thickness of the α -detector has to be as thin as possible in order to minimize the contamination from β -particles, while being thick enough to stop the α -particles completely. Fig. 5.13 shows how much energy gets deposited by α - and β -particles inside the α -detector – made of ZnS(Ag) – for various detector thicknesses of the order of 0.01 mm to 1 mm.

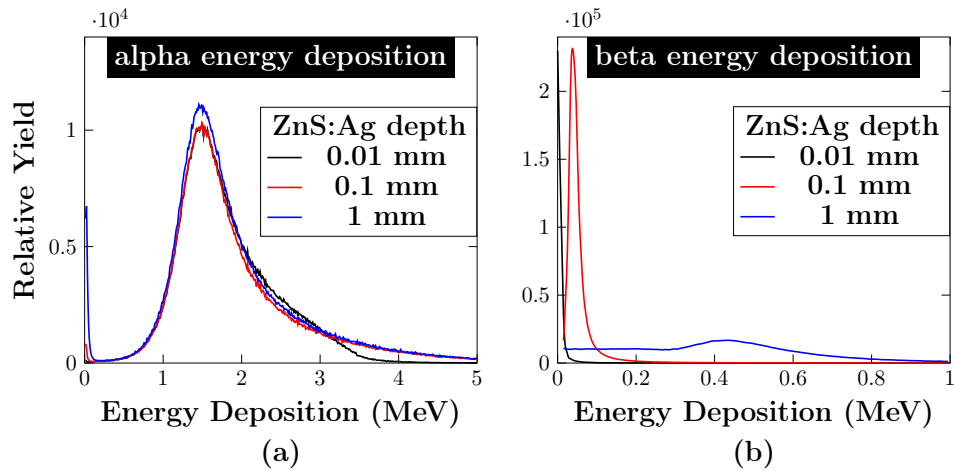


Figure 5.13: The energy deposition profile of α - (*Left*) and β -particles (*Right*) inside the α -detector for various detector thicknesses.

From Fig. 5.13(a) one can see that an α -detector thickness in the range 0.1 mm to 1 mm is adequate to stop completely the α -particles, while a detector thickness of 0.01 mm is not enough to completely stop the α -particles with energy >4 MeV.

Turning to Fig. 5.13(b), the energy deposited in the α -detector by the β -particles is virtually zero for a detector thickness of 0.01 mm, while for a thickness of 0.1 mm, it is still limited around 100 keV. For larger detector thickness, in the order of 1 mm, the β -particles can deposit as much as 1 MeV in the α -detector, which could lead to background.

The above considerations identify an α -detector thickness of 0.1 mm as the optimum value if the detector is made of ZnS. If another material is used, then this study has to be repeated, since different material densities and Z -values result in different stopping profiles for the incoming α - and β -particles.

5.3 Calculating the α -radiotracer signal

A major limitation of the simulation study presented in the previous section is the time investment required for the simulation of a given scenario. This is true even after complete parallelization of the Geant4 code, which provides almost linear scale up with the number of processors [136].

Computationally speaking, each such simulation can be divided into two parts: The calculation of the ^8Li depth profile versus time and the Monte Carlo simulation for every given point in time.

The time needed for the first part increases exponentially with the diffusion rate D . For slow diffusion rates (D between 10^{-12} cm²/s to 10^{-11} cm²/s), all ⁸Li ions are distributed in the first few hundred nanometers from the surface, but for faster diffusion (D between 10^{-9} cm²/s to 10^{-8} cm²/s), the depth profile of ⁸Li spans over tens of micrometers after a few seconds. Consequently, calculating the depth profiles of ⁸Li for slow diffusion is almost instantaneous, but can take up to several hours for fast diffusion (using a machine deploying an Intel(R) Core(TM) i7-4710HQ processor, CPU @ 2.50GHz, 4 Core(s), 8 Logical Processor(s)).

In addition to the time consuming calculation of the depth distributions, running the Geant4 simulation typically takes a few hours to complete a crude time-scan of 15-20 data points with 10^7 Monte Carlo statistics per point. This raises the total time investment significantly. For example, if a fine grid of data points is used over a period of, e.g., 5 s after the beam implantation, for a multitude of diffusion rates spanning at least 3-4 orders of magnitude, the required computational time for the Geant4 simulations is prohibitively long.

To amend this problem, a method was developed to bypass the Geant4 simulation completely. The idea is that the result of the Monte Carlo simulation can be calculated (instead of simulated) by multiplying each bin of the depth profile of ⁸Li (such as Fig. 5.4) with the probability of detecting an α for that depth (see Fig 5.14).

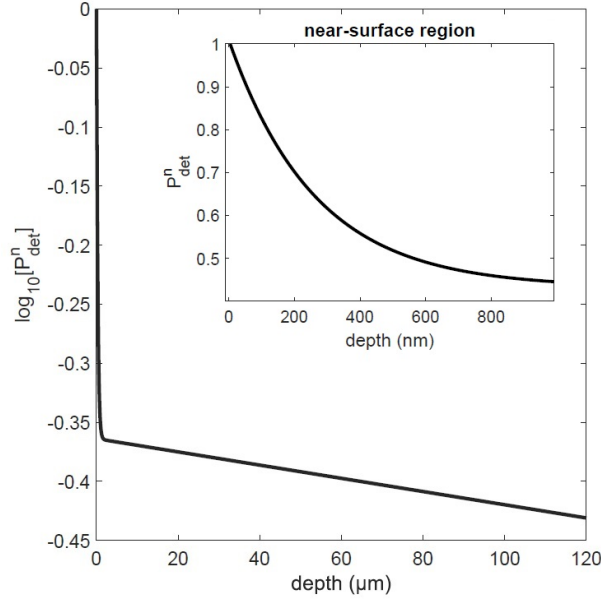


Figure 5.14: Probability of α -detection versus decay depth, as simulated by Geant4 in TiO_2 . P_{det}^n is the probability of detection normalized to 1 at the surface, namely $P_{det}^n(d) = P_{det}(d)/P_{det}(0)$. At the main plot, the logarithm of P_{det}^n is plotted over a range of 120 μm . There is a very sharp decrease over the first 100 nm and a very slow probability reduction after that. For clarity, the first 1 μm from the surface is plotted at the insert, on a linear scale.

For the case of TiO_2 , this distribution can be fitted effectively with a phenomenological sum of two exponentials:

$$P_{det}(z; E_{th}) = c_1 \exp(a_1 z) + c_2 \exp(a_2 z) \quad (5.4)$$

with parameters: $c_1 = 0.01774$, $a_1 = -0.003809 \text{ nm}^{-1}$, $c_2 = 0.0133$ and $a_2 = -1.288 \cdot 10^{-6} \text{ nm}^{-1}$. Evidently, the fast decaying component dies out after the first 500 nm, while the slowly decaying component has a range on the millimeter scale. The fast component is related to the high energy tail of Fig. 2.2b and the fact that the α -detector ring has a non-zero width, whereas the slow component is most probably due to α -particles emitted at a low angle relative to the surface of the sample that reach the detector after they scatter close to the surface. This scattering results in a small $d/\sin\theta$ parameter, with only a weak increase of the attenuation with decay depth.

Note that the probability P_{det} of α -detection is a function of both the decay depth and the energy threshold of the detector, as well as the properties of the

material (density, Z -value, etc), therefore this simulation has to be run once per material under study.

Then, the α -counts versus time are given by:

$$N_{\alpha}(t) = N(t) \int_0^{\infty} C(z,t) P_{det}(z; E_{th}) dz \quad (5.5)$$

where $N(t)$ is the number of α -decays versus time, $C(z,t)$ is the concentration of Li at depth z and time t and $P_{det}(z; E_{th})$ is the probability of detecting an α above a given energy threshold E_{th} at that depth. A comparison between the simulated and calculated α -signals under the same condition can be seen in Fig. 5.15.

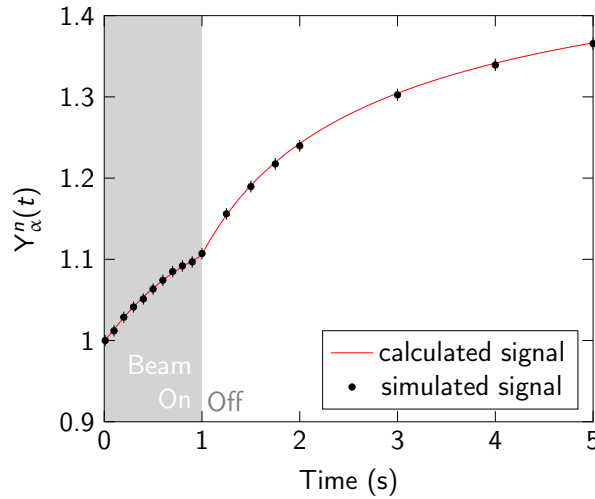


Figure 5.15: Comparison of the calculated (continuous red line) and simulated (black points) $Y_{\alpha}^n(t)$ α -signals for a diffusion rate of $D = 10^{-10} \text{ cm}^2 \text{ s}^{-1}$.

Evidently, this method succeeds in reproducing the Geant4 simulation. The merit of this approach is that it allows for the calculation of normalized α -signals in only a fraction of the time required for the full Geant4 simulation. This development was exploited for extracting the diffusion rate of Li from experimental data (Ch. 6).

5.4 Conclusions

In summary, the subsequent α -decay of ^8Li can be used to extract the nanoscale diffusion rate of Li in solids.

The very different attenuation profiles of the emitted α - and β -particles inside materials allow for the monitoring of the nanoscale $^8\text{Li}^+$ motion towards/away from

the sample surface by measuring the ratio of the α -to- β counts versus time.

A detailed simulation study of the above concept was carried out. The implantation profile of ${}^8\text{Li}^+$ for various beam energies was simulated by SRIM. These profiles were evolved in time for different diffusion coefficients D in accordance with Fick's second law, in order to calculate the ${}^8\text{Li}$ depth distribution versus time under the boundary condition of ${}^8\text{Li}$ getting either trapped (with a certain probability) or reflected upon reaching the sample surface. Then, for each of the above depth distributions, the output of the α - and β -detectors was simulated by Geant4.

By analyzing the various simulations presented in this Chapter, a favorable experimental geometry was identified, which was used as a basis for the design of the new cryo-oven (see Appendix A).

The combined graphs of the normalized α -signals Y_α^n versus time for various diffusion coefficients showed that it is possible to determine the boundary condition at the sample surface based on the time evolution of Y_α^n .

It was also identified that it is possible to accelerate the compilation of a library of normalized $Y_\alpha^n(t; D)$ by performing a series of calculations that are able to reproduce the Geant4 simulations in a fraction of the required time.

In the next Chapter, this theoretical/numerical study is put to the test, by performing proof-of-principle ${}^8\text{Li}$ α -radiotracer measurements in rutile TiO_2 .

Chapter 6

Measurements of ^8Li Diffusion in Rutile using α Detection

In this study we employ the α -radiotracer method to extract the diffusion rate of isolated ion-implanted $^8\text{Li}^+$ within ~ 120 nm of the surface of oriented single-crystal rutile TiO_2 , at the dilute limit of Li concentrations. The α -particles from the ^8Li decay provide a sensitive monitor of the distance from the surface and how the depth profile of ^8Li evolves with time. The main findings are that the implanted Li^+ diffuses and traps (with a probability $\geq 50\%$) at the (001) surface. The T -dependence of the diffusivity is described by a bi-Arrhenius expression with activation energies of 0.3341(21) eV above 200 K, whereas at lower temperatures, it has a much smaller barrier of 0.0313(15) eV. The low- T behavior is discussed in the context of the recently reported Li- Ti^{3+} polaron complex [29].

6.1 Rutile - General Characteristics

Many transition-metal oxides are good materials for lithium-ion batteries [139]; their capability of assimilating the extra charge from lithium ions, their open-structures, and relatively low production cost all make them attractive intercalation electrodes. In particular, the TiO_2 polymorphs have garnered significant attention to this end in recent years.

Rutile is the most stable TiO_2 polymorph (Fig 6.1), which crystallizes in a body-centered tetragonal structure made up of two Ti and four O atoms per unit cell [140] (lattice parameters $a = b = 4.59 \text{ \AA}$ and $c = 2.95 \text{ \AA}$). The crystal's macro-structure is comprised of stacked TiO_6 octahedra, which share edges with their neighbors in the c -direction and corners in the basal ab -planes. This fortuitous atomic arrangement gives rise to open channels parallel to its c -axis, providing a 1D pathway for interstitial ion transport. In this sense, rutile is structurally similar to many so-called superionic conductors which also possess crystallographic tunnels that confine the motion of mobile ions.

Regarding the surface properties of rutile, there have been extensive studies of their properties [141–143], but the focus was never on the (001) surface, as it is not

stable [144–146]. Rather, a reduction of the surface Ti atoms' coordination from sixfold to fourfold reduces the energy configuration of the surface. As a result, the (001) surface tends to reconstruct at higher temperatures, which could give rise to trapping centers for Li^+ .

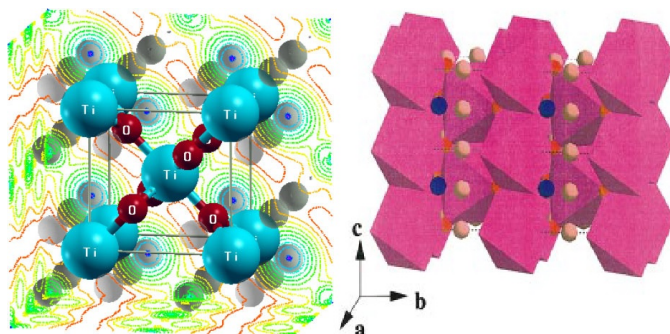


Figure 6.1: A 3-D view of the rutile TiO_2 unit cell [147] (left) and the rutile lattice [148] (right), with the possible sites for lithium intercalation marked with pink (octahedral sites) and blue (tetrahedral sites).

It has been known for some time [60, 70] that Li^+ diffusion down these interstitial channels is extremely fast, greatly surpassing all other interstitial cations [149], with a room temperature diffusion coefficient exceeding many modern solid-state Li electrolytes [150]. A major limitation, however, for the use of rutile as a Li-ion battery material is its limited Li uptake at room temperature [151, 152]; however, the discovery that using nanosized crystallites mitigates this issue [65] has led to renewed interest in its applicability [139].

There are a number of poorly understood aspects of rutile lithiation, including the cause of the limited Li^+ uptake, as well as why reported Li diffusion rates differ by orders of magnitude, even under the same experimental conditions [29, 60, 68, 70–73, 153–155]. As pointed out recently [29], there is large scatter in the reported diffusion coefficients [29, 60, 71–73]. Such systematic discrepancies are not unprecedented (see e.g., LiCoO_2 [74–76]), but rather unexpected in a relatively simple ion conductor.

The 1D ionic transport of Li^+ is characterized by an activation energy of ~ 0.33 eV, as evidenced by both techniques sensitive to microscopic [29, 155] and macroscopic [60, 68] Li^+ motions. Surprisingly, these results greatly contrast the large body of theoretical work that predicts significantly lower barriers of 0.03–0.05 eV [44, 148, 156–163], suggesting a key ingredient is missing from the calculations.

At low temperatures (below 100 K) a second Arrhenius-like component with an

energy barrier of ~ 0.027 eV was recently reported using β -NMR [29], but it was attributed to the local dynamics of Li^+ -polaron complexes, rather than long-range diffusion.

This complex is formed when Li^+ comes into proximity with an electron polaron Ti'_{Ti} , namely a localized electron on a Ti site (i.e., a Ti^{3+} site in a lattice of ideally Ti^{4+}). The electron polaron is mobile along the c -axis stacks of TiO_2 octahedra with an activation energy of 0.033 eV, according to DFT calculations [157].

Interestingly, DFT calculations of the Li-polaron complex hopping, yield an activation energy of 0.29 eV, very close to the value of 0.33 eV found at high- T in all relevant experiments.

Using the results of the current study, we were able to suggest a novel interpretation of the Li^+ dynamics in rutile TiO_2 that can answer some of the above questions.

6.2 Experimental Details

This experiment was performed using the facility infrastructure at TRIUMF [33], in Vancouver, Canada. The α -radiotracer method used a low-energy radioactive ion beam of $^8\text{Li}^+$ to introduce Li into a target material. The ions are implanted with typical energies ≤ 30 keV, whose precise value can be tuned with a decelerating bias applied to an electrically isolated spectrometer platform [33, 123, 164]. The incident energy is used to influence the $^8\text{Li}^+$ stopping distribution, providing depth resolution, with a typical mean range of ~ 100 nm at these energies. The incoming $^8\text{Li}^+$ beam was implanted in rutile targets housed in an ultra high vacuum cold finger cryostat within a dedicated low field spectrometer [33, 123]. The samples were commercial chemo-mechanically polished (roughness < 0.5 nm) single crystal rutile TiO_2 substrates (CRYSTAL GmbH) with typical dimensions of $7 \text{ mm} \times 7 \text{ mm} \times 0.5 \text{ mm}$. The surfaces were free of macroscopic defects under 50x magnification.

6.3 Experimental Results on Rutile TiO_2 Using the α -radiotracer Technique

Using the α -radiotracer technique, we performed measurements on rutile TiO_2 at various temperatures with two beam energies (10 and 25 keV) and two sample orientations.

It is the 1D character of lithium diffusion in rutile TiO_2 (the tensor \mathcal{D} is very anisotropic, see Sect. 4.1.1) that makes it an ideal test case for this technique. As Li^+ is known to diffuse primarily along the c -axis of rutile, if the c -axis is

oriented parallel to the surface (perpendicular to the beam), then the ${}^8\text{Li}^+$ motion should not change the initial implantation profile. Since the ab -plane diffusivity $D_{ab} \ll 10^{-12} \text{ cm}^2 \text{ s}^{-1}$, $Y_{\alpha}^n(t)$ is expected to be time-independent. On the other hand, if the c -axis is perpendicular to the surface, then the depth distribution of lithium should evolve rapidly with time, since $D_c \gg 10^{-12} \text{ cm}^2 \text{ s}^{-1}$. Depending on the boundary condition at the surface, we expect either a spectrum like Fig. 5.9, Fig. 5.10, or something in between.

In Fig. 6.2 we compare the measured normalized α -yield, Y_{α}^n , for the c -axis parallel and perpendicular to the surface. As expected, the time spectrum for the (110) orientation of TiO_2 rutile (c -axis parallel to the surface) is completely flat at 294 K, indicating that the ab -plane diffusion rate is lower than the detection limit $\sim 10^{-12} \text{ cm}^2 \text{ s}^{-1}$ (Fig. 5.9), consistent with other studies reporting an ab -plane diffusion rate of $10^{-15} \text{ cm}^2 \text{ s}^{-1}$ or lower [60].

In contrast, the spectrum from the (001)-oriented crystal increases rapidly with time. Most of the percentage change in the signal happens during the first 2 sec followed by a much more gradual increase. This is the signature of fast diffusion ($D > 10^{-9} \text{ cm}^2/\text{sec}$), approaching the saturation regime of Fig. 5.9.

Next, we rotated the (001)-oriented rutile by $\theta \sim 10^\circ$ – introducing an angle between the incoming beam and the crystallographic c -axis – and repeated the measurement under otherwise identical experimental conditions (294 K, 25 keV). The two $Y_{\alpha}^n(t; \theta)$ signals can be seen Fig. 6.3. The comparison of the two cases can be used to decide whether channeling (see Sect. 2.2.3) can be neglected or not, as the critical angle for channeling in rutile is calculated (using Eq. 2.5) to be 6.9° . Evidently, the two spectra look very similar – inside their experimental uncertainty –, but the signal of the rotated sample evolves more linearly close to the end of the beam pulse, where the number of alphas collected is maximum. This slight difference might be due to the reduction of a (small) pile-up effect at the detector, as the rotation of the sample reduced the effective solid angle of the detector and thus the probability of two light pulses of lower energy than the threshold to arrive at the same time at the PMT tube and be counted as a single alpha of energy above the threshold (similarly to the case discussed in Sect. 3.3.2).

From the above test, we conclude that channeling cannot be very significant under these experimental conditions, therefore the SRIM implantation profile was used to generate a library of calculated normalized α -spectra versus diffusion rate in a range $[10^{-12} - 10^{-8}] \text{ cm}^2/\text{sec}$, as described in Sect. 5.2. Exploiting the fact that the calculated α -signals can be generated significantly faster than the simulated ones, this library contained 100 calculated spectra for each order of magnitude of diffusion coefficient in the above-mentioned range.

After these tests at room temperature, we also performed a temperature scan in the range of 60 K to 370 K with beam energies of 10 keV and 25 keV. In Fig. 6.4 are

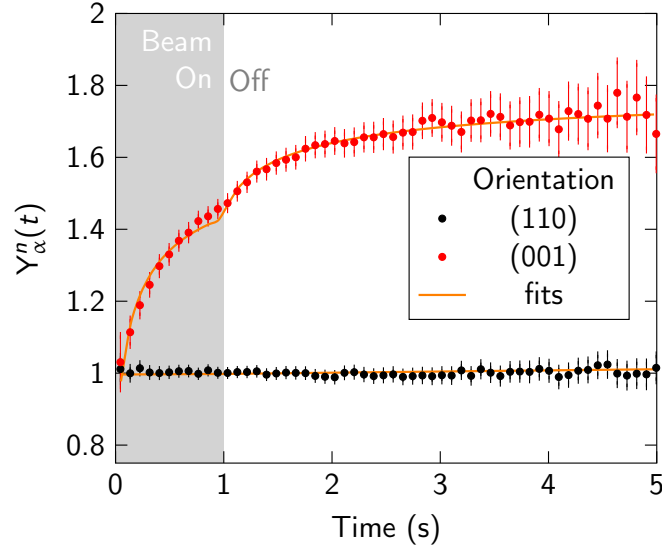


Figure 6.2: Comparison of the measured normalized α -yield $Y_{\alpha}^n(t; D, P_{tr})$ for the (110)- and (001)-oriented rutile TiO_2 and fits (orange lines) for a beam energy of 25 keV and a surface trapping probability $P_{tr} = 1$. The increasing signal with time in the (001) crystal is consistent with the anisotropy of the Li diffusion coefficient [60] and indicates that Li diffuses fast along the c -axis and gets trapped upon reaching the sample surface. Each spectrum took roughly 40 min, with an α -rate of $\sim 20,000$ ions/pulse. Each beam pulse was 1 s long and was repeated every 15 s.

a few examples of experimental data for the (001) orientation with a beam energy of 25 keV, with the corresponding fits.

In this temperature range, the value of the normalized α -signal $Y_{\alpha}^n(t; T)$ at 5 sec increases with temperature up to ~ 300 K, but then evidently starts getting reduced again, even though it is clear that the high temperature spectra reach saturation much earlier. This apparent signal reduction in the high- T region is due to the self-normalization process, which normalizes the spectrum to its (extrapolated) value at time zero. For a beam energy of 25 keV and diffusion rates of up to $\sim 10^{-9}$ cm^2/sec , Li^+ does not move fast enough to reach the surface at the very first time-bins. For faster diffusion, though, this is no longer true. For $D > 10^{-9}$ cm^2/sec , the percentage of Li near the surface (and therefore the probability of α -detection) is much higher even at very early times, so the whole spectrum gets normalized to a higher value, hence the apparent signal suppression.

This effect is also present in the simulations. The turning point in the diffusion coefficient, above which the signal is getting suppressed is 3.1×10^{-9} cm^2/sec in

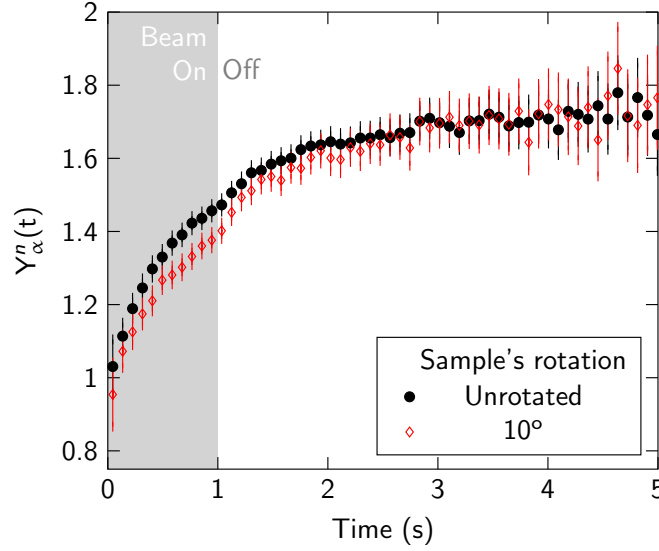


Figure 6.3: Comparison of the measured normalized α -yield $Y_{\alpha}^n(t; \theta)$ between unrotated and rotated (by 10°) (001)-oriented rutile TiO_2 at 294 K.

the current experimental configuration. This is the slowest diffusion rate which enables the peak of the implantation profile of the 25 keV beam of Fig. 2.11 to reach the surface during the first 10 ms time-bin.

To fit the data, we used a custom C++ code applying the MINUIT [165] minimization functionalities of ROOT [166] to compare the Y_{α}^n signals to the library of calculated spectra. The free parameters of the fit were the diffusion rate D and the trapping probability at the (001) surface, P_{tr} . All $Y_{\alpha}^n(t; D, P_{tr})$ spectra at both implantation energies (10 keV and 25 keV) were fitted simultaneously with a shared P_{tr} value. For the (001) orientation Y_{α}^n increases rapidly with time, approaching saturation, indicating that lithium diffuses fast along the c -axis and gets trapped at (or within few nm of) the surface (see Fig. 5.9). For $P_{tr} \geq 50\%$, the global χ^2 value is completely insensitive to P_{tr} , but for $P_{tr} < 50\%$, the quality of the fits deteriorates rapidly. This can be understood by revisiting Fig. 5.11, where it is evident that the Y_{α}^n signal is virtually unaffected by the trapping probability P_{tr} , for $P_{tr} \geq 50\%$.

This is the first *unambiguous* evidence for Li trapping (with at least 50% probability) at the (001) surface. There is no evidence of Li de-trapping up to 370 K, since at that temperature $Y_{\alpha}^n(t; T)$ reaches saturation after ~ 2 s and any Li surface de-trapping would lead to an observable decrease of $Y_{\alpha}^n(t; T)$ at later times. The non-zero trapping probability is most likely related to the reported difficulty of intercalating Li into rutile, as the Li ions would tend to stick at or near the surface

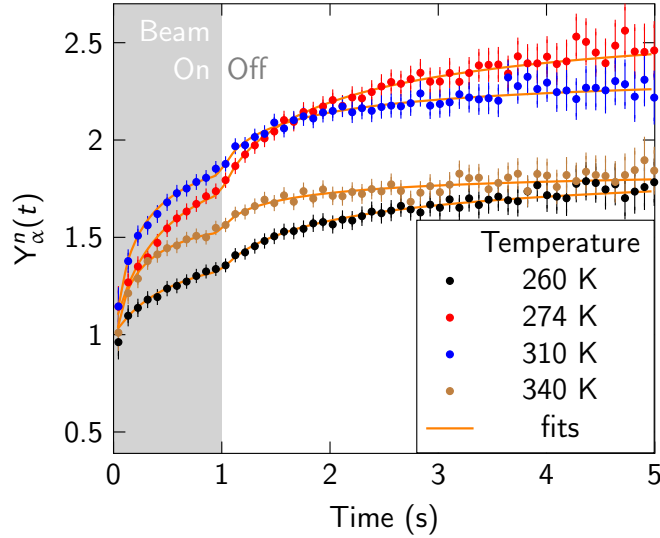


Figure 6.4: Examples of measured normalized α -yield $Y_{\alpha}^n(t; D, P_{tr})$ for the (001)-oriented rutile TiO_2 and fits (orange lines) for a beam energy of 25 keV and a surface trapping probability $P_{tr} = 1$. For increasing temperature, $Y_{\alpha}^n(t; D)$ saturates more and more rapidly, indicating that above room temperature, most of Li gets trapped at the (001)-surface during its lifetime. Above room temperature, the c -axis normalized spectra $Y_{\alpha}^n(t; T)$ get progressively suppressed, as the normalization factor $Y_{\alpha}(t = 0; T)$ increases substantially due to fast diffusion. Each spectrum took roughly 40 min, with an α -rate of $\sim 20,000$ ions/pulse. Each beam pulse was 1 s long and was repeated every 15 s.

rather than diffuse towards the bulk.

This view is in agreement with the suggestion of Hu et al. [65] that there might be a surface storage mechanism for Li^+ in nanosized rutile, with a calculated surface Li content of roughly 50% of its maximum surface capacity in storing Li^+ . In addition, Zhukovskii et al. [167] indicated using ab initio simulations that it might be energetically favorable to store Li^+ at the surface of metal/ Li_2O nanocomposites. It is worth mentioning, however, that both these studies were focusing on nanometer-sized systems, whereas the current study used macroscopic single-crystals, with Li implanted near a (001)-oriented surface.

It is not clear whether the Li^+ surface trapping is caused by an electrostatic potential well (similar to H in Pd [168]), a partially reconstructed surface [141] (see Sect. 6.1), or by a chemical sink due to a solid state reaction at the surface (e.g., forming another phase such as cubic LiTiO_2). With X-ray diffraction, it was found

that about 40 % of the (001) surface of a polished and annealed rutile sample was flat and the remaining 60 % consisted of (011)-oriented facets [169], which could provide trapping centers for Li^+ .

6.4 Arrhenius Fits and Discussion

Turning to the values of $D(T)$ extracted using the above analysis (see Fig. 6.5), they reveal a bi-Arrhenius relationship of the form:

$$D(T) = D_H \exp[-E_H/(k_B T)] + D_L \exp[-E_L/(k_B T)], \quad (6.1)$$

where E_i is the activation energy and D_i is the pre-factor of each component ($i = H/L$). These were found to be $E_H = 0.3341(21)$ eV and $D_H = 2.31(18) \times 10^{-4} \text{ cm}^2 \text{ s}^{-1}$ for the high- T component and $E_L = 0.0313(15)$ eV and $D_L = 7.7(7) \times 10^{-10} \text{ cm}^2 \text{ s}^{-1}$ for the low- T component, respectively.

This extracted E_H is in excellent agreement with values deduced by other techniques [29, 60, 68] and the diffusion rates at high temperatures are very similar to the ones found in rutile nanorods using impedance spectroscopy [68], but three orders of magnitude lower than what is found with β -NMR [29], even though the current measurements agree with β -NMR at low temperatures ($T \sim 150$ K), as can be seen at Fig. 6.5.

From the values of the energy barriers and the pre-exponential factors of the bi-Arrhenius fit, one can easily see that the energy barriers are reported with a much smaller relative uncertainty, compared to the pre-factors. This stems from the fact that a change in the trapping probability P_{tr} in the range discussed above ($P_{tr} \geq 50$ %), results in the bi-Arrhenius plot of $D(T)$ (shown in Fig. 6.5) to be shifted vertically by a constant amount. The lower the value of P_{tr} , the faster the diffusivity, while the energy barriers of the two components are virtually unaffected. Also, note that the uncertainties of the Arrhenius parameters reported here are purely statistical, but the systematic sources of uncertainty, such as possible discrepancies between the various parameters of the Geant4 simulation with the actual experimental configuration, are taken into account in the level of fitting each individual normalized α -yield, by introducing a stretching factor which is able to stretch (or suppress) the measured $Y_\alpha^n(t)$ signals by ~ 10 %. This factor increases the available phase-space of each fit, therefore increases the uncertainty of the diffusivities of each individual fit.

An additional reason for the higher uncertainty of the pre-exponential factors, is that both data sets acquired with beam energies of 10 and 25 keV yield virtually the same bi-Arrhenius activation energies and they are in agreement at high- T , but the low- T component of the 10 keV data is shifted lower by about an order of magnitude (see Fig. 6.6).

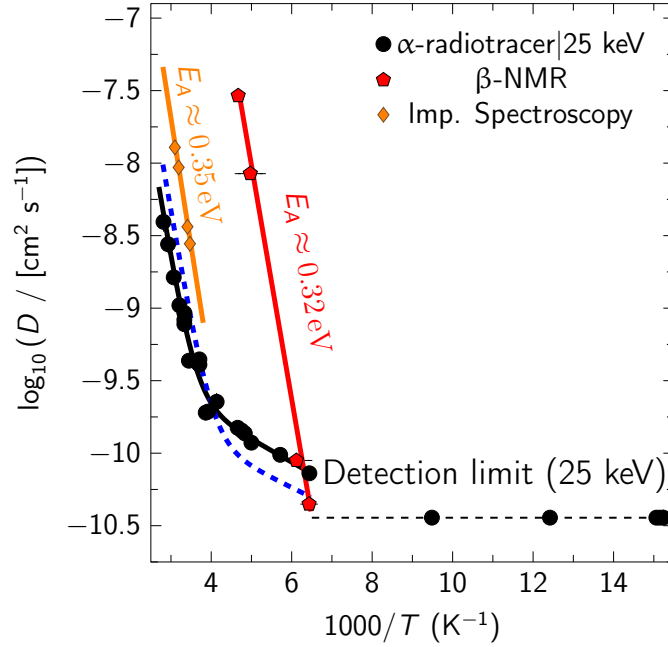


Figure 6.5: Arrhenius plot, comparing reported Li diffusivity in rutile TiO_2 [29, 68]. The solid black line is the bi-Arrhenius fit of Eq. 6.1 with $P_{tr} = 100\%$. The red line is the high- T Arrhenius component found with β -NMR [29]. The blue dashed line is the fit of the present data using the two Arrhenius components found with β -NMR [29], assuming that only a fraction f of the β -NMR fluctuations corresponds to a hop, which f was the only free parameter and yielded $f = 28.1(17) \times 10^{-6}$

For trapping probability $P_{tr} < 100\%$, the apparent gap narrows and for $P_{tr} = 50\%$ is about half an order of magnitude wide. The persistency of the gap suggests that it might be related to either a discrepancy between SRIM and the actual implantation profiles (e.g., due to channeling [170]), or due to some small random disorder close to the surface parameterized by some energy scale (Δ). At higher temperatures when $kT \gg \Delta$ its effect would diminish. Both these effects would affect the (closer to the surface) 10 keV data more than the 25 keV and would become irrelevant at fast diffusivities, explaining the agreement of the two sets at high temperatures and why the diffusion seems slower at low- T for the 10 keV data. The insensitivity of the α -yield $Y_{\alpha}^n(t; \theta)$ to the angle of sample's rotation θ (see Fig. 6.3), suggests that a possible channeling effect cannot be very large, which makes the latter explanation of a near surface random disorder more probable.

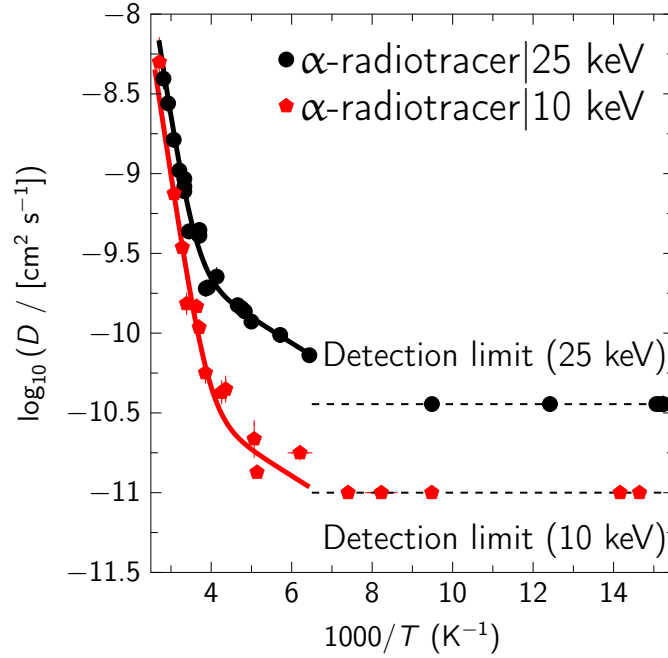


Figure 6.6: Arrhenius fit to the diffusion rates of ^8Li found in this study in (001)-oriented rutile TiO_2 assuming a fully trapping ($P_{tr} = 100\%$) sample surface and the implantation profile provided by SRIM for a beam energy of 10 and 25 keV.

A bi-Arrhenius relationship for diffusivity is not uncommon; in vacancy ion conductors [171], it may occur from a crossover between a region at high- T , where vacancies are thermally generated, to a region at lower T with a shallower slope. As α -radiotracer is always only measuring the diffusion of Li^+ , rather than the net ionic conductivity, the origin of the two Arrhenius components can't be the same as above. While we cannot be conclusive about it, we consider some possibilities.

Using molecular dynamics (MD) in rutile TiO_2 , Gligor et al. [172] found a bi-Arrhenius behavior above room temperature for high Li concentrations, but reported an Arrhenius relation with $E_A \sim 0.22$ eV for low concentrations (Li_xTiO_2 with $x \leq 0.06$). Gilgor et al. attributed the additional Arrhenius component at high concentrations to Li^+ blocking the c -axis channels, resulting in the collective motion of several Li^+ moving together at high temperatures, whereas individual Li^+ ions are thought to be moving at lower temperatures. In spite of the bi-Arrhenius finding, this MD study contrasts ours, as our measurements were taken in ultra dilute concentrations of Li^+ and the second Arrhenius component was found far below room temperature.

To provide a possible explanation of the two Arrhenius components, we consider a recent β -NMR experiment on rutile [29], which also used an implanted $^8\text{Li}^+$ beam on similar crystals. The β -NMR measurements revealed two peaks in the relaxation rate $1/T_1$, one below 100 K and one above 200 K.

Below 100 K, a 0.027 eV barrier was attributed to dynamics of electron-polarons in the vicinity of the implanted ion [157, 173]. Electron-polarons in rutile TiO_2 are manifested as Ti^{3+} centers, produced by an electron trapped at a normally Ti^{4+} ion. These extra electrons can be provided either by oxygen vacancies [174], by doping with Li [173], F or H, by laser illumination [175], or due to electron/hole excitations produced by the implantation process of an ion beam. When Li^+ ions are introduced in rutile at low temperatures (~ 20 K), the interstitial ion has been shown [173] to occupy a position neighboring a Ti^{3+} center, forming therefore a neutral paramagnetic bound Li-polaron complex.

In principle, the dynamics of these complexes might not be diffusive, e.g. the $^8\text{Li}^+$ is static and the polaron is thermally trapped by the Li and cycles through trapping and detrapping. Nonetheless, our current measurement really shows that there is some long range diffusion of $^8\text{Li}^+$ at low- T , with a barrier significantly different than high- T . While our E_L is of a similar magnitude to that found with β -NMR, it is also compatible with the diffusion barrier predicted from theory for isolated Li in rutile [148, 156, 157, 159–161, 163, 172]. The α -radiotracer cannot distinguish whether Li moves either as a simple interstitial, or as part of a Li-polaron complex, it would only identify their weighted average contribution to the motion of $^8\text{Li}^+$. The similarity of the observed activation energy at low temperatures to the theoretical value suggests that a small fraction of the Li^+ interstitials does not combine with a polaron, but rather diffuses as a simple ion. If this fraction is small, that would explain why the low- T pre-factor is so much smaller than the high- T .

It seems possible that the larger activation energy observed above 200 K may involve diffusion of a more complex object, possibly a Li-polaron complex, or it could be related to a dissociation energy of Li^+ with the polarons, which are known to form Coulomb bond defect complexes. Indeed, theory predicts a diffusion barrier of 0.29 eV for the Li-polaron complex and a disassociation energy of 0.45 eV [157], both comparable to the high- T barrier found here. The Li-polaron complex is overall electrically neutral, so its movement should contribute to the diffusivity of Li but not to the ionic conductivity (charge transport). An electric field would not cause it to move - unless it was strong enough to destabilize the complex (strong potential gradient). Thus, if it is a neutral Li-polaron complex moving at high- T , one would expect the impedance measurement to yield a very different Arrhenius slope. This speaks in favor of the Li-polaron dissociation case, but without further investigation we cannot exclude the possibility of Li-polaron diffusion, or a combination of the two aforementioned mechanisms.

The much larger pre-factor above 200 K, compared to low- T , is also quite intriguing and is further evidence that these are two very different mechanisms for diffusion of Li in rutile. Indeed, D_H , when written in terms of frequency, yields $\tau_H^{-1} \sim 2 \times 10^{12} \text{ s}^{-1}$, which is in the 10^{12} - 10^{13} s^{-1} range one would normally expect from phonons driving a thermally activated motion. Note that this frequency is ~ 5000 times smaller than what was found with β -NMR [29], as well as with optical absorption [60].

The above explanation on the nature of the two Arrhenius components relies on the assumption that the Li-polaron complex is stable or metastable at high temperatures. In the absence of Li doping, the intrinsic Ti^{3+} polarons [174] are unstable at high temperatures, with the corresponding electron paramagnetic resonance (EPR) signals vanishing above 20 K [175]. The Li-polaron complex is shown to be more stable, with the EPR signal visible up to 50 K [173] (above which the signal broadens) and the corresponding β -NMR signal being present up to 100 K [29].

There are no studies reporting the existence of Li-polaron complexes above 100 K, but the fact that the dissociation energy for the complex is expected to be large (0.45 eV [157], an order of magnitude larger than the 0.025 eV thermal energy at room temperature), suggests that these complexes might be present at high temperatures and the EPR signal might be broadened by some other process, rather than the dissociation of the complex. For instance, its broadening could reflect the mobilization of the complex, or internal excitations (i.e., polaron hopping locally while still overall bound to Li^+).

One could argue that the Li-polaron complex is unbound in equilibrium at high temperatures (above 100 K), but the ion beam implantation process creates a number of electron/hole pairs in the vicinity of the $^8\text{Li}^+$, which may form the complex with one of the free electrons at higher temperatures for a short time. However, this explanation would suggest that the high- T Arrhenius component is beam-induced, rather than inherent to the crystal and would therefore fail to explain the agreement of E_H with techniques that don't use an ion beam.

An alternative explanation regarding the nature of the two Arrhenius components, would be the opposite of the one discussed above, namely having Li-polaron complex diffusion at low- T and simple interstitial motion at high- T . This scenario has the merit of not requiring the Li-polaron complex to be stable at high temperatures and also explains why the low- T Arrhenius component found with β -NMR has the same activation energy as the one found here. However, it does not provide any insight as to why the energy barrier predicted by DFT for simple interstitial motion is ten times smaller than E_H and (coincidentally?) agrees with E_L , whereas the predicted values for Li-polaron complex diffusion and dissociation are similar to E_H and an order of magnitude larger than E_L .

6.5 Conclusions

In summary, we used the radioactive α -decay of ^8Li to study Li diffusion in a single crystal rutile TiO_2 in the range of 60 K to 370 K.

This work established the feasibility of the α -radiotracer technique, as well as its applicability to answer science-relevant questions about the Li^+ motion in a Li-battery material. It is the first time that α -radiotracer is used to extract the activation energy of the Li^+ motion in a sample. Moreover, it is demonstrated to be the only technique to date that can clearly identify the surface boundary condition of the Li^+ motion.

In rutile TiO_2 , the nanoscale Li diffusion rate was found to exhibit bi-Arrhenius behavior. We report a high- T activation energy of $E_H = 0.3341(21)$ eV, in agreement with measurements carried out with different techniques [29, 60, 68]. At low temperatures, a second Arrhenius component was revealed, with an activation energy of $E_L = 0.0313(15)$ eV. We suggest that this might be related to a small fraction of the Li^+ that does not bind to a Li-polaron complex but rather hops as a simple interstitial with an activation energy near theoretical calculations. In addition, we found evidence that Li traps at the (001)-surface, which could contribute to the reduced Li uptake at room temperature. We believe that this technique can shed new light on the Li motion in Li-ion battery materials and across their interfaces.

Chapter 7

Conclusions and Future Work

7.1 Summary

In this work, we have enhanced the ability to study nanoscale phenomena using the radioactive β - and α -decays of ^8Li and ^9Li .

We showed that by comparing the β -NMR spin lattice relaxation rate (SLR) of ^8Li and ^9Li under the same experimental conditions it is possible to distinguish the source of relaxation in a given sample (Ch. 3). As a proof of principle, we studied a Pt foil and a SrTiO_3 single-crystal. The SLR in Pt was shown to be primarily magnetic in origin, whereas in SrTiO_3 the main source of relaxation was identified to be electric quadrupolar. To further develop the isotopic comparison method of β -NMR, we showed that the ^9Li β -NMR asymmetry can be increased by a factor of at least ~ 2 , by tagging the decay branches of ^9Li in coincidence/anti-coincidence with an emitted α -particle. The isotopic comparison method can greatly enhance the capabilities of β -detected NMR, by providing a tool capable of lifting any ambiguity as to what is the dominant source of spin-lattice relaxation in a given situation.

In the second part of this work, we developed from first principles the α -radiotracer technique and we used it to study the Li motion in rutile TiO_2 .

Detailed simulation studies (Ch. 5) were carried out in order to guide the design of a dedicated spectrometer (Appendix A) and also as a basis of the data analysis tools required for extracting the diffusion rate of Li^+ from the raw α -rate signal.

Using the α -radiotracer technique, we studied the Li^+ motion in rutile TiO_2 , in which we showed that Li^+ gets trapped upon reaching the (001) surface of rutile and that the diffusion rate of Li^+ versus temperature follows a bi-Arrhenius relationship (Ch. 6). The high temperature component was in agreement with other techniques and the previously unknown low temperature component yielded important novel information on the nature of the Li motion. We believe that the α -radiotracer technique is very effective in studying nanoscale Li^+ diffusion, as it is the only experimental technique that directly measures the Li^+ diffusion rate in this scale and can clearly extract the surface trapping probability of Li^+ , which has important implications on the applicability of a given material as part of a Li-ion battery system.

7.1.1 Isotopic comparison for distinguishing magnetic and electric relaxation in β -NMR

As there are instances where the source of the SLR in a β -NMR measurement is not easily identifiable as either magnetic or electric quadrupolar, we developed the isotopic comparison method using ^8Li and ^9Li probes. The basis of the method is that the SLR of the same element should scale between isotopes based on their different nuclear characteristics, such as spin and quadrupole moment. For the case of ^9Li and ^8Li , we showed that the ratio of the relaxation rates of the two isotopes in the limit of fast fluctuations is ~ 7.7 for pure magnetic interactions and ~ 2.1 for purely electric quadrupolar.

Following this theoretical result, we performed β -NMR measurements with both isotopes in two very different materials, namely Pt and SrTiO_3 . Pt is a metal in which ion-implanted Li feels a very small, if any, quadrupolar interaction, so the primary source of relaxation was expected to be through the (magnetic) Korringa hyperfine interaction to the conduction electrons. Indeed, the ratio of the relaxation rates for ^9Li and ^8Li yielded 6.82(29), close to the limit of purely magnetic interactions.

In contrast, the same ratio in SrTiO_3 was 2.7(3), very close to the limit of the spin fluctuations being caused by purely electric quadrupolar interactions. That was expected from a non-magnetic insulator such as SrTiO_3 with very few available nuclear moments. Indeed, previous measurements with ^8Li β -NMR had found all the usual signs of a dominant electric quadrupolar interaction at the stopping site of ^8Li . Hence, we showed that using the isotopic comparison technique with β -NMR using ^8Li and ^9Li as probes, it is possible to infer the primary source of spin lattice relaxation in a given situation.

The ^9Li β -NMR measurements dominated both the time investment and the uncertainty of the isotopic comparison. A large part of the reason behind this is that ^9Li decays into three possible states of ^9Be , two of which are associated with opposite β -decay asymmetry and thus suppress the average β -NMR signal significantly. To increase the usability of the isotopic comparison, we invented a method (termed $\alpha\text{LithEIA}$) of partially resolving the decay branches of ^9Li , by tagging each β -decay in coincidence/anti-coincidence with an α -particle. The α 's are emitted from decays to one of the excited states of ^9Be , whereas a decay to the ground state emits only a β (plus an electron antineutrino for lepton number conservation). Using the $\alpha\text{LithEIA}$ method, we were able to increase the effective asymmetry of ^9Li β -NMR by a factor of ~ 2 .

7.1.2 Establishing the α -radiotracer technique for studying nanoscale Li diffusion

So far, the α -decay of ^8Li had been completely neglected as a means of studying nanoscale phenomena in solids. In this work, we use the rapid attenuation of α -particles in solids to extract the long-range diffusion rate of Li^+ in a direct manner, with the so-called α -radiotracer technique. This allows one to study *at the same time* both the long-range motion of Li^+ (using the α -decay) and its local hop-rate (using β -NMR) with a single ion-implanted radioactive probe (^8Li).

To achieve that, we had to study all aspects of the new technique, in order to find an experimental geometry that is compatible with the constraints of both β -NMR and the α -radiotracer. This was done using a combination of the Monte Carlo Geant4 simulation package and custom codes. The findings of that work were an indispensable guide for the design, development and testing of a novel spectrometer with the specified characteristics, the so-called cryo-oven.

In addition, the aforementioned simulation study doubled as the basis of the data analysis tools required for the extraction of the diffusion rate and the surface trapping probability of Li^+ from the raw experimentally-acquired α -rate.

The conclusion of the simulation study regarding the optimum α -detection geometry was the placement of a thin Al ring just upstream of the sample surface, coated with a layer of ZnS(Ag) paste (ideally ~ 0.1 mm thick). This geometry maximized the quality of the normalized α -signal without diminishing the effective solid angle of the detector. The light produced from α -particles reaching the ZnS(Ag) ring was then guided through a system of lenses to a photomultiplier tube, whose energy threshold was selected again in order to maximize the quality of the signal, based on the simulation.

Moreover, the simulation study showed that it is possible to determine the probability of Li^+ trapping at the surface of the sample, in addition to extracting the diffusion rate and energy barrier of the Li^+ motion. These findings then were put to the test by studying the diffusion of Li^+ in single crystal rutile TiO_2 .

7.1.3 Study of the Li^+ motion in rutile TiO_2 , using the α -radiotracer technique

Rutile TiO_2 is an interesting 1D ion conductor with several open questions regarding the Li interstitial motion through its c -axis and the fate of Li^+ upon reaching its surface. The much slower Li diffusion in the ab -plane makes it an ideal test case for α -radiotracer. Indeed we found no evidence of Li motion perpendicular to the c -axis above the theoretical detection limit of this technique (i.e., $D_{ab} \ll 10^{-12} \text{ cm}^2 \text{ s}^{-1}$), as expected from other studies showing a much lower diffusion rate. In contrast,

the c -axis diffusion rate was much larger than $10^{-12} \text{ cm}^2 \text{ s}^{-1}$ and we were able to get full temperature scans between 60 K and 370 K with two beam energies (10 keV and 25 keV).

These data were then fitted with the model developed through the simulation study (Sect. 7.1.2) and yielded information on both the Li (001)-surface trapping probability and the temperature dependence of the diffusion rate. Based on the analysis, we found that Li^+ has a probability to get trapped upon reaching the (001)-surface of rutile larger or equal to 50 %, with no evidence of de-trapping up to 400 K. In addition, we showed that the temperature dependence of the diffusion rate follows a bi-Arrhenius relationship, rather than a simple Arrhenius.

The Arrhenius component of the diffusion rate that is dominant at high temperatures was found to have an activation energy of 0.3341(21) eV, in excellent agreement with other techniques, including our recent β -NMR measurement.

At lower temperatures – below 200 K – a second, previously unknown, Arrhenius component was revealed, having a diffusion barrier of 0.0313(15) eV. Our recent ^8Li β -NMR measurement in rutile [29] had found a second fluctuation mechanism below 100 K that followed Arrhenius law with a similar activation energy 0.027 eV, but was attributed to local dynamics with the electron-polaron. As α -radiotracer is insensitive to local effects, we concluded that part of the β -NMR signal should be related to long-range Li motion. In addition, the similarity of the low- T activation energy with the theoretical diffusion barrier of the simple Li^+ interstitial, suggests that at low- T a portion of Li^+ does not combine with a polaron and moves as a simple interstitial.

Overall, the work on rutile has showed the capability of the α -radiotracer technique to study the nanoscale Li motion, but also its power to extract new information about diffusion and surface trapping of Li^+ in technologically relevant materials.

7.2 Future Work

Moving forward, there are advances to be made in both the isotopic comparison and the α -radiotracer methods, as well as interesting new research pathways and material properties to be studied using the aforementioned techniques.

As for the isotopic comparison method, the most impactful immediate advance is to remove the distortions of the α -tagged spectrum (see Sect. 3.3). This is expected to further increase the enhancement of the ^9Li asymmetry by an additional factor of ~ 2 . To achieve this, one option would be to move away from the ZnS(Ag) scintillator and design a different α -detector with suppressed noise and better time response (i.e., rapid light output). Such an example would be a Si-strip detector.

Nonetheless, given how successful the current very simple setup is, there is a big incentive to look for other options for cleaning up the α -tagged spectrum. One such option would be to add an additional non-polarized pulse in the sequence of positive and negative helicities (i.e., having a pulse sequence of $P_+ \rightarrow P_0 \rightarrow P_-$). As the unpolarized beam should result in zero β -asymmetry, any variation of the α -tagged spectrum from the $A = 0$ line would be the product of distortion. One could then subtract the unpolarized spectrum from the helicity-resolved ones and recover the actual time-evolution of the undistorted spectrum. The obvious drawback of this option is that it effectively reduces the time used for the actual SLR measurement by 1/3, so it should only be used if its resulting increase in asymmetry sufficiently compensates for that.

Turning to the Li diffusion measurements, we propose to further advance and establish the capabilities of the α -radiotracer technique by studying the motion of $^8\text{Li}^+$ across an interface of two Li-ion battery materials, as well as by increasing the maximum temperature of the cryo-oven. By changing the thermometer lead wires to higher-T materials, it should be possible to increase the maximum temperature of the cryo-oven to ~ 600 K.

Regarding the study of the Li^+ motion through an interesting heterostructure, we propose to use a thin-film of graphene on rutile TiO_2 as our proof-of-principle experiment. On one hand, it has been shown that capping rutile with graphene substantially enhances (up to 100%) Li-ion insertion capacity [176, 177], which was attributed to achieving better conductivity and to a structure that supports insertion reactions [178]. Based on our result that Li^+ traps at the surface of rutile TiO_2 , we think that this increase may, to some extent, be due to a more favorable boundary condition (i.e., a more reflective boundary) for Li intercalation at the surface of rutile. α -radiotracer is the only technique capable of directly extracting this information, so we propose to study how the graphene cap changes the Li^+ surface trapping probability. Moreover, the fact that we have already studied extensively the motion of $^8\text{Li}^+$ in rutile TiO_2 will expedite the study of Li motion in this heterostructure, as we won't have to perform again (during an increasingly limited beam-time) the control measurement of the temperature dependence of Li diffusing in an uncapped single crystal rutile TiO_2 . On the above and on all other samples that we plan to study with β -NMR and/or the α -radiotracer technique(s), we will perform a rigorous characterization of their crystal structure and their surface with other techniques, such as XRD [12] and AFM [14].

Bibliography

- [1] A. Chatzichristos, R. M. L. McFadden, V. L. Karner, D. L. Cortie, C. D. P. Levy, W. A. MacFarlane, G. D. Morris, M. R. Pearson, Z. Salman, and R. F. Kiefl. Determination of the nature of fluctuations using ^8Li and ^9Li β -NMR and spin-lattice relaxation. *Phys. Rev. B*, 96:014307, Jul 2017.
- [2] A. Chatzichristos, R. M. L. McFadden, V. L. Karner, D. L. Cortie, C. D. P. Levy, W. A. MacFarlane, G. D. Morris, M. R. Pearson, Z. Salman, and R. F. Kiefl. Comparison of ^8Li and ^9Li spin relaxation in SrTiO_3 and Pt: A means to distinguish magnetic and electric quadrupolar sources of relaxation. *Proceedings of the 14th International Conference on Muon Spin Rotation, Relaxation and Resonance ($\mu\text{SR}2017$)*, 2018.
- [3] A. Chatzichristos, R. M. L. McFadden, M. H. Dehn, S. R. Dunsiger, D. Fujimoto, V. L. Karner, I. McKenzie, G. D. Morris, M. R. Pearson, M. Stachura, J. Sugiyama, J. O. Ticknor, W. A. MacFarlane, and R. F. Kiefl. Bi-arrhenius diffusion and surface trapping of $^8\text{Li}^+$ in rutile TiO_2 . *Phys. Rev. Lett.*, 123:095901, Aug 2019.
- [4] A. Ohtomo and H. Y. Hwang. A high-mobility electron gas at the $\text{LaAlO}_3/\text{SrTiO}_3$ heterointerface. *Nature*, 427:423—426, 2004.
- [5] R. B. Laughlin. Quantized Hall conductivity in two dimensions. *Phys. Rev. B*, 23:5632–5633, May 1981.
- [6] Mohammad Sabaieian and Ali Khaledi-Nasab. Size-dependent intersubband optical properties of dome-shaped InAs/GaAs quantum dots with wetting layer. *Appl. Opt.*, 51(18):4176–4185, Jun 2012.
- [7] C. L. Kane and E. J. Mele. Z_2 topological order and the quantum spin Hall effect. *Phys. Rev. Lett.*, 95:146802, Sep 2005.
- [8] G. Bayreuther. Magnetic surfaces. *Hyperfine Interactions*, 47(1):237–249, Mar 1989.
- [9] V. Y. Aaron and J. P. Leburton. Flash memory: towards single-electronics. *IEEE Potentials*, 21(4):35–41, Oct 2002.

- [10] A. R. Mellnik, J. S. Lee, A. Richardella, J. L. Grab, M. H. Mintun, P. J. and-Fischer, A. Vaezi, A. Manchon, E.-A. Kim, N. Samarth, and D. C. Ralph. Spin-transfer torque generated by a topological insulator. *Nature*, 511:449–451, 2014.
- [11] Charles P. Slichter. *Principles of Magnetic Resonance*. Springer Series in Solid-State Sciences, 1990.
- [12] Jean-Louis Hodeau, Vincent Favre-Nicolin, Sandra Bos, Hubert Renevier, Emilio Lorenzo, and Jean-Francois Berar. Resonant diffraction. *Chemical Reviews*, 101(6):1843–1868, 2001. PMID: 11710001.
- [13] T.P. Russell. X-ray and neutron reflectivity for the investigation of polymers. *Materials Science Reports*, 5(4):171 – 271, 1990.
- [14] G. Binnig, C. F. Quate, and Ch. Gerber. Atomic force microscope. *Phys. Rev. Lett.*, 56:930–933, Mar 1986.
- [15] G. Binnig and H. Rohrer. Scanning tunneling microscopy. *IBM Journal of Research and Development*, 44(1):279–293, Jan 2000. Copyright - Copyright International Business Machines Corporation Jan/Mar 2000; Last updated - 2017-10-31; CODEN - IBMJAE.
- [16] Riccardo Comin and Andrea Damascelli. *ARPES: A Probe of Electronic Correlations*, pages 31–71. Springer Berlin Heidelberg, Berlin, Heidelberg, 2015.
- [17] D. L. Cortie, T. Buck, M. H. Dehn, V. L. Karner, R. F. Kiefl, C. D. P. Levy, R. M. L. McFadden, G. D. Morris, I. McKenzie, M. R. Pearson, X. L. Wang, and W. A. MacFarlane. β -NMR investigation of the depth-dependent magnetic properties of an antiferromagnetic surface. *Phys. Rev. Lett.*, 116(10):106103, MAR 10 2016.
- [18] Z. Salman, R. F. Kiefl, K. H. Chow, M. D. Hossain, T. A. Keeler, S. R. Kreitzman, C. D. P. Levy, R. I. Miller, T. J. Parolin, M. R. Pearson, H. Saadaoui, J. D. Schultz, M. Smadella, D. Wang, and W. A. MacFarlane. Near-surface structural phase transition of SrTiO₃ studied with zero-field β -detected nuclear spin relaxation and resonance. *Phys. Rev. Lett.*, 96:147601, Apr 2006.
- [19] Z. Salman, M. Smadella, W. A. MacFarlane, B. D. Patterson, P. R. Willmott, K. H. Chow, M. D. Hossain, H. Saadaoui, D. Wang, and R. F. Kiefl. Depth dependence of the structural phase transition of SrTiO₃ studied with β -NMR and grazing incidence x-ray diffraction. *Phys. Rev. B*, 83:224112, Jun 2011.

- [20] Z. Salman, O. Ofer, M. Radovic, H. Hao, M. Ben Shalom, K. H. Chow, Y. Dagan, M. D. Hossain, C. D. P. Levy, W. A. MacFarlane, G. M. Morris, L. Patthey, M. R. Pearson, H. Saadaoui, T. Schmitt, D. Wang, and R. F. Kiefl. Nature of weak magnetism in SrTiO₃/LaAlO₃ multilayers. *Phys. Rev. Lett.*, 109:257207, Dec 2012.
- [21] T. Shigematsu, H. D. Pfannes, and W. Keune. Depth-selective conversion-electron Mössbauer spectroscopy. *Phys. Rev. Lett.*, 45:1206–1209, Oct 1980.
- [22] W. A. MacFarlane. Implanted-ion β -NMR: A new probe for nanoscience. *Solid State Nucl. Magn. Reson.*, 68–69(0):1–12, 2015.
- [23] T. J. Parolin, Z. Salman, K. H. Chow, Q. Song, J. Valiani, H. Saadaoui, A. O’Halloran, M. D. Hossain, T. A. Keeler, R. F. Kiefl, S. R. Kreitzman, C. D. P. Levy, R. I. Miller, G. D. Morris, M. R. Pearson, M. Smadella, D. Wang, M. Xu, and W. A. MacFarlane. High resolution β -NMR study of $^8\text{Li}^+$ implanted in gold. *Phys. Rev. B*, 77:214107, Jun 2008.
- [24] T. J. Parolin, J. Shi, Z. Salman, K. H. Chow, P. Dosanjh, H. Saadaoui, Q. Song, M. D. Hossain, R. F. Kiefl, C. D. P. Levy, M. R. Pearson, and W. A. MacFarlane. Nuclear magnetic resonance study of Li implanted in a thin film of niobium. *Phys. Rev. B*, 80:174109, Nov 2009.
- [25] W. A. MacFarlane, G. D. Morris, K. H. Chow, R. A. Baartman, S. Daviel, S. R. Dunsiger, A. Hatakeyama, S. R. Kreitzman, C. D. P. Levy, R. I. Miller, K. M. Nichol, R. Poutissou, E. Dumont, L. H. Greene, and R. F. Kiefl. Quadrupolar split ^8Li β -NMR in SrTiO₃. *Physica B*, 326(1–4):209–212, 2003.
- [26] W. A. MacFarlane, C. B. L. Tschense, T. Buck, K. H. Chow, D. L. Cortie, A. N. Hariwal, R. F. Kiefl, D. Koumoulis, C. D. P. Levy, I. McKenzie, F. H. McGee, G. D. Morris, M. R. Pearson, Q. Song, D. Wang, Y. S. Hor, and R. J. Cava. β -detected NMR of $^8\text{Li}^+$ in Bi, Sb, and the topological insulator Bi_{0.9}Sb_{0.1}. *Phys. Rev. B*, 90:214422, Dec 2014.
- [27] Z. Salman, D. Wang, K. H. Chow, M. D. Hossain, S. R. Kreitzman, T. A. Keeler, C. D. P. Levy, W. A. MacFarlane, R. I. Miller, G. D. Morris, T. J. Parolin, H. Saadaoui, M. Smadella, and R. F. Kiefl. Magnetic-field effects on the size of vortices below the surface of NbSe₂ detected using low energy β -NMR. *Phys. Rev. Lett.*, 98:167001, Apr 2007.

- [28] T. Dunlop, A.I. Mansour, Z. Salman, K.H. Chow, I. Fan, J. Jung, R.F. Kiefl, S.R. Kreitzman, C.D.P. Levy, W.A. MacFarlane, G.D. Morris, and T.J. Parolin. ^8Li in GaAs studied with β -NMR. *Physica B: Condensed Matter*, 401-402(Supplement C):254 – 257, 2007.
- [29] Ryan M. L. McFadden, Terry J. Buck, Aris Chatzichristos, Chia-Chin Chen, Kim H. Chow, David L. Cortie, Martin H. Dehn, Victoria L. Karner, Dimitrios Koumoulis, C. D. Philip Levy, Chilin Li, Iain McKenzie, Rotraut Merkle, Gerald D. Morris, Matthew R. Pearson, Zaher Salman, Dominik Samuelis, Monika Stachura, Jiyu Xiao, Joachim Maier, Robert F. Kiefl, and W. Andrew MacFarlane. Microscopic dynamics of Li^+ in rutile TiO_2 revealed by ^8Li β -detected Nuclear Magnetic Resonance. *Chemistry of Materials*, 29(23):10187–10197, 2017.
- [30] J. Sugiyama, I. Umegaki, T. Uyama, R. M. L. McFadden, S. Shiraki, T. Hitosugi, Z. Salman, H. Saadaoui, G. D. Morris, W. A. MacFarlane, and R. F. Kiefl. Lithium diffusion in spinel $\text{Li}_4\text{Ti}_5\text{O}_{12}$ and LiTi_2O_4 films detected with ^8Li β -NMR. *Phys. Rev. B*, 96(9):094402, September 2017.
- [31] Iain McKenzie, Chad R. Daley, Robert F. Kiefl, C. D. Philip Levy, W. Andrew MacFarlane, Gerald D. Morris, Matthew R. Pearson, Dong Wang, and James A. Forrest. Enhanced high-frequency molecular dynamics in the near-surface region of polystyrene thin films observed with β -NMR. *Soft Matter*, 11:1755–1761, 2015.
- [32] M. Stachura, R. M. L. McFadden, A. Chatzichristos, M. H. Dehn, A. Gottberg, L. Hemmingsen, A. Jancso, V.L.Karner, R. F. Kiefl, F. H. Larsen, J. Lassen, C. D. P. Levy, R. Li, W. A. MacFarlane, G. D. Morris, S. Pallada, M. R. Pearson, D. Szunyogh, P. W. Thulstrup, and A. Voss. Towards ^{31}Mg - β -NMR resonance linewidths adequate for applications in magnesium chemistry. *Hyperfine Interact*, 238, 2017.
- [33] Gerald D. Morris. β -NMR. *Hyperfine Interact.*, 225(1–3):173–182, 2014.
- [34] Doris Forkel-Wirth. Exploring solid state physics properties with radioactive isotopes. *Reports on Progress in Physics*, 62(4):527, 1999.
- [35] M. Deicher, G. Weyer, and Th. Wichert. Solid state physics at ISOLDE. *Hyperfine Interactions*, 151(1):105–123, Dec 2003.
- [36] K. Matsuta, T. Minamisono, M. Mihara, M. Fukuda, Shengyun Zhu, Y. Masuda, K. Hatanaka, Daqing Yuan, Yongnan Zheng, Yi Zuo, Ping Fang, Dongmei Zhou, T. Ohtsubo, T. Izumikawa, S. Momota, D. Nishimura,

- R. Matsumiya, A. Kitagawa, S. Sato, M. Kanazawa, M. Torikoshi, T. Nagatomo, Y. Nojiri, T. Suzuki, Xizhen Zhang, J. R. Alonso, T. J. M. Symons, S. Kawasaki, S. C. Jeong, Y. Watanabe, and K. Minamisono. Nuclear moments as a probe of electronic structure in material, exotic nuclear structure and fundamental symmetry. *Hyperfine Interactions*, 220(1):21–28, May 2013.
- [37] Yu. G. Abov, A. D. Gulko, and F. S. Dzheparov. Beta-NMR spectroscopy: Modern state and prospects. *Physics of Atomic Nuclei*, 69(10):1701–1710, Oct 2006.
- [38] Jonathan Bagger, Friedhelm Ames, Yu. Bylinskii, Alexander Gottberg, Kathryn Hayashi, Oliver Kester, Shane Koscielniak, Robert Laxdal, Marco Marchetto, and Paul Schaffer. ARIEL at TRIUMF: Science and Technology. In *Proceedings, 9th International Particle Accelerator Conference (IPAC 2018): Vancouver, BC Canada, April 29-May 4, 2018*, page MOXGB2, 2018.
- [39] C. D. P. Levy, M. R. Pearson, R. F. Kiefl, E. Mané, G. D. Morris, and A. Voss. Laser polarization facility. *Hyperfine Interact.*, 225(1–3):165–172, 2014.
- [40] Soonchil Lee. Sensitive detection of NMR for thin films. *Solid State Nuclear Magnetic Resonance*, 71:1 – 10, 2015.
- [41] Pavel Bakulé and Elvezio Morenzoni. Generation and applications of slow polarized muons. *Contemp. Phys.*, 45(3):203–225, 2004.
- [42] Pavel Bakule, Yasuyuki Matsuda, Yasuhiro Miyake, Kanetada Nagamine, Masahiko Iwasaki, Yutaka Ikedo, Koichiro Shimomura, Patrick Strasser, and Shunshuke Makimura. Pulsed source of ultra low energy positive muons for near-surface μ SR studies. *Nuclear Instruments and Methods in Physics Research Section B: Beam Interactions with Materials and Atoms*, 266(2):335 – 346, 2008.
- [43] Elvezio Morenzoni, Thomas Prokscha, Hassan Saadaoui, Zaher Salman, Andreas Suter, Bastian M. Wojek, Jordan Baglo, Ivan Božović, Masrur Hossain, Robert F. Kiefl, Gennady Logvenov, and Oren Ofer. Low-energy muons at PSI: Examples of investigations of superconducting properties in near-surface regions and heterostructures. *Proceedings of the International Symposium on Science Explored by Ultra Slow Muon (USM2013)*, 2014.

- [44] Marina V. Koudriachova, Nicholas M. Harrison, and Simon W. de Leeuw. Diffusion of Li-ions in rutile. An ab initio study. *Solid State Ionics*, 157(1–4):35–38, 2003.
- [45] M. Perrin, Y.M. Saint-Drenan, F. Mattera, and P. Malbranche. Lead–acid batteries in stationary applications: competitors and new markets for large penetration of renewable energies. *Journal of Power Sources*, 144(2):402 – 410, 2005. Selected papers from the Ninth European Lead Battery Conference.
- [46] Carl Johan Rydh and Björn A. Sandén. Energy analysis of batteries in photovoltaic systems. Part II: Energy return factors and overall battery efficiencies. *Energy Conversion and Management*, 46(11):1980 – 2000, 2005.
- [47] Hadeed Ahmed Sher and Khaled E. Addoweesh. Power storage options for hybrid electric vehicles—a survey. *Journal of Renewable and Sustainable Energy*, 4(5):052701, 2012.
- [48] Toyota Electric Vehicles. http://www.toyota-global.com/innovation/environmental_technology/electric_vehicle/.
- [49] Tesla Electric Vehicles. https://www.tesla.com/en_CA/models.
- [50] Bruno Scrosati and Jürgen Garche. Lithium batteries: Status, prospects and future. *Journal of Power Sources*, 195(9):2419 – 2430, 2010.
- [51] Matthew Li, Jun Lu, Zhongwei Chen, and Khalil Amine. 30 years of lithium-ion batteries. *Advanced Materials*, 30(33):1800561, 2018.
- [52] Yoshio Nishi. The development of lithium ion secondary batteries. *The Chemical Record*, 1(5):406–413, 2001.
- [53] Qingsong Wang, Binbin Mao, Stanislav I. Stoliarov, and Jinhua Sun. A review of lithium ion battery failure mechanisms and fire prevention strategies. *Progress in Energy and Combustion Science*, 73:95 – 131, 2019.
- [54] H. Mehrer. *Diffusion in solids*. Springer series in solid state sciences. Springer, 2007.
- [55] M. Wegner, F. Wilangowski, R. Wuerz, and N.A. Stolwijk. Radiotracer diffusion of Ag in Cu(In,Ga)Se₂ thin films. *Thin Solid Films*, 633:31 – 34, 2017. E-MRS 2016 Spring Meeting, Symposium V, Thin-Film Chalcogenide Photovoltaic Materials.

- [56] H. Ishiyama, S. C. Jeong, Y. X. Watanabe, Y. Hirayama, N. Imai, H. S. Jung, H. Miyatake, M. Oyaizu, A. Osa, Y. Otokawa, M. Matsuda, K. Nishio, H. Makii, T. K. Sato, N. Kuwata, J. Kawamura, H. Ueno, Y. H. Kim, S. Kimura, and M. Mukai. Direct measurement of nanoscale lithium diffusion in solid battery materials using radioactive tracer of ^8Li . *Nucl. Instrum. Methods Phys. Res., Sect. B*, 376:379–381, 2016.
- [57] Vickerman J. C. Secondary ion mass spectrometry—basic concepts, instrumental aspects, applications and trends. *Surface and Interface Analysis*, 10(8):435–435, 1987.
- [58] Lifshin Eric. *Electron Microprobe Analysis*. American Cancer Society, 2006.
- [59] Price William S. Pulsed-field gradient nuclear magnetic resonance as a tool for studying translational diffusion: Part 1. Basic theory. *Concepts in Magnetic Resonance*, 9(5):299–336, 1987.
- [60] O. W. Johnson. One-dimensional diffusion of Li in rutile. *Phys. Rev.*, 136:A284–A290, Oct 1964.
- [61] Zhaofeng Deng, Zhian Zhang, Yanqing Lai, Jin Liu, Jie Li, and Yexiang Liu. Electrochemical impedance spectroscopy study of a Lithium/Sulfur battery: Modeling and analysis of capacity fading. *Journal of The Electrochemical Society*, 160(4):A553–A558, 2013.
- [62] G. Vogl and B. Sepiol. Elementary diffusion jump of iron atoms in intermetallic phases studied by Mössbauer spectroscopy—i. FeAl close to equiatomic stoichiometry. *Acta Metallurgica et Materialia*, 42(9):3175 – 3181, 1994.
- [63] Hervé Jobic, Karsten Hahn, Jörg Kärger, Marc Bée, Alain Tuel, Manfred Noack, Irina Girnus, and Gordon J. Kearley. Unidirectional and single-file diffusion of molecules in one-dimensional channel systems. A quasi-elastic neutron scattering study. *The Journal of Physical Chemistry B*, 101(30):5834–5841, 1997.
- [64] A. R. Armstrong, G. Armstrong, J. Canales, R. Garcia, and P. G. Bruce. Lithium-ion intercalation into TiO_2 -B nanowires. *Advanced Materials*, 17(7):862–865, 2005.
- [65] Y.-S. Hu, L. Kienle, Y.-G. Guo, and J. Maier. High lithium electroactivity of nanometer-sized rutile TiO_2 . *Adv. Mater.*, 18(11):1421–1426, 2006.

- [66] M. Anji Reddy, V. Pralong, U. V. Varadaraju, and B. Raveau. Crystallite size constraints on lithium insertion into brookite TiO₂. *Electrochemical and Solid-State Letters*, 11(8):A132–A134, 2008.
- [67] Z. Wen, S. Ci, S. Mao, S. Cui, Z. He, and J. Chen. CNT@TiO₂ nanohybrids for high-performance anode of lithium-ion batteries. *Nanoscale Research Letters*, 8(499), 2013.
- [68] S. Bach, J. P. Pereira-Ramos, and P. Willman. Investigation of lithium diffusion in nano-sized rutile TiO₂ by impedance spectroscopy. *Electrochim. Acta.*, 55(17):4952–4959, 2010.
- [69] Izumi Umegaki, Shigehiro Kawauchi, Hiroshi Sawada, Hiroshi Nozaki, Yuki Higuchi, Kazutoshi Miwa, Yasuhito Kondo, Martin Mansson, Mark Telling, Fiona Coomer, Stephen P. Cottrell, Tsuyoshi Sasaki, Tetsuro Kobayashi, and Jun Sugiyama. Li-ion diffusion in Li intercalated graphite C₆Li and C₁₂Li probed by μ^+ SR. *Phys. Chem. Chem. Phys.*, 19:–, 07 2017.
- [70] O. W. Johnson and H. R. Krouse. Isotopic mass dependence of Li diffusion in rutile. *J. Appl. Phys.*, 37(2):668–670, 1966.
- [71] K. Kanamura, K. Yuasa, and Z. Takehara. Diffusion of lithium in the TiO₂ cathode of a lithium battery. *J. Power Sources*, 20(1–2):127–134, 1987.
- [72] A. V. Churikov, V. A. Zobenkova, and K. I. Pridatko. Lithium intercalation into titanium dioxide films from a propylene carbonate solution. *Russ. J. Electrochem.*, 40(1):63–68, 2004.
- [73] A. V. Churikov, A. V. Ivanishchev, A. V. Ushakov, and V. O. Romanova. Diffusion aspects of lithium intercalation as applied to the development of electrode materials for lithium-ion batteries. *J. Solid State Electrochem.*, 18(5):1425–1441, 2014.
- [74] Hajime Sato, Daisuke Takahashi, Tatsuo Nishina, and Isamu Uchida. Electrochemical characterization of thin-film LiCoO₂ electrodes in propylene carbonate solutions. *J. Power Sources*, 68(2):540–544, 1997.
- [75] Hui Xia, Li Lu, and G. Ceder. Li diffusion in LiCoO₂ thin films prepared by pulsed laser deposition. *J. Power Sources*, 159(2):1422–1427, 2006.
- [76] Hironobu Ishiyama, S.-C. Jeong, Y. X. Watanabe, Y. Hirayama, N. Imai, H. Miyatake, M. Oyaizu, I. Katayama, M. Sataka, A. Osa, Y. Otokawa, M. Matsuda, H. Makii, K. Nishio, T. K. Sato, and A. Nakao. In situ diffusion

measurements in solids using short-lived radioactive tracers of ^8Li and ^{20}Na . *Nucl. Instrum. Methods Phys. Res., Sect. B*, 317:789–792, 2013.

- [77] Hironobu Ishiyama, Sun-Chan Jeong, Yutaka Watanabe, Yoshikazu Hirayama, Nobuaki Imai, Hiroari Miyatake, Michiharu Oyaizu, Ichiro Katayama, Masao Sataka, Akihiko Osa, Yoshinori Otokawa, Makoto Matsuda, and Hiroyuki Makii. Toward online nanoscale diffusion measurements using radioactive ^8Li tracer. *Jpn. J. Appl. Phys.*, 52(1R):010205, 2013.
- [78] H. Ishiyama, S. C. Jeong, Y. X. Watanabe, Y. Hirayama, N. Imai, H. Miyatake, M. Oyaizu, A. Osa, Y. Otokawa, M. Matsuda, K. Nishio, H. Makii, T. K. Sato, N. Kuwata, J. Kawamura, A. Nakao, H. Ueno, Y. H. Kim, S. Kimura, and M. Mukai. In situ lithium diffusion measurement in solid ionic conductors using short-lived radiotracer beam of ^8Li . *Nucl. Instrum. Methods Phys. Res., Sect. B*, 354:297–300, 2015.
- [79] Sun-Chan Jeong, Ichiro Katayama, Hirokane Kawakami, Hironobu Ishiyama, Hiroari Miyatake, Masao Sataka, Akihiro Iwase, Satoshi Okayasu, Hiroyuki Sugai, Shinichi Ichikawa, Katsuhisa Nishio, Yasuharu Sugiyama, Masahito Yahagi, Kazunori Takada, and Mamoru Watanabe. Simulation study on the measurements of diffusion coefficients in solid materials by short-lived radiotracer beams. *Jpn. J. Appl. Phys.*, 42(7R):4576–4583, 2003.
- [80] S.C. Jeong, I. Katayama, H. Kawakami, H. Ishiyama, Y. Watanabe, H. Miyatake, E. Tojyo, M. Oyaizu, K. Enomoto, M. Sataka, S. Okayasu, H. Sugai, S. Ichikawa, K. Nishio, Y. Sugiyama, A. Iwase, M. Yahagi, T. Hashimoto, K. Takada, M. Watanabe, M. Tanigaki, and T. Shinozuka. ^8Li and ^{18}F diffusion experiments in solids — an application of accelerated RNB. *Nucl. Phys. A*, 746:293–297, 2004.
- [81] S.C. Jeong, I. Katayama, H. Kawakami, Y. Watanabe, H. Ishiyama, H. Miyatake, M. Sataka, S. Okayasu, H. Sugai, S. Ichikawa, K. Nishio, T. Nakanoya, N. Ishikawa, Y. Chimi, T. Hashimoto, M. Yahagi, K. Takada, B. C. Kim, M. Watanabe, A. Iwase, Takashi Hashimoto, and T. Ishikawa. Measurement of diffusion coefficients in solids by the short-lived radioactive beam of ^8Li . *Nucl. Instrum. Methods Phys. Res., Sect. B*, 230(1):596–600, 2005.
- [82] I. Jeong, S.C. and Katayama, H. Kawakami, H. Ishiyama, Y. Watanabe, H. Miyatake, E. Tojyo, M. Oyaizu, K. Enomoto, M. Sataka, S. Okayasu, H. Sugai, S.I. Ichikawa, K. Nishio, M. Yahagi, T. Hashimoto, K. Takada,

- M. Watanabe, A. Iwase, and Y. Sugiyama. Direct diffusion studies of solids using radioactive nuclear beams. In Junichi Kawamura, Shinzo Yoshikado, Takashi Sakuma, Yoshitaka Michihiro, Masaru Aniya, and Yoshiaki Ito, editors, *Superionic Conductor Physics*, pages 145–150. World Scientific, Singapore, 2007.
- [83] Sun-Chan Jeong, Ichiro Katayama, Hirokane Kawakami, Yutaka Watanabe, Hironobu Ishiyama, Nobuaki Imai, Yoshikazu Hirayama, Hiroari Miyatake, Masao Sataka, Hiroyuki Sugai, Satoru Okayasu, Shin-Ichi Ichikawa, Katsuhisa Nishio, Shinichi Mitsuoka, Takamitsu Nakanoya, Takashi Hashimoto, Takanori Hashimoto, and Masahito Yahagi. Abnormal Li diffusion in β -LiGa by the formation of defect complex. *Solid State Ionics*, 180(6):626–630, 2009.
- [84] A. Voss, M. R. Pearson, J. Billowes, F. Buchinger, K. H. Chow, J. E. Crawford, M. D. Hossein, R. F. Kiefl, C. D. P. Levy, W. A. MacFarlane, E. Mané, G. D. Morris, T. J. Parolin, H. Saadaoui, Z. Salman, M. Smadella, Q. Song, and D. Wang. Nuclear electric quadrupole moment of ${}^9\text{Li}$ using zero-field β -detected NQR. *J. Phys. G: Nucl. Part. Phys.*, 38(7):075102, 2011.
- [85] X. Fléchar, E. Liénard, O. Naviliat-Cuncic, D. Rodríguez, M. A. G. Alvarez, G. Ban, B. Carniol, D. Etasse, J. M. Fontbonne, A. M. Lallena, and J. Praena. Measurement of the ${}^8\text{Li}$ half-life. *Phys. Rev. C*, 82:027309, Aug 2010.
- [86] D. Borremans, D. L. Balabanski, K. Blaum, W. Geithner, S. Gheysen, P. Himpe, M. Kowalska, J. Lassen, P. Lievens, S. Mallion, R. Neugart, G. Neyens, N. Vermeulen, and D. Yordanov. New measurement and reevaluation of the nuclear magnetic and quadrupole moments of ${}^8\text{Li}$ and ${}^9\text{Li}$. *Phys. Rev. C*, 72:044309, Oct 2005.
- [87] D. E. Alburger and D. H. Wilkinson. Beta decay of ${}^{16}\text{C}$ and ${}^{17}\text{N}$. *Phys. Rev. C*, 13:835–846, Feb 1976.
- [88] M. Birch, B. Singh, I. Dillmann, D. Abriola, T.D. Johnson, E.A. McCutchan, and A.A. Sonzogni. Evaluation of beta-delayed neutron emission probabilities and half-lives for $Z = 2-28$. *Nuclear Data Sheets*, 128(Supplement C):131 – 184, 2015.
- [89] National Nuclear Data Center Database.
<http://www.nndc.bnl.gov/ensdf/>.

- [90] M. Kowalska, D. T. Yordanov, K. Blaum, P. Himpe, P. Lievens, S. Mallion, R. Neugart, G. Neyens, and N. Vermeulen. Nuclear ground-state spins and magnetic moments of ^{27}Mg , ^{29}Mg , and ^{31}Mg . *Phys. Rev. C*, 77:034307, Mar 2008.
- [91] C. Forssén, E. Caurier, and P. Navrátil. Charge radii and electromagnetic moments of Li and Be isotopes from the *ab initio* no-core shell model. *Phys. Rev. C*, 79:021303, Feb 2009.
- [92] H. Saadaoui. *Magnetic Properties Near the Surface of Cuprate Superconductors Studied Using Beta-Detected NMR*. PhD thesis, University of British Columbia, 2009.
- [93] F.C. Barker. Delayed alpha spectra from the beta decay of ^8Li and ^8B . *Australian Journal of Physics*, 42:25–40, 1989.
- [94] TRIUMF Main Cyclotron Facts.
<http://www.triumf.ca/home/about-triumf/about-us/faq-about-triumf/triumf-backgrounder>.
- [95] B. Weber, K. Paton, R. Ma, and T. Pickles. Outcomes of proton beam radiotherapy for large non-peripapillary choroidal and ciliary body melanoma at TRIUMF and the BC Cancer Agency. *Ocul. Oncol. Pathol.*, 2:29–35, 2015.
- [96] D.J. Arseneau, B. Hitti, S.R. Kreitzman, and E. Whidden. The TRIUMF μSR facility. *Hyperfine Interactions*, 106(1):277–282, Apr 1997.
- [97] Pierre Bricault, Friedhelm Ames, Tobias Achtzehn, Marik Dombisky, Francis Labrecque, Jens Lassen, and Jean-Phillipe Lavoie. An overview on TRIUMF's developments on ion source for radioactive beams. *Review of Scientific Instruments*, 79(02A908), 2008.
- [98] ISAC Yield Database.
<http://mis.triumf.ca/science/planning/yield/beam>.
- [99] W. A. MacFarlane, C. D. P. Levy, M. R. Pearson, T. Buck, K. H. Chow, A. N. Hariwal, R. F. Kiefl, F. H. McGee, G. D. Morris, and D. Wang. The initial state of optically polarized $^8\text{Li}^+$ from the β -NMR in Bismuth. *J. Phys.: Conf. Ser.*, 551(1):012059, 2014.
- [100] The ISAC β NMR HomePage.
<http://www.bnmr.triumf.ca/?file=Polarizer>.

- [101] Oren Ofer, K. H. Chow, I. Fan, M. Egilmez, T. J. Parolin, M. D. Hossain, J. Jung, Z. Salman, R. F. Kiefl, C. D. P. Levy, G. D. Morris, M. R. Pearson, H. Saadaoui, Q. Song, D. Wang, and W. A. MacFarlane. $^8\text{Li}^+$ Knight shift and resonance in the enhanced paramagnet Platinum studied by β -NMR. *Phys. Proc.*, 30:156–159, 2012.
- [102] H. Saadaoui, W. A. MacFarlane, Z. Salman, G. D. Morris, Q. Song, K. H. Chow, M. D. Hossain, C. D. P. Levy, A. I. Mansour, T. J. Parolin, M. R. Pearson, M. Smadella, D. Wang, and R. F. Kiefl. Vortex lattice disorder in $\text{YBa}_2\text{Cu}_3\text{O}_7 - \delta$ probed using β -NMR. *Phys. Rev. B*, 80:224503, Dec 2009.
- [103] W. A. MacFarlane, Q. Song, N. J. C. Ingle, K. H. Chow, M. Egilmez, I. Fan, M. D. Hossain, R. F. Kiefl, C. D. P. Levy, G. D. Morris, T. J. Parolin, M. R. Pearson, H. Saadaoui, Z. Salman, and D. Wang. β -detected NMR spin relaxation in a thin film heterostructure of ferromagnetic EuO. *Phys. Rev. B*, 92:064409, Aug 2015.
- [104] J. F. Ziegler, M. D. Ziegler, and J. P. Biersack. SRIM - The stopping and range of ions in matter (2010). *Nuclear Instruments and Methods in Physics Research B*, 268:1818–1823, June 2010.
- [105] C. J. Andreen and R. L. Hines. Critical angles for channeling of 1- to 25-keV H^+ , D^+ , and He^+ ions in gold crystals. *Phys. Rev.*, 159:285–290, Jul 1967.
- [106] Z. Salman, R. F. Kiefl, K. H. Chow, W. A. MacFarlane, S. R. Kreitzman, D. J. Arseneau, S. Daviel, C. D. P. Levy, Y. Maeno, and R. Poutissou. Beta-detected NQR in zero field with a low energy beam of $^8\text{Li}^+$. *Physica B*, 374–375:468–471, 2006.
- [107] M. D. Hossain, H. Saadaoui, T. J. Parolin, Q. Song, D. Wang, M. Smadella, K. H. Chow, M. Egilmez, I. Fan, R. F. Kiefl, S. R. Kreitzman, C. D. P. Levy, G. D. Morris, M. R. Pearson, Z. Salman, and W. A. MacFarlane. The spin lattice relaxation of ^8Li in simple metals. *Physica B*, 404(5):914–916, 2009.
- [108] J. Korringa. Nuclear magnetic relaxation and resonance line shift in metals. *Physica*, 16(7–8):601–610, 1950.
- [109] Izumi Tomeno and Masayuki Oguchi. NMR study of $\text{LiCo}_{1-x}\text{Cr}_x\text{O}_2$ and $\text{Li}_{1-x}\text{Na}_x\text{CoO}_2$ ($x=0$ and 0.05). *J. Phys. Soc. Jpn.*, 67(1):318–322, 1998.
- [110] Ofer Oren, Chow K. H., Fan I., Egilmez M., Parolin T. J., Hossain M. D., Jung J., Salman Z., Kiefl R. F., Levy C. D. P., Morris G. D., Pearson M. R., Saadaoui H., Song Q., Wang D., and MacFarlane W. A. β -NMR study of

isolated ${}^8\text{Li}^+$ in the enhanced paramagnet platinum. *Phys. Rev. B*, 86:064419, Aug 2012.

- [111] Anatole Abragam. *Principles of Nuclear Magnetism*. Oxford University Press, 1983.
- [112] N. J. Stone. Table of nuclear magnetic dipole and electric quadrupole moments. *At. Data Nucl. Data Tables*, 90(1):75–176, 2005.
- [113] J. G. Bednorz and K. A. Müller. $\text{Sr}_{1-x}\text{Ca}_x\text{TiO}_3$: An XY quantum ferroelectric with transition to randomness. *Phys. Rev. Lett.*, 52:2289–2292, Jun 1984.
- [114] I. Fan, K. H. Chow, T. J. Parolin, M. Egilmez, M. D. Hossain, J. Jung, T. A. Keeler, R. F. Kiefl, S. R. Kreitzman, C. D. P. Levy, R. Ma, G. D. Morris, M. R. Pearson, H. Saadaoui, Z. Salman, M. Smadella, Q. Song, D. Wang, M. Xu, and W. A. MacFarlane. β -NMR of a thin Pt film. *Physica B*, 404(5–7):906–909, 2009.
- [115] W. A. MacFarlane, T. J. Parolin, D. L. Cortie, K. H. Chow, M. D. Hossain, R. F. Kiefl, C. D. P. Levy, R. M. L. McFadden, G. D. Morris, M. R. Pearson, H. Saadaoui, Z. Salman, Q. Song, and D. Wang. ${}^8\text{Li}^+$ β -NMR in the cubic insulator MgO. *J. Phys.: Conf. Ser.*, 551(1):012033, 2014.
- [116] W. A. MacFarlane, G. D. Morris, T. R. Beals, K. H. Chow, R. A. Baartman, S. Daviel, S. R. Dunsiger, A. Hatakeyama, S. R. Kreitzman, C. D. P. Levy, R. I. Miller, K. M. Nichol, R. Poutissou, and R. F. Kiefl. ${}^8\text{Li}$ β -NMR in thin metal films. *Physica B*, 326(1–4):213–216, 2003.
- [117] T. J. Parolin, Z. Salman, J. Chakhalian, Q. Song, K. H. Chow, M. D. Hossain, T. A. Keeler, R. F. Kiefl, S. R. Kreitzman, C. D. P. Levy, R. I. Miller, G. D. Morris, M. R. Pearson, H. Saadaoui, D. Wang, and W. A. MacFarlane. β -NMR of isolated lithium in nearly ferromagnetic palladium. *Phys. Rev. Lett.*, 98:047601, Jan 2007.
- [118] Z. Salman, A. I. Mansour, K. H. Chow, M. Beaudoin, I. Fan, J. Jung, T. A. Keeler, R. F. Kiefl, C. D. P. Levy, R. C. Ma, G. D. Morris, T. J. Parolin, D. Wang, and W. A. MacFarlane. β -NMR of isolated ${}^8\text{Li}^+$ implanted into a thin copper film. *Phys. Rev. B*, 75:073405, Feb 2007.
- [119] D. Wang, Z. Salman, K. H. Chow, I. Fan, M. D. Hossain, T. A. Keeler, R. F. Kiefl, C. D. P. Levy, A. I. Mansour, G. D. Morris, M. R. Pearson, T. J. Parolin, H. Saadaoui, M. Smadella, Q. Song, and W. A. MacFarlane. Nuclear spin relaxation/resonance of ${}^8\text{Li}$ in Al. *Physica B*, 404(5–7):920–923, 2009.

- [120] K. H. Chow, A. I. Mansour, I. Fan, R. F. Kiefl, G. D. Morris, Z. Salman, T. Dunlop, W. A. MacFarlane, H. Saadaoui, O. Mosendz, B. Kardasz, B. Heinrich, J. Jung, C. D. P. Levy, M. R. Pearson, T. J. Parolin, D. Wang, M. D. Hossain, Q. Song, and M. Smadella. Detection and decoherence of level-crossing resonances of ^8Li in Cu. *Phys. Rev. B*, 85:092103, Mar 2012.
- [121] M. Smadella, Z. Salman, K. H. Chow, M. Egilmez, I. Fan, M. D. Hossain, R. F. Kiefl, S.R. Kreitzman, C.D.P. Levy, W.A. MacFarlane, A. I. Mansour, G. D. Morris, T. J. Parolin, M. Pearson, H. Saadaoui, Q. Song, and D. Wang. Surface dependent structural phase transition in SrTiO_3 observed with spin relaxation of ^8Li . *Physica B*, 404(5–7):924–926, 2009.
- [122] Mats Johansson and Peter Lemmens. *Crystallography and Chemistry of Perovskites in the Handbook of Magnetism and Advanced Magnetic Materials*. American Cancer Society, 2007.
- [123] Z. Salman, E. P. Reynard, W. A. MacFarlane, K. H. Chow, J. Chakhalian, S. R. Kreitzman, S. Daviel, C. D. P. Levy, R. Poutissou, and R. F. Kiefl. β -detected nuclear quadrupole resonance with a low-energy beam of $^8\text{Li}^+$. *Phys. Rev. B*, 70:104404, Sep 2004.
- [124] Richard B. Firestone and Virginia S. Shirley. *Table of isotopes*. J. Wiley, New York, 8th edition, 1996.
- [125] S. Agostinelli, J. Allison, K. Amako, J. Apostolakis, H. Araujo, P. Arce, M. Asai, D. Axen, S. Banerjee, G. Barrand, F. Behner, L. Bellagamba, J. Boudreau, L. Broglia, A. Brunengo, H. Burkhardt, S. Chauvie, J. Chuma, R. Chytrcek, G. Cooperman, G. Cosmo, P. Degtyarenko, A. Dell'Acqua, G. Depaola, D. Dietrich, R. Enami, A. Feliciello, C. Ferguson, H. Fesefeldt, G. Folger, F. Foppiano, A. Forti, S. Garelli, S. Giani, R. Giannitrapani, D. Gibin, J. J. Gómez Cadenas, I. González, G. Gracia Abril, G. Greeniaus, W. Greiner, V. Grichine, A. Grossheim, S. Guatelli, P. Gumplinger, R. Hamatsu, K. Hashimoto, H. Hasui, A. Heikkinen, A. Howard, V. Ivanchenko, A. Johnson, F. W. Jones, J. Kallenbach, N. Kanaya, M. Kawabata, Y. Kawabata, M. Kawaguti, S. Kelner, P. Kent, A. Kimura, T. Kodama, R. Kokoulin, M. Kossov, H. Kurashige, E. Lamanna, T. Lampén, V. Lara, V. Lefebure, F. Lei, M. Liendl, W. Lockman, F. Longo, S. Magni, M. Maire, E. Medernach, K. Minamimoto, P. Mora de Freitas, Y. Morita, K. Murakami, M. Nagamatu, R. Nartallo, P. Nieminen, T. Nishimura, K. Ohtsubo, M. Okamura, S. O'Neale, Y. Oohata, K. Paech, J. Perl, A. Pfeiffer, M. G. Pia, F. Ranjard, A. Rybin, S. Sadilov, E. Di Salvo, G. Santin, T. Sasaki, N. Savvas, Y. Sawada, S. Scherer, S. Sei, V. Sirotenko,

- D. Smith, N. Starkov, H. Stoecker, J. Sulkimo, M. Takahata, S. Tanaka, E. Tcherniaev, E. Safai Tehrani, M. Tropeano, P. Truscott, H. Uno, L. Urban, P. Urban, M. Verderi, A. Walkden, W. Wander, H. Weber, J. P. Wellisch, T. Wenaus, D. C. Williams, D. Wright, T. Yamada, H. Yoshida, and D. Zschiesche. Geant4 — a simulation toolkit. *Nucl. Instrum. Methods Phys. Res., Sect. A*, 506(3):250–303, 2003.
- [126] John S. McCloy, Mary Bliss, Brian Miller, Zheming Wang, and Sean Stave. Scintillation and luminescence in transparent colorless single and polycrystalline bulk ceramic ZnS. *Journal of Luminescence*, 157:416 – 423, 2015.
- [127] D. Qin, G. Yang, G. He, L. Zhang, Q. Zhang, and L. Li. The investigation on synthesis and optical properties of ZnS: Co nanocrystals by using hydrothermal method. *Chalcogenide Letters*, 9:441 – 446, 2012.
- [128] J J Davies and J E Nicholls. Optically detected magnetic resonance of strongly coupled donor-acceptor pairs in ZnS. *Journal of Physics C: Solid State Physics*, 15(25):5321, 1982.
- [129] Dongyang Jiang, Zheng Zhang, Rui-Xue Liang, Zhi-Hong Zhang, Yang Li, Qiang Zhao, and Xiao-Ping Ouyang. Electronic structure and optical properties of the scintillation material wurtzite ZnS(Ag). *Nuclear Science and Techniques*, 28, 03 2017.
- [130] V.B. Mikhailik, S. Henry, M. Horn, H. Kraus, A. Lynch, and M. Pipe. Investigation of luminescence and scintillation properties of a ZnS–Ag/⁶LiF scintillator in the 7–295 K temperature range. *Journal of Luminescence*, 134:63 – 66, 2013.
- [131] Tsunesaburo Asada, Masayoshi Masuda, Masayuki Okumura, and Juzo Okuma. Decay properties of ZnS(Ag) phosphors. *Journal of the Physical Society of Japan*, 14(12):1766–1770, 1959.
- [132] S. Chandrasekhar. Stochastic problems in physics and astronomy. *Rev. Mod. Phys.*, 15:1–89, Jan 1943.
- [133] George H. Vineyard. Frequency factors and isotope effects in solid state rate processes. *Journal of Physics and Chemistry of Solids*, 3(1):121 – 127, 1957.
- [134] C. A. Wert. Diffusion coefficient of C in α -Iron. *Phys. Rev.*, 79:601–605, Aug 1950.

- [135] J. Allison, K. Amako, J. Apostolakis, H. Araujo, P. A. Dubois, M. Asai, G. Barrand, R. Capra, S. Chauvie, R. Chytraccek, G. A. P. Cirrone, G. Cooperman, G. Cosmo, G. Cuttone, G. G. Daquino, M. Donszelmann, M. Dressel, G. Folger, F. Foppiano, J. Generowicz, V. Grichine, S. Guatelli, P. Gumplinger, A. Heikkinen, I. Hrivnacova, A. Howard, S. Incerti, V. Ivanchenko, T. Johnson, F. Jones, T. Koi, R. Kokoulin, M. Kossov, H. Kurashige, V. Lara, S. Larsson, F. Lei, O. Link, F. Longo, M. Maire, A. Mantero, B. Mascialino, I. McLaren, P. M. Lorenzo, K. Minamimoto, K. Murakami, P. Nieminen, L. Pandola, S. Parlati, L. Peralta, J. Perl, A. Pfeiffer, M. G. Pia, A. Ribon, P. Rodrigues, G. Russo, S. Sadilov, G. Santin, T. Sasaki, D. Smith, N. Starkov, S. Tanaka, E. Tcherniaev, B. Tome, A. Trindade, P. Truscott, L. Urban, M. Verderi, A. Walkden, J. P. Wellisch, D. C. Williams, D. Wright, and H. Yoshida. Geant4 developments and applications. *IEEE Trans. Nucl. Sci.*, 53:270–278, 2006.
- [136] J. Allison, K. Amako, J. Apostolakis, P. Arce, M. Asai, T. Aso, E. Bagli, A. Bagulya, S. Banerjee, G. Barrand, B. R. Beck, A. G. Bogdanov, D. Brandt, J. M. C. Brown, H. Burkhardt, Ph. Canal, D. Cano-Ott, S. Chauvie, K. Cho, G. A. P. Cirrone, G. Cooperman, M. A. Cortés-Giraldo, G. Cosmo, G. Cuttone, G. Depaola, L. Desorgher, X. Dong, A. Dotti, V. D. Elvira, G. Folger, Z. Francis, A. Galoyan, L. Garnier, M. Gayer, K. L. Genser, V. M. Grichine, S. Guatelli, P. Guèye, P. Gumplinger, A. S. Howard, I. Hřivnáčová, S. Hwang, S. Incerti, A. Ivanchenko, V. N. Ivanchenko, F. W. Jones, S. Y. Jun, P. Kaitaniemi, N. Karakatsanis, M. Karamitros, M. Kelsey, A. Kimura, T. Koi, H. Kurashige, A. Lechner, S. B. Lee, F. Longo, M. Maire, D. Mancusi, A. Mantero, E. Mendoza, B. Morgan, K. Murakami, T. Nikitina, L. Pandola, P. Paprocki, J. Perl, I. Petrović, M. G. Pia, W. Pokorski, J. M. Quesada, M. Raine, M. A. Reis, A. Ribon, A. Ristić Fira, F. Romano, G. Russo, G. Santin, T. Sasaki, D. Sawkey, J. I. Shin, I. I. Strakovsky, A. Taborda, S. Tanaka, B. Tomé, T. Toshito, H.N. Tran, P.R. Truscott, L. Urban, V. Uzhinsky, J. M. Verbeke, M. Verderi, B. L. Wendt, H. Wenzel, D. H. Wright, D. M. Wright, T. Yamashita, J. Yarba, and H. Yoshida. Recent developments in Geant4. *Nucl. Instrum. Methods Phys. Res., Sect. A*, 835:186–225, 2016.
- [137] S. Incerti, G. Baldacchino, M. Bernal, R. Capra, C. Champion, Z. Francis, P. Guèye, A. Mantero, B. Mascialino, P. Moretto, P. Nieminen, C. Villagrasa, and C. Zacharatou. The GEANT4-DNA project. *Int. J. Model. Simul. Sci. Comput.*, 01(02):157–178, 2010.

- [138] Geant4 Physics Models Catalog. http://geant4.web.cern.ch/geant4/support/proc_mod_catalog/models/.
- [139] M. V. Reddy, G. V. Subba Rao, and B. V. R. Chowdari. Metal oxides and oxysalts as anode materials for Li ion batteries. *Chem. Rev.*, 113(7):5364–5457, 2013.
- [140] Jeremy K. Burdett, Timothy Hughbanks, Gordon J. Miller, James W. Richardson, and Joseph V. Smith. Structural-electronic relationships in inorganic solids: powder neutron diffraction studies of the rutile and anatase polymorphs of titanium dioxide at 15 and 295 K. *J. Am. Chem. Soc.*, 109(12):3639–3646, 1987.
- [141] Ulrike Diebold. The surface science of titanium dioxide. *Surf. Sci. Rep.*, 48(5–8):53–229, 2003.
- [142] Akira Fujishima, Xintong Zhang, and Donald A. Tryk. TiO₂ photocatalysis and related surface phenomena. *Surf. Sci. Rep.*, 63(12):515–582, 2008.
- [143] Kyriakos Bourikas, Christos Kordulis, and Alexis Lycourghiotis. Titanium dioxide (anatase and rutile): Surface chemistry, liquid-solid interface chemistry, and scientific synthesis of supported catalysts. *Chem. Rev.*, 114(19):9754–9823, 2014.
- [144] Madhavan Ramamoorthy, David Vanderbilt, and R. D. King-Smith. First-principles calculations of the energetics of stoichiometric TiO₂ surfaces. *Phys. Rev. B*, 49:16721–16727, Jun 1994.
- [145] J. Muscat and N. M. Harrison. The physical and electronic structure of the rutile (001) surface. *Surf. Sci.*, 446(1):119–127, 2000.
- [146] A. Hallil, E. Amzallag, S. Landron, and R. Tétot. Properties of rutile TiO₂ surfaces from a tight-binding variable-charge model. comparison with ab initio calculations. *Surf. Sci.*, 605(7):738–745, 2011.
- [147] Chinedu E. Ekuma and Diola Bagayoko. Ab-initio electronic and structural properties of rutile titanium dioxide. *Japanese Journal of Applied Physics*, 50(10R):101103, 2011.
- [148] Marina V. Koudriachova, Nicholas M. Harrison, and Simon W. de Leeuw. Density-functional simulations of lithium intercalation in rutile. *Phys. Rev. B*, 65:235423, Jun 2002.

- [149] James A. Van Orman and Katherine L. Crispin. Diffusion in oxides. *Rev. Mineral. Geochem.*, 72(1):757–825, 2010.
- [150] John Christopher Bachman, Sokseiha Muy, Alexis Grimaud, Hao-Hsun Chang, Nir Pour, Simon F. Lux, Odysseas Paschos, Filippo Maglia, Saskia Lupart, Peter Lamp, Livia Giordano, and Yang Shao-Horn. Inorganic solid-state electrolytes for Lithium Batteries: Mechanisms and properties governing ion conduction. *Chem. Rev.*, 116(1):140–162, 2016.
- [151] D. W. Murphy, R. J. Cava, S. M. Zahurak, and A. Santoro. Ternary Li_xTiO_2 phases from insertion reactions. *Solid State Ionics*, 9–10:413–417, 1983.
- [152] B. Zachau-Christiansen, K. West, T. Jacobsen, and S. Atlung. Lithium insertion in different TiO_2 modifications. *Solid State Ionics*, 28–30:1176–1182, 1988.
- [153] J. Heine, M. Wilkening, and P. Heitjans. Slow Li^+ self-diffusion in Li intercalated nanometer-sized needlelike rutile TiO_2 as probed by mixing time dependent ^7Li stimulated echo NMR spectroscopy. *Diffus. Fundament.*, 12:95–96, 2010.
- [154] R. M. L. McFadden, D. L. Cortie, D. J. Arseneau, T. J. Buck, C.-C. Chen, M. H. Dehn, S. R. Dunsiger, R. F. Kiefl, C. D. P. Levy, C. Li, G. D. Morris, M. R. Pearson, D. Samuelis, J. Xiao, J. Maier, and W. A. MacFarlane. β -NMR of $^8\text{Li}^+$ in rutile TiO_2 . *J. Phys.: Conf. Ser.*, 551(1):012032, 2014.
- [155] Denise Prutsch, Stefan Breuer, Marlena Uitz, Patrick Bottke, Julia Langer, Sarah Lunghammer, Martin Philipp, Patrick Posch, Veronika Pregartner, Bernhard Stanje, Andreas Dunst, Dominik Wohlmuth, Harald Brandstätter, Walter Schmidt, Viktor Epp, Alan Chadwick, Ilie Hanzu, and Martin Wilkening. Nanostructured ceramics: Ionic transport and electrochemical activity. *Z. Phys. Chem.*, 231(7–8):1361–1405, 2017.
- [156] Marina V. Koudriachova, Nicholas M. Harrison, and Simon W. de Leeuw. Effect of diffusion on lithium intercalation in titanium dioxide. *Phys. Rev. Lett.*, 86:1275–1278, Feb 2001.
- [157] Sebastien Kerisit, Kevin M. Rosso, Zhenguo Yang, and Jun Liu. Dynamics of coupled lithium/electron diffusion in TiO_2 polymorphs. *J. Phys. Chem. C*, 113(49):20998–21007, 2009.
- [158] Peter V. Sushko, Kevin M. Rosso, and Igor V. Abarenkov. Interaction of intercalated Li^+ ions with oxygen vacancies in rutile TiO_2 . *ECS Trans.*, 28(11):299–306, 2010.

- [159] Handan Yildirim, Jeffrey P. Greeley, and Subramanian K. R. S. Sankaranarayanan. The effect of concentration on Li diffusivity and conductivity in rutile TiO₂. *Phys. Chem. Chem. Phys.*, 14:4565–4576, 2012.
- [160] Sebastien Kerisit, Anne M. Chaka, Timothy C. Droubay, and Eugene S. Ilton. Shell model for atomistic simulation of lithium diffusion in mixed Mn/Ti oxides. *J. Phys. Chem. C*, 118(42):24231–24239, 2014.
- [161] Jongbo Jung, Maenghyo Cho, and Min Zhou. Density functional theory study of the mechanism of Li diffusion in rutile RuO₂. *AIP Adv.*, 4(1):017104, 2014.
- [162] Jayeon Baek, Soomin Park, Chyan Kyung Song, Tae Yong Kim, Inho Nam, Jong Min Lee, Jeong Woo Han, and Jongheop Yi. Radial alignment of *c*-channel nanorods in 3D porous TiO₂ for eliciting enhanced Li storage performance. *Chem. Commun.*, 51:15019–15022, 2015.
- [163] Corinne Arrouvel, Thiago C. Peixoto, Mario E. G. Valerio, and Stephen C. Parker. Lithium migration at low concentration in TiO₂ polymorphs. *Comput. Theor. Chem.*, 1072:43–51, 2015.
- [164] G. D. Morris, W. A. MacFarlane, K. H. Chow, Z. Salman, D. J. Arseneau, S. Daviel, A. Hatakeyama, S. R. Kreitzman, C. D. P. Levy, R. Poutissou, R. H. Heffner, J. E. Elenewski, L. H. Greene, and R. F. Kiefl. Depth-controlled β -NMR of ⁸Li in a thin silver film. *Phys. Rev. Lett.*, 93:157601, Oct 2004.
- [165] F. James and M. Roos. MINUIT — a system for function minimization and analysis of the parameter errors and correlations. *Comput. Phys. Commun.*, 10(6):343–367, 1975.
- [166] Rene Brun and Fons Rademakers. ROOT — an object oriented data analysis framework. *Nucl. Instrum. Methods Phys. Res., Sect. A*, 389(1–2):81–86, 1997. <https://root.cern.ch/>.
- [167] Yuri F. Zhukovskii, Palani Balaya, Eugene A. Kotomin, and Joachim Maier. Evidence for interfacial-storage anomaly in nanocomposites for lithium batteries from first-principles simulations. *Phys. Rev. Lett.*, 96:058302, Feb 2006.
- [168] H. Okuyama, W. Siga, N. Takagi, M. Nishijima, and T. Aruga. Path and mechanism of hydrogen absorption at Pd(100). *Surface Science*, 401(3):344–354, 1998.

- [169] Yasuro Ikuma, Makoto Yamana, Satoshi Yokose, Koichi Niwa, Srinivasan Anandan, Daiki Kuroda, Hiroo Tajiri, and Osami Sakata. Surface X-ray diffraction study of annealed single-crystal rutile TiO₂ (001) surface. *Ionics*, 25(4):1879–1886, Apr 2019.
- [170] T.R. Beals, R.F. Kiefl, W.A. MacFarlane, K.M. Nichol, G.D. Morris, C.D.P. Levy, S.R. Kreitzman, R. Poutissou, S. Daviel, R.A. Baartman, and K.H. Chow. Range straggling of low energy ⁸Li⁺ in thin metallic films using β -NMR. *Physica B: Condensed Matter*, 326(1):205 – 208, 2003.
- [171] Irene E. Hooton and P. W. M. Jacobs. Ionic conductivity of pure and doped sodium chloride crystals. *Canadian Journal of Chemistry*, 66(4):830–835, 1988.
- [172] F. Gligor and S. W. de Leeuw. Lithium diffusion in rutile structured titania. *Solid State Ionics*, 177(26–32):2741–2746, 2006.
- [173] A.T. Brant, N.C. Giles, and L.E. Halliburton. Insertion of lithium ions into TiO₂ (rutile) crystals: An electron paramagnetic resonance study of the Li-associated Ti₃⁺ small polaron. *Journal of Applied Physics*, 113(5):053712, 2013.
- [174] L. A. K. Dominik and R. K. MacCrone. Dielectric relaxations in reduced rutile (TiO_{2-x}) at low temperatures. *Phys. Rev.*, 163:756–768, Nov 1967.
- [175] Shan Yang, A. Brant, N. Giles, and Larry Halliburton. Intrinsic small polarons in rutile TiO₂. *Physical Review B*, 87:125201–, 03 2013.
- [176] Mahmoud Madian, Alexander Eychmüller, and Lars Giebeler. Current advances in TiO₂-based nanostructure electrodes for high performance lithium ion batteries. *Batteries*, 4(1), 2018.
- [177] Donghai Wang, Daiwon Choi, Juan Li, Zhenguo Yang, Zimin Nie, Rong Kou, Dehong Hu, Chongmin Wang, Laxmikant V. Saraf, Jiguang Zhang, Ilhan A. Aksay, and Jun Liu. Self-assembled TiO₂-graphene hybrid nanostructures for enhanced Li-ion insertion. *ACS Nano*, 3(4):907–914, 2009.
- [178] Lifang He, Ruguang Ma, Ning Du, Jianguo Ren, Tailun Wong, Yangyang Li, and Shuitong Lee. Growth of TiO₂ nanorod arrays on reduced graphene oxide with enhanced lithium-ion storage. *J. Mater. Chem.*, 22:19061–19066, 2012.

- [179] J. Apostolakis, S. Giani, M. Maire, P. Nieminen, M.G. Pia, and L. Urban. Geant4 low energy electromagnetic models for electrons and photons. *CERN-OPEN*, 99(034), 1999.
- [180] D.H. Wright and M.H. Kelsey. The Geant4 Bertini cascade. *Nuclear Instruments and Methods in Physics Research Section A: Accelerators, Spectrometers, Detectors and Associated Equipment*, 804:175 – 188, 2015.

Appendix A

The cryo-oven

In this appendix, the characteristics of the new cryo-oven are discussed. The geometry of this new apparatus is designed around the α -detection system discussed in Ch. 5.

Starting from the sample itself, it sits on an Aluminum sample holder, which contains three sample positions and two thermometers, one Pt resistor and one Si diode (see Fig. A.1). The Pt resistor can measure temperatures up to 873 K (600 °C), but does not work below 30 K, whereas the Si diode is functional at low temperatures but unable to measure above 523 K (i.e., 250 °C).

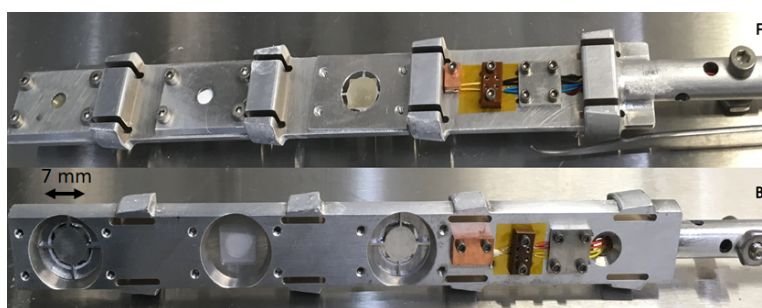


Figure A.1: Figure showing the sample holder used in the cryo-oven assembly. The top picture (F) is the side facing the beam and the lower one (B) the back of the sample holder. At the right hand side, the two thermometers are visible, both the Pt resistor (top picture) and the Si diode (lower picture). To their left, the three sample positions can be seen. On the middle position, there is an Al_2O_3 crystal coated with ZnS(Ag) and capped with a 3 mm \varnothing Al collimator. It is used for $^8\text{Li}^+$ beam diagnostics. On the top and bottom positions, the (001) and (110)-oriented rutile TiO_2 samples are sitting on the 7x7 mm² slot, which has a circular gap around it for the light emitted from the ZnS(Ag) to go through. On the front of the two samples (top picture), there is an Al ring coated with ZnS powder. At the rightmost sample, this ring is visible, as the Al collimator was not installed yet at the time the picture was taken. The Al collimator is then installed on top of the Al ring, as shown in the leftmost sample position. It allows only the centered part of the $^8\text{Li}^+$ beam to reach the sample.

The sample-mounting concept and process is identical to the conventional β -NQR cryostat, as discussed in Sect. 2.2.2. The only difference is that the samples intended to be studied with the α -radiotracer technique should be mounted on a special $7 \times 7 \text{ mm}^2$ base, which sits on the regular $12 \times 12 \text{ mm}^2$ slot. On the upstream side of the sample, a ring painted with ZnS(Ag) and a Al mask with a pinhole are also mounted (see Fig. A.1).

The Al collimator, mounted $\sim 1 \text{ mm}$ upstream of the sample, stops the ^8Li beam from getting implanted off-center, as discussed in Ch. 5.

The light produced from the ZnS(Ag) ring passes through the peripheral hole around the $7 \times 7 \text{ mm}^2$ base and can reach the photomultiplier tube (PMT) lying outside vacuum after getting focused on its front surface by a system of two convex lenses. The first lens is mounted on the radiation shield of the cryo-oven, whereas the second one is mounted outside vacuum, at the front of the PMT housing. This light-collection system is depicted on Fig. 5.2.

The lower region of the cryo-oven, with the α -detection, the cooling and heating systems visible, can be seen on Fig. A.2a. In the two cuts shown in that figure, one can identify the following parts:

1. The front (Fig. A.2a) and back (Fig. A.2b) sides of the three sample positions on the Aluminum sample holder at the end of a hollow stainless steel rod.
2. The position of the Si diode (Fig. A.2a) and Pt resistor (Fig. A.2b) thermometers occupying the topmost (blind) position on the sample holder.
3. Vertical-cut views of the radiation shield installed around the sample region.
4. View of the beam collimator positioned on the radiation shield upstream of the sample (Fig. A.2a).
5. Images of the optical viewport with a convex lens positioned on the radiation shield at the back (i.e., downstream) side of the sample.
6. The Al wedge piece on which the sample holder sits.
7. The electric heater.
8. The liquid He inlet tube.
9. The liquid He exhaust tube.

In addition to the two above-mentioned thermometers on the sample holder, there is a thermometer mounted on the Al wedge piece, one on the copper heater and one on the radiation shield, all Pt resistors.

Fig. A.3a shows the whole cryo-oven assembly both externally (Fig. A.3a) and as an isometric cut (Fig. A.3b). The system's key components are enumerated as follows:

1. The radiation shield installed around the sample holder.
2. View of the beam collimator positioned on the radiation shield upstream of the sample.
3. Images of the optical viewport with a convex lens positioned on the radiation shield at the back (i.e., downstream) side of the sample.
4. View of one of the two windows allowing the β -particles to reach the two beta detectors positioned at the left and right sides of the sample (Fig. A.3a).
5. The liquid He inlet tube.
6. The liquid He inlet port.
7. The liquid He exhaust tube.
8. The liquid He exhaust port.
9. The upper stainless steel flange with the rotatable bellows allowing the cryo-oven alignment with the beamline.
10. The ports of the electrical feedthroughs used for the thermometers and the heater positioned on the cryostat and the radiation shield.
11. The port of the electrical feedthroughs passed through the hollow sample rod for the thermometers on the sample holder.
12. The load lock valve that allows the differential pumping during the sample change process.

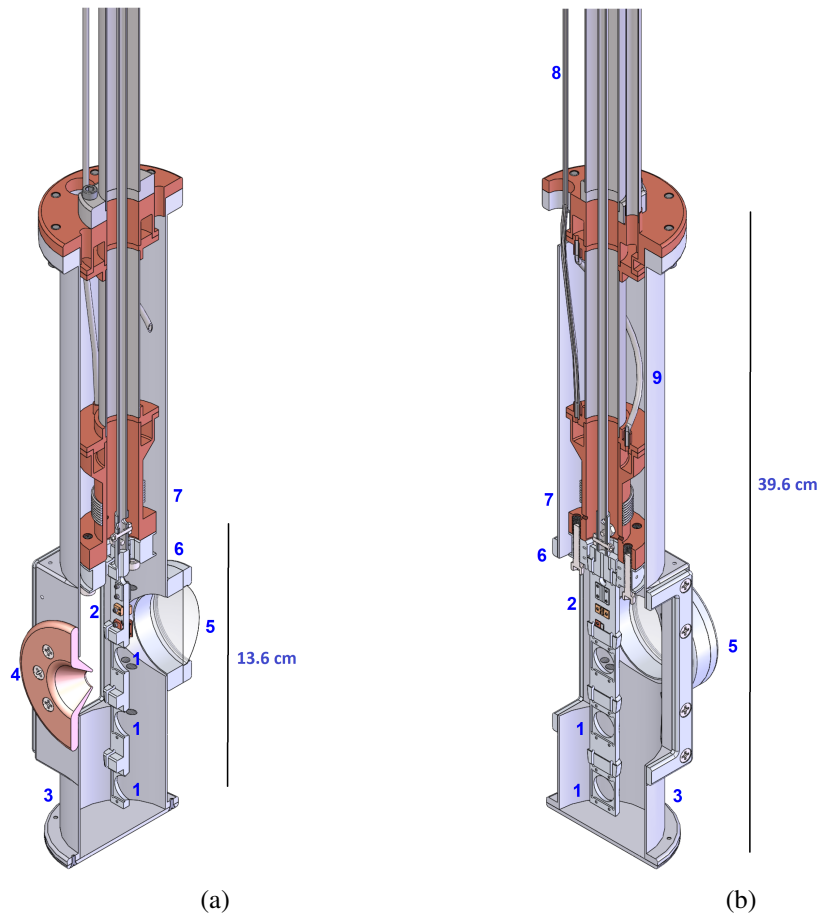


Figure A.2: Images of two SolidWorks cuts of the lower region of the cryo-oven assembly with the various parts enumerated. See text for details.

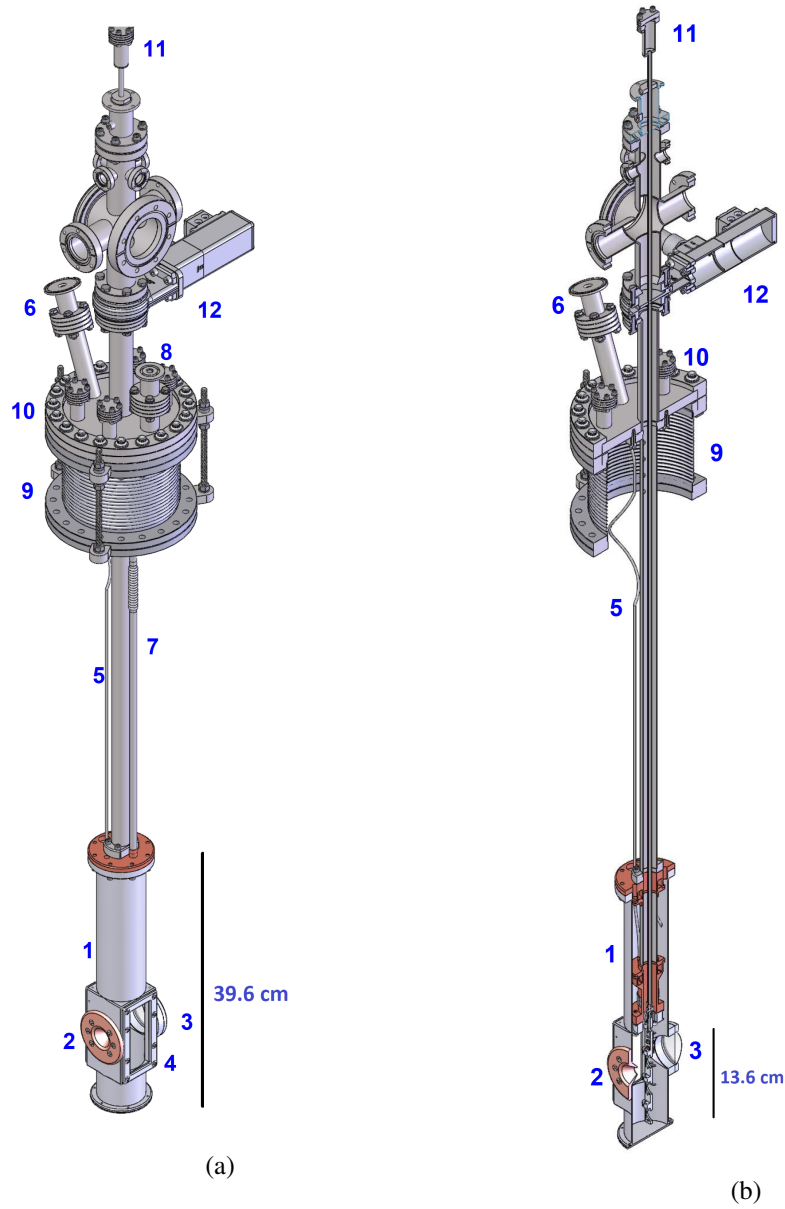


Figure A.3: Images of two SolidWorks overviews of the cryo-oven assembly with the various parts enumerated. See text for details.

Appendix B

Geant4

This Appendix discusses how the Geant4 project used in this thesis is structured. The assumption is that it runs on a Unix-type operating system (e.g., Linux), as Geant4 is almost incompatible with Windows.

As discussed in the Ch. 5, the Geant4 code doesn't have to be used *per se* in order to compile the library of $Y_{\alpha}^n(t)$ versus D , but rather Geant4 is required in order to provide the probability of alpha detection versus depth, each time some aspect of the experiment (such as sample properties, detector geometry, energy threshold) changes. Nonetheless, the project presented here can generate both the α -detection probability vs depth and the actual $Y_{\alpha}^n(t; D)$ signal, simply by changing the input macro file.

B.1 Getting started

An overview of Geant4 can be found here: <https://geant4.web.cern.ch/>

Upon downloading the source code, detailed instructions on how to build and install Geant4 can be found here: <http://geant4-userdoc.web.cern.ch/geant4-userdoc/UsersGuides/InstallationGuide/html/installguide.html>

After the Geant4 software is installed, the novice user can familiarize themselves by going through the example projects provided by the Geant4 development team and are distributed as part of the Geant4 source code.

B.2 The project code tree

Turning now to the project at hand: The classes defining the Geant4 project developed as part of this thesis are very long. If printed here, they would cover more than 80 pages. Instead, they can be found and downloaded at the link: <https://github.com/arishadj/LiDiffusion-v2> together with all secondary files needed for the execution at <https://github.com/arishadj/LiDiffusion-v2-build>.

The following supposes that the source code of the project is copied in a folder named *LiDiffusion-v2*, where the main class file *LiDiffusion.cc* and the

CMakeLists.txt lay, as well as two secondary folders, *src* and *include*. *src* contains the .cc files of the Geant4 code and *include* the header files with the extension .hh:

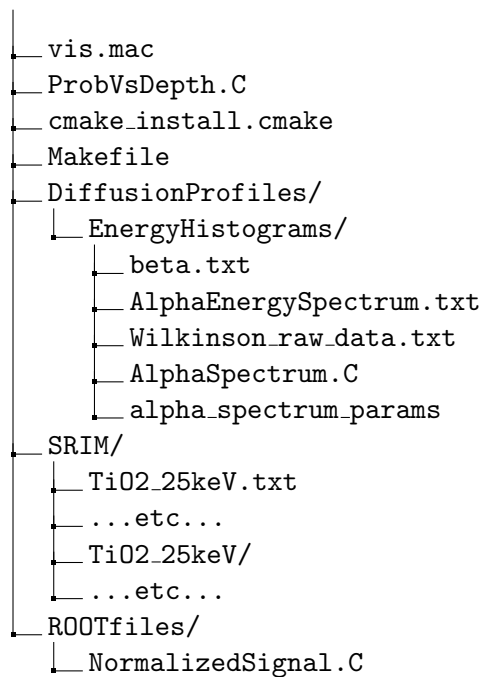
```
LiDiffusion-v2/
├── LiDiffusion.cc
├── CMakeLists.txt
├── src/
│   ├── LiActionInitialization.cc
│   ├── LiDetectorConstruction.cc
│   ├── LiDetectorMessenger.cc
│   ├── LiEventAction.cc
│   ├── LiPrimaryGeneratorAction.cc
│   ├── LiPrimaryGeneratorMessenger.cc
│   ├── LiRun.cc
│   ├── LiRunAction.cc
│   ├── LiSteppingAction.cc
│   └── PhysicsList.cc
└── include/
    ├── Analysis.hh
    ├── LiActionInitialization.hh
    ├── LiDetectorConstruction.hh
    ├── LiDetectorMessenger.hh
    ├── LiEventAction.hh
    ├── LiPrimaryGeneratorAction.hh
    ├── LiPrimaryGeneratorMessenger.hh
    ├── LiRun.hh
    ├── LiRunAction.hh
    ├── LiSteppingAction.hh
    └── PhysicsList.hh
```

The *CMakeLists.txt* file allows the compilation of the project. For more details on how to build and compile a Geant4 project, see:

<http://geant4-userdoc.web.cern.ch/geant4-userdoc/UsersGuides/InstallationGuide/html/quickstart.html>

The compiled code lies on a second folder *LiDiffusion-v2-build*, which also includes the shell environment setup script for Geant4 *geant4.sh* and all other secondary files needed for this project:

```
LiDiffusion-v2-build/
├── LiDiffusion
├── geant4.sh
├── standard.t.mac
└── init.vis.mac
```



The function of each file, both from the source code and the secondary auxiliary files, will be discussed below.

B.3 Running the simulation

To run the compiled code, simply open a terminal in the *LiDiffusion-v2-build* folder and execute:

```

1 >> source geant.sh
2 >> ./LiDiffusion

```

This initializes the Geant4 code. After the end of this process, the user can apply commands that either define parameters of the simulation, or start the simulation itself. Because the simulation at hand is rather complex and is designed to be flexible, a large number of parameters have to be defined by the user prior to the simulation start. This is taken care by a macro file, such as *standard_t.mac*. To run a macro file, the user should use the command:

```

1 Idle> /control/execute standard_t.mac // or_name_of_another_macro

```

The *standard_t.mac* has the visualization capabilities of Geant4 turned off, in order to speed up the performance. If the user wants to visualize the geometry of the simulation, the macro file *init_vis.mac* should be used instead.

B.4 Structure of the Geant4 project

B.4.1 LiDiffusion.cc

LiDiffusion.cc is the main class of the project. It defines the random number generator, chooses between single-threaded and multi-threaded programming styles and instantiates the *runManager*, by creating instances of the main classes required for the simulation. These are the *LiDetectorConstruction*, which defines the geometry of the simulation (see Sect. B.4.2), the *PhysicsList* that defines the models of the physical interactions to be used in the simulation (Sect. B.4.3) and the *LiActionInitialization* class (Sect. B.4.4), which instantiates all other parts of the simulation.

B.4.2 LiDetectorConstruction/LiDetectorMessenger

The *LiDetectorConstruction* class defines all the information regarding the materials and the geometry of the simulation. The user can change most aspects of the geometrical structures (materials, sizes etc) using the macro file, which passes these inputs to *LiDetectorConstruction* through the *LiDetectorMessenger* class. *LiDetectorMessenger* contains the definition of the available commands for changing the geometry of the simulation.

The header file *LiDetectorConstruction.hh* contains the definitions of all public and private functions, as well as all protected objects that are used during the simulations (e.g., the *G4LogicalVolume* structures).

The .cc file contains the definition of all relevant methods. *MakeMaterials()* instantiates the material manager and defines the default material of each component (e.g., sample, detector etc). *Construct()* is the main function that defines and creates the geometry of the simulation, as well as which LogicalVolumes correspond to which detector. This source code also contains a number of auxiliary functions that are used to define the material of each component, e.g., *SetSampleMaterial(...)* sets the material of the sample, as defined by the user through the macro file.

Finally, the class *LiDetectorConstruction* contains the methods required in order to import the SRIM implantation profile and calculate the temporally-evolved depth profile. These methods are called at the *LiPrimaryGeneratorAction* class that defines the properties of the particle beam, but are placed in *LiDetectorConstruction*, in order to allow for parallel execution of the simulation, as *LiDetectorConstruction* is shared between all CPU cores, in contrast with the *LiPrimaryGeneratorAction* which is defined locally in each core.

The method *CheckDepthDistribution()* checks if the depth distribution for the user-defined diffusion rate, boundary condition and point in time already exists in

the folder `.../LiDiffusion-build/DiffusionProfiles/NAMEofSRIMfile/`

For instance for a diffusion rate $10^{-9} \text{ cm}^2 \text{ s}^{-1}$, a trapping boundary condition at the sample's surface, SRIM file `TiO2_25keV` and time 0.1 s, it will seek the file `.../LiDiffusion-build/DiffusionProfiles/TiO2_25keV/D1e-09t0_1accumulative.txt`. If it exists, then it will just get imported. If not, then the method: `MakeDepthDistribution(...)` will be invoked.

`MakeDepthDistribution(...)` creates the time-evolved profiles starting from the SRIM file. It calls the method `ReadSRIMProfile(...)` to import the SRIM profile and then calculates the depth distribution for the requested point in time by stepping from time $t = 0$ and calculating all intermediate distributions with a finite differences numerical code. Until the BeamOff time, the initial implantation distribution gets replenished at each time increment and the depth profile is evolved in time using Fick's Second law (Eq. 5.1).

After the final depth profile is calculated, it is used by the method `SetCoefficients(...)` to define the coefficients needed to sample the profile by the random number generator of the `LiPrimaryGeneratorAction` class.

B.4.3 PhysicsList

`PhysicsList` class defines which models will be imported in order to simulate all relevant physical interactions. The classes `G4EmLivermorePhysics` and `G4EmExtraPhysics` are used for the electromagnetic interactions, as they are considered the most accurate models in the MeV energy region [179]. `G4HadronElasticPhysics` defines the nuclear elastic scattering and `G4HadronPhysicsQGSP_BERT` imports the Bertini model for the hadronic interactions, as it is deemed the most suitable for energies below $\sim 10 \text{ GeV}$ [180].

B.4.4 LiActionInitialization

`LiDetectorConstruction` and `PhysicsList` are the two classes that are shared by all CPU cores, i.e., they are running in the master thread. `LiActionInitialization` instantiates both the master thread - with the method `BuildForMaster()` - and each parallel thread with the method `Build()`.

Each thread creates instances of the classes `LiRunAction`, which defines the output of the simulation (see Sect. B.4.6), the `LiPrimaryGeneratorAction` class, which defines the properties of the "particle gun" (see Sect. B.4.5), `LiEventAction` (Sect. B.4.6), which collects all relevant information after the simulation of each "event" (i.e., each ^8Li decay) and the `LiSteppingAction`, which collects the energy deposited in the detectors during each "step" of each particle's trajectory (Sect. B.4.6).

In a nutshell, the structure of the simulation is the following: Each thread creates the primary particles (i.e., the products of an ^8Li decay) with an initial position, momentum, energy and direction defined by the user or through statistical distributions and random number generation. Each of these particles is propagated in the geometry of the simulation in small steps. At each step, all relevant physical interactions are applied in a stochastic manner. They can generally result in energy loss, momentum/direction changes and secondary particle creation. At the end of each step, the energy deposited at the detectors is collected by the class *LiSteppingAction*, which passes it to the class *LiEventAction*. The above tracking process continues until each primary particle loses all its energy, or propagates out of the defined simulation geometry. Then, the same process is repeated for each produced secondary particle.

LiEventAction accumulates the energy deposited in the detectors during the whole tracking of all particles created by a single ^8Li decay and passes the total energy deposited at that decay event to the *LiRunAction* class which registers it in an output ROOT file.

B.4.5 LiPrimaryGeneratorAction/LiPrimaryGeneratorMessenger

LiPrimaryGeneratorAction defines all properties of each primary particle to be tracked in the simulation geometry in the main method *GeneratePrimaries(...)*. The (x,y) coordinates of the decay are generated by a Gaussian distribution, with center and sigma values defined by the user in the macro file through the *LiPrimaryGeneratorMessenger* class. The decay depth follows the distribution defined by the method *MakeDepthDistribution(...)* of the *LiDetectorConstruction* class (see Sect. B.4.2).

If the user wants to generate the probability vs depth instead of simulating the $Y_\alpha^n(t)$ signal, then they should pass a negative value for time through the macro file. Then *LiPrimaryGeneratorAction* will generate a flat distribution of depths in the first 20 μm .

The beta particle coming from the ^8Li beta decay is assigned a random energy following the experimental beta energy distribution by calling the method *MakeBetaDistribution()* which reads the auxiliary file *beta.txt* (Sect. B.2) and creates a random number following that distribution. Its momentum direction is completely random. To take into account the spin polarization of the beam, a custom code should be inserted here. As this is inconsequential for the diffusion study, it is omitted.

For each decay event, a pair of alpha particles emitted back-to-back at the same coordinates as the beta are also generated. Their energy follows the energy distribution defined in the auxiliary file *AlphaEnergySpectrum.txt*. This file is created using the experimental values of the spectrum from [93] by running the ROOT file

AlphaSpectrum.C. As the file *AlphaEnergySpectrum.txt* is already defined, the user does not have to recompile it each time.

B.4.6 LiRunAction/LiEventAction/LiSteppingAction

LiSteppingAction gets the information of the current coordinates of the trajectory of each propagating particle, checks if it is inside some detector defined at *LiDetectorConstruction* (Sect. B.4.2) and if it is, passes the energy deposited in that detector by the tracked particle during the current step of its trajectory to the *LiEventAction* class.

LiEventAction class sums at the end of each decay event the energy deposited in the detectors by all/some particles in all the steps of their trajectories and fills the histograms defined in the *LiRunAction* class with the relevant values.

LiRunAction defines what information will be stored in the output ROOT file. It creates a number of histograms to be filled (e.g., the histogram of the ^8Li depth distribution in the sample), as well as a “Ntuple” structure, which contains “leaves” with the relevant information of each decay event (e.g., decay depth and energy deposited at the detector).

B.4.7 Output files

The output of the simulation is a .root file. If the simulation was aiming to get the probability of detecting an alpha versus decay depth, then one has to run the ROOT file *ProbVsDepth.C* with ROOT, in order to generate the relevant .txt file from the raw .root output file.

If the chosen output is the $Y_\alpha^n(t)$ signal, then upon completion of all simulations (one for each chosen instance in time), the .root files should be moved to the *ROOTfiles* folder and the code *NormalizedSignal.C* should be executed with ROOT in order to generate the normalized alpha signal from the raw energy deposition at the detector.

To change the detector threshold, one has to manually change the value defined in the *ProbVsDepth.C* and *NormalizedSignal.C* files, but can use the same .root files in order to re-calculate the $Y_\alpha^n(t)$ signal. The detector threshold can be defined either directly by an energy value (e.g., 2 MeV), or indirectly by choosing which percentage of the highest energy alphas should be detected (e.g., the 30 % of the highest energy alphas corresponds to an energy threshold of roughly 2 MeV).

B.4.8 Macro (input) file

The macro files with the extension .mac define all parameters of a simulation. For instance, the following commands define the verbose levels of the simulation:

```
1 /control/verbose 0
2 /control/saveHistory
3 /run/verbose 0
4 /control/cout/ignoreThreadsExcept 0
5 /event/verbose 0
6 /tracking/verbose 0
```

The following commands then define the various geometrical characteristics of the sample, (optional) substrate and alpha detector:

```
1 /LiDiffusionCode/geometry/createSampleMaterial 3.15 Mg 1 F 2
2
3 /LiDiffusionCode/geometry/setSampleWidth 7 mm
4 /LiDiffusionCode/geometry/setSampleDepth 500 um
5 /LiDiffusionCode/geometry/setSubstrateWidth 7 mm
6 /LiDiffusionCode/geometry/setSubstrateDepth 500 um
7 /LiDiffusionCode/geometry/setDetectorWidth 0.4 mm
8 /LiDiffusionCode/geometry/setDetectorDepth 0.1 mm
9 /LiDiffusionCode/geometry/setDetectorRadius 5.72 mm
10 /LiDiffusionCode/geometry/setFilename MgF2
```

In this case, the sample would be a $7 \times 7 \times 0.5$ mm³ MgF₂. The substrate has nominally the same size, but as its material is not defined in the macro file, it takes its default value of being made of vacuum, i.e., it does not exist. The alpha detector is a ring (with its internal side cut at a 45° angle) and the above commands define its radius, width and depth. As its material is not defined in this macro file, it takes its default value of being made of ZnS(Ag).

The characteristics of the particle beam and the requested instance in time to be simulated are defined by the following commands:

```
1 /LiDiffusionCode/geometry/LiIonsPerPulse 1000000
2 /LiDiffusionCode/geometry/setBeamOnTime 1 s
3 /LiDiffusionCode/geometry/setSRIMfilename TiO2_25keV
4 /LiDiffusionCode/geometry/setDiffusionRate 1e-11
5 /LiDiffusionCode/geometry/setBoundaryCondition reflective
6 /LiDiffusionCode/geometry/setTime 0.1 s
```

The above commands define that the ion beam will contain 10^6 Li ions, which is taken into account during the beam implantation time, defined to be 1 s. The SRIM file to be imported is the *TiO2_25keV* (i.e., a 25 keV $^8\text{Li}^+$ beam implanted into TiO_2) and this initial depth distribution is to be developed in time with a diffusion rate of $10^{-11} \text{ cm}^2 \text{ s}^{-1}$ and a reflective boundary condition at the surfaces of the sample, until the depth distribution at the requested point in time ($t = 0.1$ s) is calculated.

Finally, the following commands update the parameters with the user-defined values and instantiate the simulation, in this case with 10^7 ^8Li decays.

```
1 /LiDiffusionCode/geometry/diagnostics 1
2 /LiDiffusionCode/geometry/update
3
4 /run/beamOn 10000000
```

To generate a full $Y_\alpha^n(t;D)$ signal, the above commands should be re-defined in succession for each required point in time. To generate the probability vs depth distribution, then the */LiDiffusionCode/geometry/setTime* command should be set to some negative value (e.g. -1). In this case, it is recommended to run very long simulations, at least 10^6 decay events per nanometer of the profile.